2020

The architecture of a lower-crustal shear zone and evidence for along-strike variations in strain localization and partitioning, Fiordland, New Zealand

Peter Carl Lindquist
University of Vermont

The architecture of a lower-crustal shear zone and evidence for along-strike variations in strain localization and partitioning, Fiordland, New Zealand

A Thesis Presented

by

Peter Carl Lindquist

to

The Faculty of the Graduate College

of

The University of Vermont

In Partial Fulfillment of the Requirements
for the Degree of Master of Science
Specializing in Geology

August, 2020

Defense Date: May 29th, 2020
Thesis Examination Committee:

Keith Klepeis, Ph.D., Advisor
Michael Ruggiero, Ph.D., Chairperson
Laura Webb, Ph.D.
Cynthia J. Forehand, Ph.D., Dean of Graduate College

Abstract

Rocks exposed in Fiordland, New Zealand provide a record of magmatic and tectonic processes that were active in the middle to lower crust of a magmatic arc during the Early Cretaceous. The George Sound shear zone (GSSZ) is one expression of those processes, and is a steep, lower-crustal shear zone that accommodated oblique sinistral motion within the continental margin of Gondwana. I have compiled structural and petrologic observations from five field areas that span the 50 km length of the exposed GSSZ. Directional and orientation statistics allow me to compare the orientation of fabrics at each field area to characterize the geometry of the GSSZ. Petrographic and microstructural analyses provide insight into the metamorphic history of rocks the GSSZ and the temperatures at which they deformed. Synthesizing these data, I construct a model of the large-scale architecture of the GSSZ and explore the tectonic, magmatic, and metamorphic processes that may have driven its evolution.

The George Sound shear zone is defined by a zone of rocks that exhibit evidence of deformation at upper amphibolite facies conditions and dominantly sinistral kinematic indicators in N- to NE-striking fabrics. This zone varies from meters to kilometers in width, and contains segments that split into up to four separate branches. Apparent variations in the amount of strain accommodated by different fabrics within the shear zone suggest that, over time, strain localized into narrower zones. These strands of high-strain fabrics experienced extensive hydration metamorphism or are found in lithologically heterogeneous areas containing weaker lithologies, indicating that strain localization processes in the lower crust can vary at the kilometer scale within a single shear zone. The geometry of fabrics also varies along strike within the GSSZ, expressed, from north to south, as a shallowing of mineral lineation directions from 70° plunges to 0–30° plunges. Such variation may be the result of strain partitioning within the lower crust, with contractional structures adjacent to the GSSZ along its southern extent enabling more strain partitioning than in the north where the GSSZ appears to accommodate non-partitioned transpression. The architecture and along-strike variations in deformation processes in the GSSZ highlight the possible complexities of lower-crustal shear zones and the numerous factors that may control the rheology of the lower crust.

Acknowledgements

I owe the greatest thanks to my advisor, Keith Klepeis, whose help and guidance were instrumental at every step of this project. Our collaborators, Joshua Schwartz, Elena Miranda, Harold Stowell, Rose Turnbull, and Richard Jongens were wonderful to work with in the field and provided crucial analyses and discussions afterward. I am grateful to Jody Smith and Dave West at Middlebury College for allowing me the use of their SEM, and I am particularly thankful to Jody for the time she gave in training me on their machine. Cameron Davidson was also very helpful in our discussions of EDS data and exploring relationships between deformation and metamorphism. I am very thankful for Joshua Davis and Sarah Titus in helping me understand and apply some statistical methods to our structural data.

In the UVM Geology Department, I owe thanks to Laura Webb for her instruction on microstructural analysis, her insights on some confusing thin sections, and for the use of her petrographic microscope. Gabriela Mora-Klepeis was also a great help in preparing to use laboratory equipment. I must also acknowledge the work of former UVM graduate students Griffin Moyer and Hannah Blatchford, upon whose earlier work on parts of the George Sound shear zone I am building.

Table of Contents

Acknowledgements ii
List of Figures xiii
List of Tables xiv

1 Introduction **1**

2 Geologic Background **4**
2.1 Fiordland Geologic Setting 4
2.1.1 The Median Batholith: arc magmatism in Fiordland 4
2.1.2 Mesozoic deformation and metamorphism 10
2.1.3 Cenozoic transpression and exhumation of Fiordland arc rocks 13
2.2 Shear Zones 14
2.2.1 Strain localization in shear zones 15

3 The fabrics of the George Sound shear zone **19**
3.1 Overview of Methodology 21
3.1.1 Field Work and Data Collection 21
3.1.2 Structural Analysis 22
3.1.3 Petrographic Analysis 29
3.1.4 Geochemical Techniques 30
3.2 Bligh Sound 31
3.2.1 Fabric facies 33
3.2.2 Statistical Analysis 46
3.2.3 Mineral Compositions 50
3.2.4 Summary 58
3.3 George Sound 61
3.3.1 Fabric facies 62
3.3.2 Statistical analysis 73
3.3.3 Summary 77
3.4 Mary Peaks 82
3.4.1 Fabric facies 84
3.4.2 Statistical Analysis 93
3.4.3 Summary 94
3.5 Myth Tarn 97
3.5.1 Fabric facies 98
3.5.2 Statistical Analysis 104
3.5.3 Summary 108
3.6 Southern Misty Margin 109
3.6.1 Fabric facies 109
3.6.2 Statistical Analysis 114
3.6.3 Summary 117

4 Discussion **120**
4.1 Architecture of the George Sound shear zone 121
4.2 Deformation processes in the George Sound shear zone 126
4.2.1 Strain partitioning 128
4.2.2 Strain localization 131

5 Conclusions **136**

Bibliography **139**

Appendix A Map of field sites for QMAP data **148**

Appendix B Bligh Sound mineral composition **150**

List of Figures

2.1 Palinspastic reconstruction of Gondwana at ca. 100 Ma, showing the extent of magmatic arc rocks and the future continent Zealandia. Plutonic rocks from this magmatic arc comprise the Median Batholith in Fiordland. Modified from Mortimer 2008. 5

3.1 Simplified geologic map of western Fiordland showing the extent of the GSSZ presented here and the location of field areas relevant to this study. (a) Bligh Sound, (b) George Sound, (c) Mary Peaks, (d) Myth Tarn, (e) Coronation Saddle and Cozette Burn. Lines within GSSZ fabric domains represent foliation trajectories. All maps in this thesis use the NZTM projection. Geologic data are derived from *Geology of the Fiordland Area. Institute of Geological & Nuclear Sciences 1: 250,000 Geological Map 17* n.d. 24

3.2 Detail map of Bligh Sound showing stations of 2018. The spatial extent of fabric facies is outlined here. It is also likely that low-strain fabrics are present to the west of the oblate zone based on available foliation measurements. The nature of the transition between the northern and oblate domains, denoted by a dashed line and question mark, is unknown. Hillshade models in this thesis based on *NZ 8m Digital Elevation Model (2012)* 2016. 33

3.3 Foliation and lineation data from Bligh Sound plotted on stereonets. (a) all foliation and lineation data. (b) Foliation/lineation pairs representing the subset of the data used for orientation statistics. (c) Paired orientation data colored by geographic location—in this case, by the UTM northing value of the station at which the data were collected. In th simplified map of station locations at left, the station colors corresponding to the color of the corresponding data. 35

3.4 Nadai-hsu plot of the results of the R_f/ϕ method of finite strain analysis applied to samples from the Worsley Pluton by Moyer (2019). Points on the diagram represent finite strain ellipsoids and are parametrized by an angular component, the Lode's parameter, and a radial component, a measure of the magnitude of strain. The former quantifies the anisotropy of the shape of an ellipsoid, and the latter is proportional to the octahedral shear strain, which may be thought of as a measure of the average distortion of material lines (Vollmer 2018; Brandon 1995). Red regions represent 95% confidence regions determined by bootstrapping ellipsoid data. Two sets of shape fabric ellipsoids representing different populations of fabrics at Bligh Sound are apparent. Adapted from Moyer (2019). 37

3.5 Stereonet plots of foliation and lineation directions—including both paired and unpaied data—from the three fabric facies present at Bligh Sound. 38
3.6 Microstructures in prolate samples. (a) Cpx tails on Opx grain in sample 18BS60 (from Moyer, 2019) (b) tail of recrystallized pyroxene, hornblende, and opaques on a pyroxene aggregate in sample 18BS78. Cpx appears to be replacing Opx within the aggregate and a rim of hornblende is present on the Cpx. (c) cuspate-lobate grain boundaries in plagioclase and anti-perthitic exsolution textures in sample 18BS42. (d) cuspate-lobate grain boundaries in matrix plagioclase and a trail of pyroxene, hornblende and opaques at top of image in sample 18BS78. 40
3.7 Microstructures in 18BS35A from the northern oblate domain. (a) asymmetric Opx porphyroclast with Cpx + Hbl tails. (b) Opx aggregates with Cpx, Hbl, and opaque tails; Cpx rim on Opx grain visible bottom left. (c) Plagioclase microtexutres and a hornblende shear band. Coarser plagioclase at the top of image exhibits lobate grain boundaries, and there is a reduction in plagioclase grain size closer to the hornblende shear band that cuts through the image. 43
3.8 Microstructures in samples from the southern oblate domain. (a) hornblende, biotite, and quartz shear bands originating on Opx grains in pyroxene aggregates in 18BS64A. (b) at top: Cpx-dominated aggregate with biotite tails; at center: large, deformed Opx grain mantled by Cpx with Hbl + Bt shear bands; at bottom left: sigmoidal Opx + Cpx aggregate with recrystallized tails of pyroxene and hornblende; 18BS69A. (c) shear bands separated by domains of coarser plagioclase that is grain-size reduce closer to the shear bands; 18BS26A (d) plagioclase bulging and subgrain textures in 18BS69A. 45
3.9 Equal volume plots and lower-hemisphere stereonets of the paired foliation/lineation orientations from each fabric facies at Bligh Sound to demonstrate the clustering of paired foliation/lineation measurements from each facies. 48
3.10 (a) The equal volume plots shows two 95% credible ellipsoids determined via MCMC simulations of the paired foliation/lineation orientation data from the central and southern oblate domains of Moyer (2019). Because of the overlap between these ellipsoids, the two-sample hypothesis test fails to reject the null hypothesis that these datasets are drawn from populations with the same mean orientation. In (b), these credible ellipsoids are projected onto a lower-hemisphere stereonet and appear as three ellipses with mean foliation and lineation directions plotted. 49

3.11 (a) Equal-volume plots of the 95% credible regions determined for orientations from each fabric facies at Bligh Sound from MCMC simulations. (b) 95% credible regions projected onto a hemispherical stereonet for comparison with mean foliation and lineation orientations. Although the projected credible regions for the prolate and southern oblate fabrics overlap, note that the 3D credible ellipsoids in (a) do not—this overlap is an result of projecting the credible ellipsoids onto a hemispherical plot. The paired foliation/lineation orientations from these facies are still statistically different. (c) 95% confidence ellipses from bootstrapping directional foliation and lineations data. Directional inference and orientational inference results are compared at right, showing good agreement between the two methods. 51
3.12 Pyroxene quadrilateral showing the compositional variations of pyroxenes between the various fabric facies of Bligh Sound. Pyroxenes from the oblate facies are generally enriched in Fe relative to those of the prolate fabrics. 54
3.13 Cross section of southern section of the GSSZ at Bligh Sound. Figure 3.2 locates the profile A-A' and contains the legend for symbology. The cross section highlights the relationship between prolate and southern oblate fabrics, with pods of the former be preserved in the latter as strain localized. We extend the prolate domain from 3.2 to the west of the high-strain domain based on the orientation of fabrics reported in the Fiordland QMAP database. 58
3.14 Detail geologic map of George Sound showing stations of the 2018 field season. Domains of high and low-strain fabrics are based on observations presented in this section and inferences to the north and south of George Sound are based on fabric measurements reported in the Fiordland QMAP database. 64
3.15 Equal-area stereonets of fabrics orientations at George Sound broken out by lithology and apparent strain intensity. 65
3.16 Field photos of magmatic textures at George Sound including (a) magmatic brecciation textures and (b) magma mixing textures at station 19GS127 where felsic and dioritic material of the McKerr Intrusives appears to have mixed. Photomicrographs of undeformed eastern McKerr Intrusives from sample 18GS120A showing the same field of view in (c) PPL and (d) XPL. The preservation of igneous textures indicated by the plagioclase lath at right suggests this rock experienced little deformation. 66

3.17 (a) Photo of low-strain fabrics in the McKerr Intrusives defined by mafic aggregates (station 18GS98). (b) and (c) are photomicrographs of sample 18GS97A, which has a smoother fabric than that in (a). Foliation in these is defined by biotite, hornblende, and epidote, with minor titanite. In (c), plagioclase feldspar exhibits cuspate-lobate grain boundaries and pinning by biotite. 67
3.18 Field photos and photomicrographs of the high-strain fabrics in the different lithologies of the Anchorage Cove complex (station 18GS129). (a) dark, dioritic material at right with fabric defined by mafic aggregates that are inclined to the compositional layering, suggesting sinistral shearing. (b) preferentially weathered sigmoidal aggregate of mafic minerals and garnet in a quartz-rich metamsedimentary layer, indicating sinistral motion. (c) shows isoclinal folds are developed in a section of interlayered dioritic and granitic material. (d) A photomicrograph from a sample of amphibolite (18GS129C) showing intact subhedral grains of biotite and hornblende that do not define a clear fabric at the micro scale (e) Photomicrograph in PPL of the metasedimentary rocks (18GS129A), showing the layering of mafics and garnet fragments with quartz and feldspar-rich domains, (f) in which amoeboid quartz grains contain elongate subgrain domains. 70
3.19 Photomicrographs of mylonitic fabrics in the Expedition Pluton. In (a), quartz-dominated domains alternate with domains of mixed feldspar and quartz. In (b), white mica can be seen defining boundaries between some of these layers. Quartz contains subgrain domains. 71
3.20 Field photos of low-angle cross cutting mylonitic zones at (a) stations 18GS117 and (b) 18GS125. In (a), deflected foliation in the dioritic McKerr Intrusives into a mylonitic zone indicates a top to the north sense of motion. (b) shows evidence for grain-size reduction between granitic host-rock and mylonites. (c) and (d) show photomicrographs in PPL and XPL, respectively, of a thin section from 18GS117. In (c), the foliation is defined by biotite, epidote, and hornblende with minor titanite. In (d), plagioclase exhibits cuspate-lobate grain boundaries and evidence for pinning on biotite. 72
3.21 Equal volume plots of paired foliation/lineation orientations for (a) low-strain fabrics in the McKerr Intrusives, with a rotated view of the same data contoured with 10-sigma Kamb contour surfaces to emphasize the clustering that is not clear in the plot at top, (b) high-strain fabrics in the Expedition Pluton, and (c), high-strain fabrics at Anchorage Cove. Fabric orientations for each define unimodal clusters. . 75

3.22 (a) Equal-volume plots of the 95% credible regions determined for orientations from the three fabric facies with good orientation data at George Sound from MCMC simulations. (b) 95% credible regions projected onto a hemispherical stereonet for comparison with mean foliation and lineation orientations. (c) 95% confidence ellipses from bootstrapping directional foliation and lineations data. Directional inference and orientational inference results are compared at right, showing good agreement between the two methods. 78
3.23 Schematic cross-section across the GSSZ at George Sound. Key for geologic units is same as figure 3.14. 79
3.24 Map of the entire eastern margin of the Misty Pluton and the three field areas discussed in this section: Mary Peak, Myth Tarn, and the Southern Misty Margin (comprising the Coronation Saddle and Cozette Burn transects. The GSSZ follows this boundary for most of the length of the Misty Pluton and related deformation fabrics are sometimes found in host rocks to the east. 84
3.25 Detail geologic map of the Mary Peaks field area showing the extent of GSSZ fabrics identified, which are confined to the Misty Pluton and the western boundary of the Large Granite. 85
3.26 (a) Lower-hemisphere stereonets of foliation and lineation directions from the different fabric facies at Mary Peaks. (b) Equal volume plot of paired foliation/lineation data from the low-strain (black) and mylonitic (blue) fabrics in the Large Granite, showing that each of these defines unimodal clusters. 86
3.27 a) Low strain, L>S fabric in the Misty Pluton at Mary Peaks defined by biotite aggregates. Petrography suggests this sample is a hybrid of dioritic Misty Pluton and granitic Large Granite material. Sample 19MP14B. (b) Evidence for the overprinting of deformation fabrics by magmatic fabrics in sample 19MP19D (float) with lobes of coarse feldspar, biotite, and hornblende interrupting a finer-grained foliation that is more clearly shown in (c), sample 19MP19C (float). (d) In low-strain sample 19MP14B, coarse grains of plagioclase are separated by networks of fine-grained quartz and feldspar. (e) Quartz grains with cuspate-lobate grain boundaries and chessboard subgrain patterns in sample 19MP19B. (f) In 19MP19D—higher strain than 19MP14B—aggregates of biotite, hornblende, and epidote bounded by zones of mixed feldspar and quartz. Quartz and feldspar exhibit cuspate-lobate grain boundaries, and quartz contains subgrain domains. 88

3.28 Microstructures of the mylonitic Large Granite in sample 19MP19E. (a) Alternating layers of quartz, feldspar, and mica are evident in PPL as feldspar appears darker than quartz. Opaque oxides are also aligned with the foliation. (b) The same field of view as (a) in XPL. The sigmoidal feldspar aggregate in the upper center of the image contains finely-recrystallized tails and indicates sinistral shearing. (c) More detailed view of the feldspar aggregate and surroundings in (b). Cuspate-lobate grain boundaries appear in feldspar within the aggregate at center and elsewhere, and elongate quartz grains may have subgrain domains. 91
3.29 Microstructures of the low-strain Large Granite at Mary Peaks indicative of high-temperature deformation. (a) Elliptical feldspar grain exhibiting flame perthite textures and a core-mantle texture with apparent subgrain development along its margins in sample 19MP23. (b) Chessboard subgrain patterns in quartz grains in sample 19MP23. (c) Irregular grain shapes and cuspate-lobate grain boundaries in feldspar and quartz suggestive of GBM. 92
3.30 95% confidence ellipses from bootstrapping directional foliation and lineation data from the different fabric facies in the Large Granite at Mary Peaks. There is a clear difference between the orientation of mylonitic and low-strain fabrics. 94
3.31 Cross section across the Mary Peaks field area. Step high-strain fabrics are confined to the western edge of the Large Granite, while the Misty Pluton's variable magmatic to low-strain tectonic fabrics are included as low-strain GSSZ fabrics. 96
3.32 Detail geologic map of the Myth Tarn field area, showing the distribution of high and low-strain fabrics discussed in this section. The boundary between the Misty Pluton and Large Granite at this site is defined by a fault. 97
3.33 (a) Stereonets depicting the orientation of fabrics in the different fabric facies observed at Myth Tarn with two different fabrics present in the Misty Pluton. 98
3.34 Examples of the facies 1 fabric in the Misty Pluton. (a) Rough foliation defined by hornblende aggregates at station 19MT07 where (b) a leucocratic vein with associated garnet crosscuts the foliation. (c) PPL photomicrograph of the hornblende aggregates with internal quartz blebs, suggestive of the retrograde breakdown of pyroxene. Euhedral biotite and epidote appear randomly oriented within the plagioclase domains. (d) XPL photomicrograph of the same view as (c) to show plagioclase grain textures including: amoeboid grains with cuspate-lobate grain boundaries and pinning by biotite. Photomicrographs in (c) and (d) are from sample 19MT05. 100

3.35 Field photos of (a) low-strain and (b, c, d, e) high-strain examples of fabric facies two from the Misty Pluton. (a) Smooth foliation defined by alternating layers of mafic minerals and plagioclase at station 19MT03. (b) Foliation is still smooth and defined by networks of mafic minerals, but plagioclase-rich layers have been boudined. Garnet in (c) is wrapped by the foliation. In (d) and (e), pegmatitic veins have been folded and, in (d), boudined. High-strain fabrics found at station 19MT13. 101
3.36 Photomicrographs of the facies two Misty Pluton fabrics. (a) Hornblende, biotite, and epidote form an S-C fabric in 19MT06 suggestive of left-lateral shearing. (b) In XPL, plagioclase grains in 19MT06 appear elongate parallel to the foliation and feature straight grain boundaries with adjacent plagioclase, but may have cuspate to lobate phase boundaries with biotite or hornblende, appearing to fill in irregularities in these minerals. In (c) and (d), high-strain fabrics from 19MT13 are defined by similar hornblende, biotite, and epidote folia, but plagioclase domains appear boudined with the mafic minerals forming and interconnected network. In (d) deformation twins and straight to lobate grain boundaries are apparent in plagioclase. 102
3.37 (a) In the field, the Large Granite at Myth Tarn exhibits a clear biotite lineation and foliation. (b) In thin section, white mica, biotite, epidote, and opaques can be seen defining the fabric, as well as (c) elongate quartz grains. Quartz shows strongly lobate grain boundaries, as well as some subgrain domains in larger grains. (d) Irregular, interlocking feldspar grains 104
3.38 Cross section across the Misty Pluton margin and GSSZ at Myth Tarn, showing low-strain fabrics being deflected into a high-strain zone. Included below the cross section is a stereonet with foliation and lineation data from the Misty Pluton colored by their position on a heading of 115°. The color gradient shows that foliation in the Misty Pluton generally steepens towards the east. Colored squares corresponding to the colors of the data on the stereonet represent where along the transect the data came from. The segment of great circle is the best fit of the geodesic regression discussed in the statistical analysis. 106
3.39 95% confidence ellipses from bootstrapping directional foliation data for the high-strain fabric in the Misty Pluton and foliation and lineation data from the Large Granite. 107
3.40 Map of southeastern margin of the Misty Pluton showing the location of field sites from the Coronation Saddle (2005) transect and Cozette Burn (Camp 2, 2015) transects. Data from Cozette Burn mostly come from within a fault-bounded slice of the Misty Pluton and a screen of the Cozette Pluton 110

3.41 Microstructural characteristics of the fabrics at Coronation Saddle and Cozette Burn. (a) Relict igneous plagioclase and a generally coarse-grained, irregular feldspar grains in the Misty Pluton at station 05-03-01, the station farthest west of the Misty Pluton edge at Coronation Saddle. Hornblende, biotite, and epidote do not exhibit a strong shape-preferred orientation. (b) Hornblende and feldspar aggregates that define the fabrics in the Misty Pluton at station 05-02-02. Hornblende aggregates commonly contain cores of quartz blebs. Compare to the facies one fabrics from Myth Tarn (Fig. 3.34). (c) Plagioclase with relict igneous textures, but recrystallizing margins and deformation twins in the Misty Pluton at station 05-02-02. Finer-grained feldspar in the right side of the image exhibit a strong LPO and cuspate-lobate grain boundaries. (d) Relict pyroxene surrounded by fine hornblende and quartz blebs. This may represent an early stage in the development of the hornblende aggregates with cores of quartz blebs present in the Misty Pluton elsewhere along the Southern Misty margin and at Myth Tarn. From a dioritic dike within a screen of the Cozette Pluton at station 15AB-72. (e) Microstructural characteristics of the Cozette Pluton at station 15AB-72. Quartz ribbons with elongate subgrain domains alternate with zones of fine, amoeboid feldspar grains suggestive of grain boundary migration. From Blatchford (2016). 114

3.42 Equal-area stereonets depicting the orientation of fabrics from the Coronation Saddle and Cozette Burn transects across the Misty Pluton margin. Breaking fabrics from Cozette Burn into those from the Misty Pluton and those from the Cozette Pluton reveal how similar measurements from the two are. Foliation and lineation data from Coronation Saddle are also colored by their UTM easting coordinates to demonstrate the steepening of foliation from west to east in the Misty Pluton, correlating with the development of more well-defined, potentially higher strain fabrics. 115

3.43 (a) MCMC 95% credible ellipsoid for the fabrics at Cozette Burn projected onto a lower-hemisphere stereonet. (b) 95% confidence ellipses from bootstrapping foliation and lineation data separately. The higher-strain fabrics from the eastern edge of the Coronation Saddle transect have a distinct orientation that differs from those fabrics at Cozette Burn. 117

3.44 Cross sections across the Misty Pluton margin at (a) Coronation Saddle, and (b) Cozette Burn. Fabric orientations vary above and below the screen at Coronation Saddle (see Fig. 3.42), and relatively high-strain fabrics are found at the easternmost edge of the Misty Pluton. Only relatively low-strain fabrics that are comparable to those low-strain fabrics at Coronation Saddle and Myth Tarn are found in the Misty Pluton at Cozette Burn. The faults shown in these cross sections represent later, brittle reactivation of the GSSZ (Blatchford, 2016). Modified from Blatchford (2016). 119

4.1 Summary of fabric correlations along the strike of the George Sound shear zone. 123
4.2 Stereonet summary of the orientation of average foliation and lineation directions and associated 95% confidence intervals from the highest-strain fabrics in each field area. No average lineation direction is reported for Myth Tarn and instead the two lineations directions from the high-strain fabrics there are plotted. This plot emphasizes the shallowing of lineation directions from northern field areas to southern ones. 125
4.3 Simplified geologic map of western Fiordland showing the extent of the GSSZ and adjacent contractional structures that were also active during the Early Cretaceous. Shaded brown regions indicate the extent of folds and thrusts that accommodated contraction perpendicular to the axis of the Fiordland magmatic arc (Daczko et al. 2002; Blatchford 2016). 131

List of Tables

3.1 Statistical descriptors of fabric orientations at Bligh Sound. 47
3.2 Representative orthopyroxene compositions 53
3.3 Representative clinopyroxene compositions 54
3.4 Representative hornblende compositions 55
3.5 Representative biotite compositions 57
3.6 Representative plagioclase compositions 57
3.7 Statistical descriptors of fabric measurements from George Sound treated as orientation data 76
3.8 Statistical descriptors of fabric measurements from George Sound treated as directional data. 76
3.9 Statistical descriptors of foliation and lineation measurements from Mary Peaks treated as directional data. 93
3.10 Statistical descriptors of foliation and lineation measurements from Myth Tarn treated as directional data. 107
3.11 Statistical descriptors of foliation and lineation measurements from the Southern Misty Margin treated as directional data. 116

Chapter 1

Introduction

Deformation in continental lithosphere is commonly localized into regions of high strain called shear zones (Fossen and Cavalcante 2017). The degree of localization and evolution of shear zones is known to be influenced by a variety of factors, including the boundary conditions and initial composition of a deforming region (e.g., lithologic heterogeneities, tectonic convergence directions), as well as a wide variety of dynamic chemical and physical processes (e.g., Poirier 1980; Fossen and Cavalcante 2017; Tommasi et al. 1995; Goncalves et al. 2012; Condit and Mahan 2018). The rheology of the lower crust and the structures that develop therein may control the partitioning of deformation in upper levels of the crust, therefore presenting an important control on the behavior of lithosphere-scale boundaries (Teyssier and Tikoff 1998; Klepeis and Clarke 2004). Knowing which processes influenced natural shear zone evolution and how they may vary temporally and spatially within the lower crust is therefore important for understanding the deformation of the continental lithosphere as a whole (Bürgmann and Dresen 2008; Dumond et al. 2018).

The geology of Fiordland, New Zealand provides one opportunity to study shear

zones that developed in the lower and middle crust. The rocks of Fiordland record the history of a long-lived continental magmatic arc, as well as the deformation it experienced (Mortimer et al. 1999; Allibone et al. 2009b; Schwartz et al. 2017; Tulloch and Kimbrough 2003; Klepeis et al. 2019). The upper plate in continental subduction systems is known to evolve in a variety of extensional or contractional environments (Ducea et al. 2015). Deformation related to these forces may be expressed in the upper crust as forearc and backarc fault systems or foreland thrust belts, but the localization of structures at deeper levels in magmatic arcs and their evolution is less well understood.

Several lower-crustal, transpressional shear zones are exposed in Fiordland that were active during an Early Cretaceous high-flux episode that emplaced the Western Fiordland Orthogneiss (Schwartz et al. 2017). One such shear zone, the George Sound shear zone in western Fiordland, developed contemporaneously with magmatic and metamorphic events within a heterogeneous lower crust and exhibits complex geometry and strain patterns (Klepeis and Clarke 2004). The exposure of this shear zone thus provides an opportunity to explore the heterogeneous architecture of lower crustal shear zones and the processes that influence their localization and evolution.

Previous work has characterized the George Sound shear zone (GSSZ) at Bligh Sound and identified branches of it at George Sound (Moyer 2019; Klepeis and Clarke 2004; Allibone et al. 2009b). The results of field work presented here allows us to extend the GSSZ farther south, linking it with other previously described shear fabrics in central Fiordland (Blatchford 2016). In this thesis, I will therefore synthesize observations from all of these field areas to present a more consolidated picture of the architecture of the GSSZ. To accomplish this, I describe the deformation processes that appear to have influenced the evolution of the GSSZ,

and attempt to address the questions of (1) how the processes controlling strain localization may vary within a single shear zone, and (2) how apparent variations in deformation processes within the GSSZ are reflected in its architecture and the geometry of its shear fabrics.

In addressing these questions, I rely primarily on structural observations from the field and petrographic and microstructural analyses of samples from the GSSZ. To structural measurements of fabric orientations, I apply the methods of directional and orientation statistics to compare the orientations of different sets of fabrics and better quantify our uncertainty in the geometry of the GSSZ. For one field area, I will also employ some mineral composition data acquired via energy dispersive X-ray spectroscopy in exploring the metamorphic processes that may have affected the evolution of fabrics. Ultimately, my results suggest that, within the GSSZ, strain localization processes varied, with metamorphism and lithologic heterogeneities influencing the evolution of different parts of the GSSZ. Additionally, variations in fabric geometry suggest that the GSSZ system accommodates partitioned transpression along its southern extent, but non-partitioned transpression along its northern extent. Both these localization and partitioning factors appear to have influenced the size and form of the George Sound shear zone.

Chapter 2

Geologic Background

2.1 Fiordland Geologic Setting

The continent Zealandia—as defined by Mortimer (2017)—is composed of rocks derived from the paleo-Pacific–Gondwana margin. Between the Cambrian and the Early Cretaceous, this margin experienced periods of oblique convergence as oceanic lithosphere of the paleo-Pacific plate subducted beneath Gondwana and allochthonous terranes were accreted onto the continental margin (Mortimer 2004). The subduction of oceanic lithosphere caused the development of a Cordilleran-style magmatic arc in the overriding Gondwanan crust (Tulloch and Kimbrough 2003). Part of this magmatic arc is now exposed in Fiordland as the rocks of the Median Batholith, providing an opportunity to study the structure and evolution of the interior of a long-lived continental magmatic arc.

2.1.1 The Median Batholith: arc magmatism in Fiordland

The Median Batholith is a contiguous collection of plutons that were emplaced into the margin of the continent Gondwana between the Ordovician and the Early

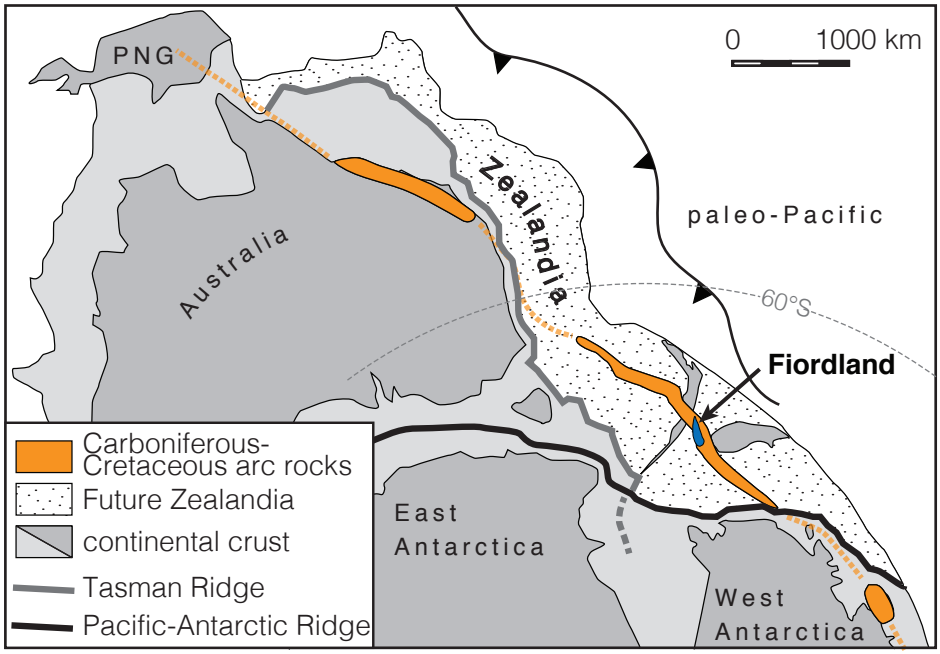

Figure 2.1: Palinspastic reconstruction of Gondwana at ca. 100 Ma, showing the extent of magmatic arc rocks and the future continent Zealandia. Plutonic rocks from this magmatic arc comprise the Median Batholith in Fiordland. Modified from Mortimer 2008.

Cretaceous (Mortimer et al. 1999; Allibone et al. 2009b). The rocks from the Fiordland arc appear to be related to similar arc-related rocks preserved in Australia and West Antarctica, and paleogeographic reconstructions link these belts of igneous rocks to infer the existence of a magmatic arc along the Gondwana margin (Fig. 2.1; Mortimer 2008). These batholithic rocks intruded Paleozoic metasedimentary and volcanic rocks from the Gondwanan continental margin. This section includes a brief introduction to the high-level nomenclature used to group these metasedimentary and volcanic rocks and to define the Median Batholith in New Zealand. Following this introduction, I describe the specific formations that are relevant to this research.

The rocks of New Zealand may be divided between a Western province and an Eastern province. The Western province includes Cambrian–Devonian

metasedimentary basement rocks that were part of the Gondwanan margin in the early Paleozoic, and the Eastern province is composed of rocks at or outboard to (east of) the early Paleozoic continental margin of Gondwana (Allibone et al. 2009a). The Eastern province largely consists of terranes accreted onto the Gondwana margin, although the origin of some terranes is ambiguous. These provinces are subdivided further into terranes of rocks of similar ages derived from similar depositional and tectonic settings. Terranes present in western Fiordland include the Buller and Takaka terranes—which comprise the Western province—and the Brook Street terrane, Drumduan terrane, and other lithotectonic units of the Eastern province. The Buller terrane is composed of metamorphosed siliciclastic rocks of Ordovician age, and the Takaka terrane includes Cambrian–Devonian siliclastic, carbonate, and volcanic rocks. The Brook Street terrane, composed of Permian volcanic rocks, accreted onto the Takaka terrane during the Early–Middle Triassic. However, Median Batholith plutons from the Jurassic and Early Cretaceous have obscured any preexisting contact between the Takaka and Brook Street terranes (Mortimer 2004).

Rocks of the Median Batholith began intruding these terranes in the Ordovician, with subduction related magmatism causing the episodic emplacement of plutons through the Early Cretaceous (Tulloch and Kimbrough 2003). The plutons of the Median Batholith are divided between inboard and outboard belts. Plutons of the inboard belt are those that intruded rocks of the Western province (towards the interior of Gondwana), and outboard plutons are those that intruded Eastern province rocks (at or east of the Gondwana–paleo-Pacific margin) (Allibone et al. 2009a). Inboard and outboard plutons are generally geochemically distinct from each other and yield different emplacement ages. Primarily low Sr/Y plutons were emplaced in the outboard arc between 230 and 136 Ma, while mostly high Sr/Y

plutons were emplaced into the inboard arc between 128 and 115 Ma during the final episode of high-flux magmatism (Tulloch and Kimbrough 2003; Schwartz et al. 2017).

Two major crustal boundaries that served as loci for subsequent magmatism and deformation are present in Fiordland. The oldest, westernmost boundary is defined by a belt of Carboniferous granitoid plutons, which align with the Early Cretaceous George Sound shear zone and Late Miocene reverse faults that reactivated this zone of deformation. The easternmost boundary is defined by several Early Cretaceous shear zones that juxtapose Jurassic plutons of the Median Batholith with Paleozoic Gondwanan basement rocks to the west. The latter boundary represents the eastern limit of the Paleozoic Gondwana margin in Fiordland and separates the Western province and inboard plutonic belt from the outboard plutonic belt (Klepeis et al. 2019; Buritica et al. 2019). The field area of this study is centered on the westernmost boundary.

Plutons of the study area

Granitoid plutons emplaced during the Devonian and Carboniferous are some of the oldest members of the Median Batholith in Fiordland. In the field area, Carboniferous granitoid plutons are aligned in a north–south belt apparent across central and southern Fiordland. In western Fiordland, this zone was intruded by another belt of plutons during a pulse of high-flux magmatism in the Early Cretaceous.

Three Carboniferous granitoid plutons lie within the study area: the Cozette Pluton, Large Granite, and Expedition Pluton. These plutons are dominated by rocks ranging from syenogranite (Cozette and Expedition Plutons) to biotite granite (Large Granite) to alkali feldspar granite (Expedition Pluton; Allibone et al.

2009a). Zircon U-Pb dating indicates emplacement ages of 340.9 ± 7.4 Ma for the Cozette Pluton, 348.5 ± 9.9 Ma for the Large Granite, and 317 ± 7.3 Ma for the Expedition Pluton (2σ uncertainty; Ramezani and Tulloch 2009). The Large Granite and Cozette Pluton have intrusive contacts with older Paleozoic metasediments of the Irene Complex along their eastern margins. These Carboniferous granitoids are the remnants of the initiation of the emplacement of the Median Batholith in this section of Fiordland.

The Lake Hankinson Complex represents another major pulse of magmatism in central Fiordland in the Late Jurassic. This heterogeneous igneous complex is composed of rocks ranging in composition from granite to diorite with reported ages ranging from 159.9 to 134.1 Ma (Allibone et al. 2009a). The Large Granite and the Expedition Pluton are separated by part of the Lake Hankinson Complex, which extends far to the south where it has an intrusive contact with the eastern margin of the Irene Complex, and to the northeast in central Fiordland, where it was intruded by younger plutons in the Early Cretaceous.

A final pulse of high-volume magmatism in Fiordland produced the Western Fiordland Orthogneiss in the Early Cretaceous, which dominates the Median Batholith in western Fiordland (Schwartz et al. 2017). The Carboniferous granitoids, Lake Hankinson Complex, and Paleozoic metasediments were all intruded by the Western Fiordland Orthogneiss (WFO). The term WFO encompasses three major plutons—the Worsley, Misty, and Malaspina Plutons—as well as several other intrusive bodies, all of which were emplaced between ca. 128 and 114 Ma (Schwartz et al. 2017).

The oldest component of the WFO in the study area is a portion of the McKerr Intrusives, a unit composed of lithologically distinct eastern and western portions that grade into each other. The 128.3–120.1 Ma eastern McKerr Intrusives includes

diorite, quartz diorite, and quartz monzodiorite, as well as xenoliths of granitic and metasedimentary rocks (Allibone et al. 2009b; Bradshaw and Kimbrough 1991). The eastern McKerr Intrusives are in intrusive contact with the Expedition Pluton and Lake Hankinson Complex to the southeast. The heterogeneous western McKerr Intrusives (118.4–117.7 Ma), are composed of diorite, quartz monzodiorite, tonalite, granodiorite, and monzonite (Schwartz et al. 2017; Allibone et al. 2009b). The McKerr Intrusives are inferred to be in intrusive contact with the Worsley Pluton to the north, and to share both intrusive and faulted contacts with the Misty Pluton to the south.

The Worsley Pluton, emplaced 124–121.8 Ma, consists of a core of two-pyroxene diorite, monzodiorite, and monzonite, and appears rimmed by hornblende diorite (Schwartz et al. 2017; Allibone et al. 2009b). The younger Misty Pluton (116.8–114.2 Ma) contains three main lithologic phases: a two pyroxene ± hornblende diorite and monzodiorite core in the central and western regions of the pluton; a diorite and quartz monzodiorite with relict clinopyroxene in the southern part of the pluton; and, a strongly-foliated hornblende-rich diorite that occurs in a zone along the eastern margin of the pluton (Allibone et al. 2009b). This third lithologic phase is in intrusive and faulted contact with Paleozoic plutons and metasediments to the east, including the Carboniferous plutons described above. The geochemistry of the Western Fiordland Orthogneiss suggests that its magma was at least partially mantle-derived (Decker et al. 2017). These compositional data indicates a link to the mantle, suggesting that the boundary along which the WFO intruded extended to the base of the crust.

Both the Worsley and Misty plutons were emplaced at pressures of approximately 0.5–1.1 GPa, and subsequently subjected to pressures of >1.2 GPa as a result of crustal thickening (Allibone et al. 2009b and references therein;

Bradshaw 1990). These pressures, combined with the heat from the emplacement of the WFO, promoted high-grade metamorphism in both the WFO and its host rock. The depths implied by these pressures are significant because they indicate that the present exposure of the Fiordland arc includes rocks from lower-crustal depths (35–65 km) providing a view of processes from an active magmatic arc (Klepeis et al. 2019). Geobarometric data from the Worsley and Misty Plutons in particular suggest depths of 35–50 km, while the intervening McKerr Intrusives record lower pressures of ca. 0.86 GPa (mid-crustal depths 20–35 km) (Anderson et al. 2019). The structural boundary that is the focus of this project therefore transects multiple levels of the mid–lower crust. The Cretaceous metamorphic history of Fiordland is discussed in greater detail in the following section.

2.1.2 Mesozoic deformation and metamorphism

The rocks of the Median Batholith and their host rocks record several generations of deformation and metamorphic events over the active period of the Fiordland arc. The presence of arc-related plutons indicates that convergence on paleo-Pacific–Gondwana margin was occurring by at least the Devonian (Mortimer et al. 1999). Convergence continued, likely episodically, through the Early Cretaceous when extensional orogenic collapse initiated around 108–106 Ma. A suite of both contractional and extensional structures that accommodated deformation within the Fiordland arc during the Mesozoic are preserved throughout Fiordland.

Contractional phase

Beginning in the early Paleozoic, the paleo-Pacific margin of Gondwana experienced periods of oblique convergence prior to ca. 108 Ma, although deformation related to this convergence is most evident in Early Cretaceous structures. Preserved in

Fiordland are contractional structures that developed between 130 and 108 Ma. Several steeply-dipping ductile shear zones that accommodated sinistral transpression include the Indecision Creek shear zone, Grebe shear zone, and George Sound shear zone (Marcotte et al. 2005; Buritica et al. 2019; Klepeis et al. 2004). These shear zones are aligned roughly parallel to the paleo-Pacific–Gondwana margin and the Cretaceous Fiordland arc (Fig. 2.1). Two structures accommodated thrusting and vertical thickening in the lower crust including the Mt. Daniel shear zone in northern Fiordland and the Caswell fold-thrust belt in western Fiordland (Klepeis et al. 2004; Daczko et al. 2002).

The steeply-dipping transpressional shear zones are situated on preexisting structural boundaries. The Indecision Creek shear zone and Grebe shear zone (formerly called the Grebe mylonite zone, see Scott et al. 2009) both deform the boundary separating Western Province and inboard Median Batholith rocks from the rocks of the outboard Median Batholith (2005; Scott et al. 2009). Inboard (west) of this Paleozoic Gondwanan boundary, the George Sound shear zone primarily deforms the Western Fiordland Orthogneiss, emplaced into the Fiordland arc during the Early Cretaceous. These recent intrusions conceal any obvious crustal boundary, but the belt of Carboniferous plutons along the eastern margin of the Misty pluton, as well as isotopic data suggest that the George Sound shear zone defines a crustal-scale boundary similar to the one defined by the Indecision Creek and Grebe shear zones (Klepeis et al. 2019).

The George Sound shear zone (GSSZ), which is the focus of this project, is defined by steeply-dipping, primarily amphibolite-grade, high-strain fabrics. First described by Klepeis and Clarke (2004) at George Sound, shear fabrics defined by steeply-dipping, NNE- to N-striking foliation have been mapped to the north and south of George Sound, revealing a ~50-km long structure that crosscuts several of

the plutons of the WFO and their host rocks described above. Kinematic indicators within the GSSZ commonly indicate oblique sinistral movement with a west-side-down component of motion. The GSSZ is estimated to have been active from ca. 119–111 Ma (Marcotte et al. 2005).

The intrusion of the Western Fiordland Orthogneiss caused a regional metamorphic event at upper-amphibolite to granulite conditions that affected both host rocks and the WFO itself. Zircon rims in plutons adjacent to the WFO indicate a high-temperature metamorphic event at ca. 120 Ma, coincident with the emplacement of WFO plutons (Hollis et al. 2004). This metamorphism also overprinted preexisting metamorphic assemblages in early-Paleozoic metasedimentary host rocks that record two earlier amphibolite to upper-amphibolite facies metamorphic events at ca. 360 and 330 Ma (Ireland and Gibson 1998). Tectonic loading of the crust via ductile thrusting and sinistral pure-shear dominated shear zones synchronous with the emplacement of several WFO plutons contributed to the development of granulite facies assemblages in parts of the WFO and surrounding host rocks (Clarke et al. 2000; Daczko et al. 2001). The heat from the emplacement of WFO plutons also contributed to their autometamorphism (Hollis et al. 2004). The metamorphism of the WFO and surrounding rocks is particularly relevant to this study because metamorphism was contemporaneous with deformation in the George Sound shear zone.

Extensional phase

Beginning ca. 108 Ma, the Fiordland arc experienced extensional orogenic collapse and the subsequent rifting of Zealandia from Gondwana (Schwartz et al. 2016). Several shear zones exposed in Fiordland provide an early glimpse of the development of this extensional regime. Major extensional structures in Fiordland

include the Doubtful Sound shear zone (e.g., Gibson et al. 1988; Schwartz et al. 2016), Resolution Island shear zone (Betka and Klepeis 2013), Mt Irene shear zone (Scott and Cooper 2006), and Sisters shear zone (Kula et al. 2007). These shear zones are gently-dipping structures that indicate roughly north–south to northeast–southwest extension. The Doubtful Sound, Resolution Island, and Mt Irene shear zones developed in the middle to lower crust at amphibolite facies, while the greenschist Sisters shear zone is an expression of extensional deformation at shallower depths.

Titanite dates from the Doubtful Sound shear zone in western Fiordland indicate that extensional deformation in the lower crust of the Fiordland arc had localized by 108 Ma (Schwartz et al. 2016. The Malaspina pluton, which lies in the footwall of the Doubtful Sound shear zone, experienced granulite facies conditions (920 °C and 1.4–1.5 GPa) and partial melting prior to this localization (Stowell et al. 2014). Although the ages of WFO plutons and extensional structures vary across Fiordland, this example highlights a rapid shift from crustal thickening and transpressional deformation accompanying WFO emplacement to extension and decompression. The initiation of extension in the lower crust was followed by felsic volcanism across New Zealand, which Tulloch et al. (2009) interpret as the result of crustal thinning related to plate reorganization and the breakup of Gondwana.

2.1.3 Cenozoic transpression and exhumation of Fiordland arc rocks

Following the initiation of extensional orogenic collapse, and the opening of the Tasman Sea starting at 83 Ma, part of the continental margin of Gondwana rifted off to become the continent Zealandia (Tulloch et al. 2009). Modern Zealandia

straddles the boundary between the Pacific and Australian plates, between which oblique convergence is accommodated primarily by dextral slip along the Alpine Fault and subduction at the Kermadec and Puyseger trenches to the north and south, respectively (Davey and Smith 1983; King 2000). Subduction of the Australian plate beneath the Pacific plate at the Puyseger trench has resulted in uplift in Fiordland to the northeast since 25 Ma (Sutherland et al. 2000). This uplift is thought to be accommodated by steep reverse faults in the overriding Australian plate, which facilitated the exhumation of rocks from the middle and lower crust (Klepeis et al. 2019). Modern Fiordland exposes rocks from the whole crustal section of the Fiordland arc: upper crust in southwest Fiordland; middle crust in central Fiordland; lower crust in western Fiordland (Klepeis et al. 2019). This recent tectonic history and exhumation is what allows us to study the Paleozoic and Mesozoic history of continental arc magmatism and deformation in Fiordland.

2.2 Shear Zones

Shear zones are tabular zones of localized deformation that separate undeformed or less strained bodies of rock (e.g., Fossen and Cavalcante 2017). In the lower crust where rocks primarily behave plastically in response to stresses, deformation tends to localize into ductile shear zones. Therefore, understanding how ductile shear zones form and evolve is important to understanding the bulk rheology of the lithosphere (Bürgmann and Dresen 2008). In some environments, ductile shear zones may also serve as the lower-crustal counterpart to upper-crustal brittle fault systems, which together can define boundaries that transect the thickness of the lithosphere and accommodate motion between lithospheric blocks (e.g., Teyssier and Tikoff 1998; Vauchez et al. 2012). This thesis focuses on a single shear zone system

that is exposed in Fiordland, recording Early Cretaceous transpressional deformation. This example of a lower crustal shear zone provides an opportunity to explore to the processes that influence the formation and evolution of these structures. The following sections offer background knowledge on shear zone localization processes and architecture.

2.2.1 Strain localization in shear zones

In order for strain to localize, some rocks must be mechanically weaker than those in surrounding regions. These weaker rocks allows strain to accumulate more efficiently, so they preferentially accommodate deformation (Poirier 1980). Weak zones may already exist in deforming regions, or may develop over time via strain-softening processes that create new zones of weak rocks. Whatever preexisting heterogeneities are present or chemical and physical processes are active will influence the ultimate anatomy of the shear zone. Below I will describe how several, but certainly not all, of these factors may influence shear zone development.

Preexisting Structures

In the case in which a heterogeneous body of rock—one containing different types of rock and possibly preexisting fabrics and structures—is deformed, the geometry and type of heterogeneities therein affect the resulting geometry and kinematic style of the shear zone. These heterogeneities influence how a region (microscopic to crustal-scale) initially deforms, as well as how it evolves once progressive deformation reorients fabrics or causes the development of interconnected weak zones (e.g., Carreras 2001; Holyoke and Tullis 2006b; Gerbi et al. 2016; Gardner et al. 2017). Fundamentally, weak zones will often preferentially localize strain because less work is required to deform these regions.

Crustal-scale lithologic and temperature contrasts have been cited as likely factors controlling the localization and architecture of shear zones at a large scale. Such contrasts are inferred to cause of the localization of shear zones in strike-slip fault systems at depth. The temperature contrast in plutonic or metamorphic core complex settings can induce rheological weakening within the hot-to-cold transition zone between, for example, an emplaced pluton and its host rock (Cao and Neubauer 2016). This also highlights the importance of plutonism which is often associated with shear zones, with some suggesting a feedback between deformation and magmatism in crustal scale shear zones (e.g., Brown and Solar 1998; Kruckenberg et al. 2013; Hanmer 1997; Neves et al. 1996). Similarly, the distribution of belts of weak rocks may preferentially localize strain and lead to a variety of shear zone geometries. For example, metasedimentary units helped to localized strain into a complex, anastomosing network of shear zones in the Borborema system of Brazil (Tommasi et al. 1995).

In addition to large-scale lithologic and compositional contrasts, existing primary or tectonic fabrics may also influence the geometry and kinematic style of shear zones. Preexisting tectonic fabrics in crustal-scale zones of deformation can be efficiently reactivated by new phases of deformation (Vauchez et al. 2012). Depending on the orientation of these fabrics relative to the direction of contraction, entirely new structures may also develop. For example, Carreras (2001) notes the development of different patterns of conjugate or parallel shear zones depending on the orientation of a preexisting foliation relative to the direction of contraction. The initial distribution and orientation of weak zones is therefore a major control on the ultimate architecture and style of deformation within shear zones across all scales.

Metamorphism

Metamorphic reactions may significantly affect shear zone evolution because the production of metamorphic minerals may fundamentally alter the mineralogy and rheology of a rock. Metamorphism can promote strain localization via reaction softening, in which the growth of new mineral phases decreases the strength of a rock (Handy 1989; Brodie and Rutter 1985). This may be accomplished via two general routes. The first is through the growth of new, weaker mineral phases that easily deform (Stünitz and Tullis 2001). In the case of fluid-mediated metamorphic reactions, the production of hydrous minerals like micas may promote the localization of strain at the microscale into shear bands (Holyoke and Tullis 2006a). The second possible pathway for reaction softening is a result of the fact that neocrystallized phases have a finer grain size, which may promote deformation via a more efficient micro-mechanism such as grain boundary sliding and grain boundary migration (Stünitz and Tullis 2001). Metamorphic reactions may therefore help to both nucleate shear zones and promote further localization as a shear zone develops.

There is a strong relationship between metamorphism in shear zones and the presence of fluids. By themselves, fluids in deforming rocks have been noted to physically weaken rocks by enhancing diffusion creep, allowing rocks to deform more efficiently (Tullis et al. 1996). In addition to this, fluids are important mediators of metamorphic reactions. Shear zones may provide conduits for fluid flow through the crust, enabling fluids to interact with dry rocks that then undergo hydration reactions, or may provide pathways for the removal of fluids that are the product of dehydration reactions in regions undergoing prograde metamorphism (Jamtveit et al. 2016). Fluid flow through fractures and subsequent metamorphism of adjacent rock may also initiate strain localization and nucleate shear zones (Getsinger et al.

2013; Condit and Mahan 2018). Fluids flowing along the boundaries of shear zones may promote further reactions in wall rock, weakening the margins of the shear zone and causing the shear zone to widen (Fossen and Cavalcante 2017; Goncalves et al. 2012). Because metamorphism may alter how strain is localized over time, metamorphic processes contribute significantly to the dynamic rheology of the lower crust (Dumond et al. 2018; Bürgmann and Dresen 2008). Understanding the metamorphic processes at play in a deforming region is therefore critical to understanding how a shear zone system might have evolved.

Chapter 3

The fabrics of the George Sound shear zone

The primary goal of this thesis is to characterize the geometry of the George Sound shear zone (GSSZ) along its 50 km-long exposure, and to describe the fabrics that define the GSSZ at the macro and microscale. This will provide a clearer picture of the architecture and evolution of shear zones in the mid to lower crust, and will bear on our understanding of the relationships between deformation and metamorphism.

The George Sound shear zone, as was introduced in chapter two, comprises amphibolite-grade fabrics that define a steeply-dipping, NNE- to N-striking zone that cross-cuts the Western Fiordland Orthogneiss. Kinematic indicators show sinistral motion with a component of west-side-down movement, and previous work has demonstrated that, at least at Bligh Sound, the GSSZ is a transpressional structure (Moyer 2019). The GSSZ developed during a period of oblique convergence on the Gondwana–paleo-Pacific margin and was active from ca. 119 to at least 111 Ma (Marcotte et al. 2005). Nearby structures of a similar age include the Caswell Sound fold and thrust belt to the west of the GSSZ, and the Indecision

Creek shear zone to the east—another sinistral transpressional structure. Exposures in Fiordland reveal the GSSZ cross-cutting rocks from lower-crustal (35–50 km) to middle-crustal depths (20–35 km; only at George Sound) (Klepeis et al. 2019). Rocks deformed by the George Sound shear zone exhibit a variety of compositions, including dioritic and granitic plutons and paragneisses. The orientation and style of GSSZ fabrics differ with these lithologies, and the GSSZ therefore exhibits significant along-strike variability in its fabric geometry and textures.

Because the expression of the George Sound shear zone at each field area is unique, this chapter is divided into sections that describe the rocks in five different regions of Fiordland. From north to south, these are: Bligh Sound, George Sound, Mary Peaks, Myth Tarn and the Southern Misty Pluton margin (which itself comprises two field areas: Coronation Saddle, and Cozette Burn). In each section, I will outline the structural and petrographic characteristics of the rocks by defining fabric facies. Fabric facies are defined by unique structural and petrologic characteristics, such as apparent strain intensity, metamorphic mineral assemblages, and microstructural characteristics. The properties that define each fabric facies vary between field areas depending on the type of data available. Each section will end with a brief summary linking the structural, petrologic, and, where available, geochemical observations, and providing initial interpretations of deformation processes and conditions. These summaries will also provide interpretations of the relationships between the different fabric facies. Ultimately, the spatial distribution of the different fabric facies will help us define the architecture of the George Sound shear zone.

Chapter three presents data that have been collected over four field seasons since 2005, including our most recent field work in 2019. Each field area provides a different view of the George Sound shear zone system and by presenting these data

together in this work, I can correlate results between field areas to describe the GSSZ on a system-wide scale. Chapter four will then discuss the synthesis of these data, fabric correlations, and interpretations that may be drawn about the behavior and evolution of the entire George Sound shear zone.

3.1 Overview of Methodology

3.1.1 Field Work and Data Collection

During January 2019, we conducted field work in central Fiordland. The two primary field areas relevant to this project are located along the George Sound shear zone where it deforms the margin of the Misty Pluton. I have also drawn in data and samples from past field seasons to provide a larger-scale view of the GSSZ. The 2005 field area at Coronation Saddle and the 2015 field area at Cozette Burn provide a view of the southern extent of the GSSZ, roughly 15 km to the south of 2019 field areas. The field areas at George Sound and Bligh Sound in 2018 provide views of the northern extent of the GSSZ, roughly 10 km and 30 km, respectively, to the north of 2019 field areas. A geologic map of western Fiordland showing the location of all field areas and the variety of lithologic units is shown in figure 3.1. Structural data and samples collected from all of these field areas allow me to establish a broad structural framework for the GSSZ and characterize the fabrics present in the GSSZ at these different locations. Each of these field areas will be described in detail in subsequent sections, but additional structural information reported in the Fiordland 1:250,000 geological map (QMAP) by the New Zealand GNS was also incorporated into the construction of the map of the GSSZ presented here (Turnbull et al. 2010). The location of field sites associated with that work are

presented in a similar map in appendix A.

This project relies on two primary methods: structural analysis of field measurements, microstructural analysis of thin sections cut from oriented samples taken in the field. I also incorporate chemical analysis via energy-dispersive X-ray spectroscopy to look for evidence of chemical changes that accompanied deformation. Structural patterns—patterns in foliation and lineation orientations paired with cross-cutting relationships and absolute age data—are used to correlate fabrics between field areas, and microstructural textures help to distinguish fabrics formed in different deformation events or at different pressure–temperature conditions.

3.1.2 Structural Analysis

The geologic structures present at each field area that are most relevant to this study of the George Sound shear zone include foliation and lineations. Fault planes, slip data, dike orientations, and fold geometry were also measured, but foliations and lineation are the most prevalent and will be the focus of subsequent presentations of GSSZ structure. Foliations and lineations are significant because they are an expression of strain in a rock and can develop in response to deformation. We use the orientation of tectonic foliations and lineations to define the geometry of the GSSZ. This basic structural information provides a framework for interpreting the kinematic, microstructural, and metamorphic characteristics of the various parts of the GSSZ, ultimately providing insights into the processes that formed the GSSZ.

The field work produced measurements of structural features (e.g., foliations and lineations) and oriented hand samples. Structural measurements were acquired by several researchers using compasses. At each field site, multiples measurements of any given feature were collected to assess the variability in orientation of each

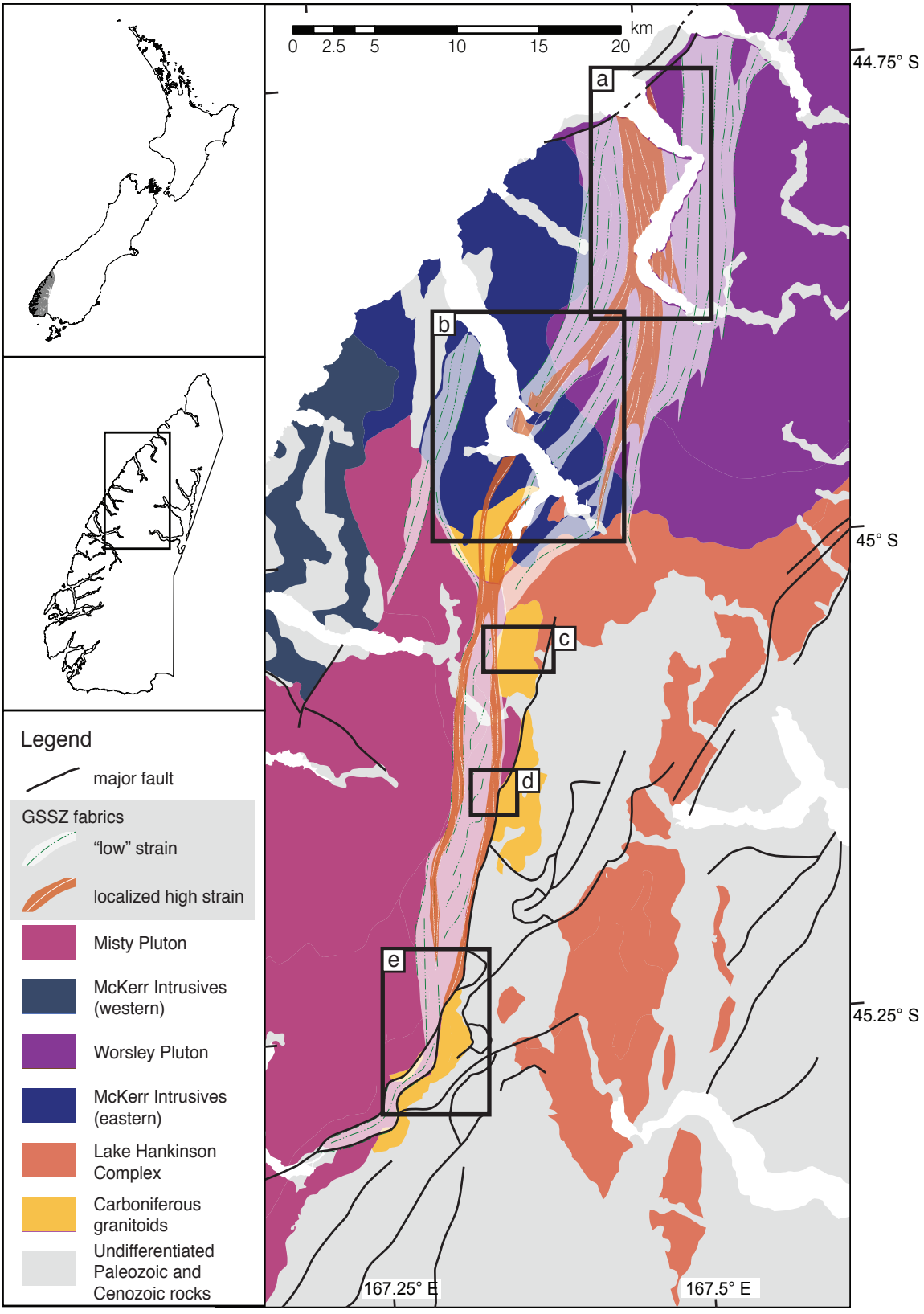
km
0 2.5 5 10 15 20
a
b
c
d
e
44.75° S
45° S
45.25° S
167.25° E
167.5° E
Legend
major fault
GSSZ fabrics
"low" strain
localized high strain
Misty Pluton
McKerr Intrusives (western)
Worsley Pluton
McKerr Intrusives (eastern)
Lake Hankinson Complex
Carboniferous granitoids
Undifferentiated Paleozoic and Cenozoic rocks

Figure 3.1: Simplified geologic map of western Fiordland showing the extent of the GSSZ presented here and the location of field areas relevant to this study. (a) Bligh Sound, (b) George Sound, (c) Mary Peaks, (d) Myth Tarn, (e) Coronation Saddle and Cozette Burn. Lines within GSSZ fabric domains represent foliation trajectories. All maps in this thesis use the NZTM projection. Geologic data are derived from Geology of the Fiordland Area. Institute of Geological & Nuclear Sciences 1: 250,000 Geological Map 17 *n.d.*
.

feature. Hand samples were oriented with respect to north and horizontal so that the orientation of structures contained therein and thin sections cut from the samples could be reset in their original orientation. Data were collected systematically along ridgetops or in fjords that provided transects roughly perpendicular to the strike of the GSSZ.

Foliation and lineation orientations were plotted using lower-hemisphere, equal-area projections in order to visualize patterns in the orientations of structures. In the subsequent sections, I will describe structural data using paired foliation and lineation measurements where paired data are available. This approach avoids the potential pitfalls of treating foliations and lineations as separate, directional data (which involves representing foliation poles and lineations separately as vectors). This also takes into account the fact that foliations and lineations are fundamentally correlated by the fact that lineations develop within foliation planes. Therefore, I combine foliation and lineation pairs and represent each observation as a 3-by-3 rotation matrix composed of three cartesian vectors representing the directions of the pole to foliation, the lineation, and the cross product of the two, following the methodology described by Davis and Titus (2017). Each rotation matrix represents one orientation. These orientations are then treatable using the methods of orientation statistics (Davis and Titus 2017).

Statistical tools

The use of directional and orientation statistics facilitates the analysis of the structural data collected in the field. These tools allow me to characterize data sets with descriptive statistics (e.g., mean and variance of a data set), and to perform statistical inference to quantify the uncertainty in our understanding of statistical descriptors and the relationships between sets of structural data. All statistical analyses presented here were performed using the tools available in the R programming language library *geologyGeometry* created by Joshua Davis (Davis 2019). A more detailed discussion of the statistical tools used here may be found in Davis and Titus (2017) for orientation statistics, and Mardia and Jupp (2009) for directional statistics.

In presenting data and their statistics, I will primarily use two different plots. The traditional equal area, lower-hemisphere spherical projection plot (stereonet) is valuable for visualizing directional datasets. I will complement these with three-dimensional equal-volume spherical plots that enable the visualization of the clustering of orientation data (Davis and Titus 2017; Roberts et al. 2018). When plotting foliation-lineation pairs as orientations using the rotation matrix method described in the previous section, each piece of data is represented by four symmetric points on an equal-volume plot because of the fact that the Cartesian vector that describes a foliation plane or a lineation direction may be negated and still represent the same feature. Therefore, when attempting to describe fabrics with an average foliation-lineation orientation, I check that the orientation data plot as four unimodal clusters on an equal-volume plot. While it is difficult to read the orientation of foliation and lineation pairs from these plots, they complement traditional hemispherical plots by representing the similarities in the orientation of

plane-line pairs. This link between lines and planes may be easily lost in hemispherical plots that present numerous data.

The fabric symmetry of deformed rocks may also bear on which statistical tools it is more appropriate to use. For L-tectonites and L>S tectonites, the lineation is the dominant characteristic of the deformation fabric and it may be more important to understand the orientations of all lineations, rather than to look at paired foliation/lineation orientation data. In rocks where lineation is dominant, paired orientation data will leave out those data for which there are no foliation measurements. In this case, it is more appropriate to use directional statistics to describe the patterns in the lineation data alone. In several cases, orientation statistics are appropriate for some sets of data in a field area, but not others, which may lack paired orientation data or the fabric may be defined primarily by a mineral lineation. In these cases, for the orientation data sets, I perform statistical inference using both orientation and directional methods. Each time I have done this here, the orientation and directional data yield similar results in terms of mean foliation and lineation directions, so I am comfortable then only using bootstrapped 95% confidence ellipses to compare these data to those for which orientation statistics were not applicable.

Statistics that I use to describe the data presented here include the Fréchet mean and variance (for both directions and orientations) and the matrix Fisher maximum likelihood estimates. Briefly, these tools help in the following ways. The Fréchet mean and variance are statistics that describe an average orientation or direction and the amount of scatter in a data set about its mean, respectively. The matrix Fisher maximum likelihood estimate fits a matrix Fisher distribution—a 3D analogue of the normal distribution—to a set of orientation data (Davis and Titus 2017). In a matrix Fisher distribution, the matrix $\mathbf{K}$ describes the dispersion of a

set of rotations. Eigenvalues of the maximum likelihood estimate $\hat{\mathbf{K}}$ then provide a measure of the anisotropy of the samples of orientation data, which is used to inform us about how to proceed with statistical inference.

Generally, statistical inference allows us to quantify how well our samples represent the natural population of fabrics orientations from which they were drawn. Statistical inference here is primarily used to generate 95% credible/confidence regions for orientational and directional data. To do this, I use two methods—Markov chain Monte Carlo (MCMC) and bootstrap simulations—to generate simulated data sets from our measured samples. In both methods, new sample sets are simulated and clouds of simulated sample means are generated—one million in the case of MCMC, and 10,000 in the case of bootstrapping. The centers of these clouds are an estimate of the mean orientation or direction of a population of fabrics, and the closest 95% of these simulated means define a 95% credible region when using the MCMC method, and a 95% confidence ellipse when using the bootstrap method (Davis and Titus 2017).

For directional data sets, I use the bootstrapping method. Bootstrapping involves constructing simulated data sets by resampling from the original data set with replacement. This method relies on the frequentist interpretation of statistics, and so the result is a traditional 95% confidence region for the population mean. For orientation data sets, I use the Markov chain Monte Carlo (MCMC) technique to simulate sample data sets. The MCMC technique is a method from Bayesian statistics and produces a 95% credible region. The 95% credible region may be interpreted as a region that has a 95% probability of containing the population mean. The MCMC simulations, however, assume that the sample data are drawn from a wrapped trivariate normal distribution—another 3D analogue of the normal distribution. The MCMC technique as applied to geologic orientation data is

described in more detail in Davis and Titus (2017). Both credible and confidence regions allow us to engage in hypothesis testing to assess whether sample data sets could be drawn from the same population of orientations or directions. Given two samples of fabric measurements, two-sample hypothesis tests test the null hypothesis that the orientations from each domain are sampled from populations with the same mean orientation. In practice, non-overlapping 95% confidence/credible regions as viewed on a stereonet or equal volume plot lead us to reject the null hypothesis at 95% confidence. In that case, we may say that the orientations of the two sets of fabrics are significantly different. Geologically, this allows us to clarify the differences between fabric populations and to quantify our uncertainty in how different the fabric populations may be.

I have also applied geodesic regressions to some sets of foliation poles (directional data) here. This type of regression is useful for fabric orientations that are associated with geographic locations (i.e., field site UTM coordinates), and allows us to test the spatial dependency of fabric orientations—for example if there is a progressive rotation of foliation dips along a given transect (Davis and Titus 2017). This simple regression fits a geodesic curve, which for directional data is simply a great circle arc on a stereonet, with an associated rate of rotation along it. For the data used here, rotation along a geodesic may also be reported as rotation about an axis at a rate with units degrees per kilometer. Geologically, this means that for some hypothetical spatially-dependent foliation data, we could conduct a regression that tells us that for every kilometer along the azimuth we ran the regression, we might expect that foliation poles will rotate by n degrees about some axis. The regression also provides an R^2 statistic that quantifies how well the regression explains the provided data, with a perfect fit represented by $R^2 = 1$.

To test the significance of a geodesic regression, I also perform a permutation

test. Permutation tests randomly permute the geographic component of the data (e.g., distance along a given azimuth), re-run the regression, and compute its R^2 value. The new, randomized geographic components do not have a meaningful relationship with the orientations. Thus, if the new R^2 value is greater than the R^2 of the original regression, the original relationship described by the regression must also not be meaningful. A number of permutation tests are run (10,000 are used in this study), and the fraction of these that produce R^2 values greater than the original R^2 represents a p-value. In this case, we are testing the null hypothesis that there is no dependence of orientation on distance along the given azimuth.

3.1.3 Petrographic Analysis

Petrographic analysis helps to more thoroughly characterize the composition and metamorphic and deformation textures of a rock. The microscopic textures of deformed rocks—particularly those of quartz and feldspars—provide insight into the temperature conditions of deformation (e.g., Stipp et al. 2002). Metamorphic textures enable us to infer the metamorphic reactions experienced by these rocks. Where metamorphic minerals define deformational structures, we may further correlate metamorphic and deformation processes. These observations from the millimeter to micron scale inform our understanding of the processes of deformation, and thus the conditions under which deformation occurred, which we may then extrapolate to larger scales to better understand the behavior of meter to kilometer scale shear zones.

Hand samples collected in the field were oriented to preserve information about the orientation of features within the samples. Billets for thin sections were cut from samples such that thin sections are oriented perpendicular to foliation and, in samples containing a lineation, parallel to lineation. From these billets, polished

thin sections were produced, which I analyzed using polarized light microscopy.

3.1.4 Geochemical Techniques

Metamorphic processes may alter the composition of minerals contained within a rock and promote the growth of entirely new minerals. If metamorphic processes occur in concert with deformation, we may expect to see variations in mineral assemblage and composition that coincide with variations in structural patterns. To look for evidence of this in the George Sound shear zone, I determined the composition of a variety of minerals in samples from across our field areas using energy dispersive x-ray spectroscopy (EDS).

Selected thin sections were analyzed on the Tescan Vega 3 LMU Scanning Electron Microscope (SEM) with an Oxford Instruments Energy Dispersive Spectrometer at Middlebury College. An accelerating voltage of 20 kV and beam intensity of 18 was used for all analyses. The EDS technique allows for the determination of the relative abundances of chemical elements in rock samples. EDS cannot reliably quantify light elements, nor can it determine the valence state of elements, so we lack information on the OH content of minerals and the valence state of iron, both of which are important for accurately categorizing some minerals. However, the major element data that are provided are useful in estimating relative changes in mineral composition between different fabrics in the same rock type. In the following sections, I will only describe the results from Bligh Sound where I have good mineral composition data from each fabric facies. The raw, quantified EDS mineral composition data for all the mineral X-ray spectra I acquired from samples from Bligh Sound are presented in appendix B.

3.2 Bligh Sound

Bligh Sound exposes rocks of the dioritic Worsley Pluton that have been deformed in the George Sound shear zone. In this area, the GSSZ is discernable by a strain gradient that juxtaposes a zone of more highly-strained rocks against rocks of lower-strain, each with different fabric shapes (oblate vs. prolate), and by the presence of mylonitic and asymmetric fabrics.

A description of the geology of Bligh Sound with special attention paid to the George Sound shear zone was first undertaken by Moyer (2019). Moyer defined distinct structural domains based on shape fabric symmetry—determined by calculating a shape fabric ellipsoid for different rock samples, which provides an estimate of the finite strain ellipsoid—and petrographic characteristics. The Bligh Sound field area (Fig. 3.2) provides a unique opportunity to study the GSSZ where it transects a relatively homogeneous dioritic pluton. This is in contrast with the field areas that will be discussed later, where multiple lithologies have been deformed. The relative homogeneity of the Worsley Pluton enabled Moyer to compare his results to theoretical studies of ductile shear zones that assume deformation of a homogeneous medium.

In this section, I will summarize the structural domains first defined by Moyer and present a more rigorous statistical analysis of the structural data he presented. My statistical results ultimately prompt me to reclassify some of the data presented by Moyer into different domains. Finally, I will also present analyses of the composition of the minerals within each structural domain.

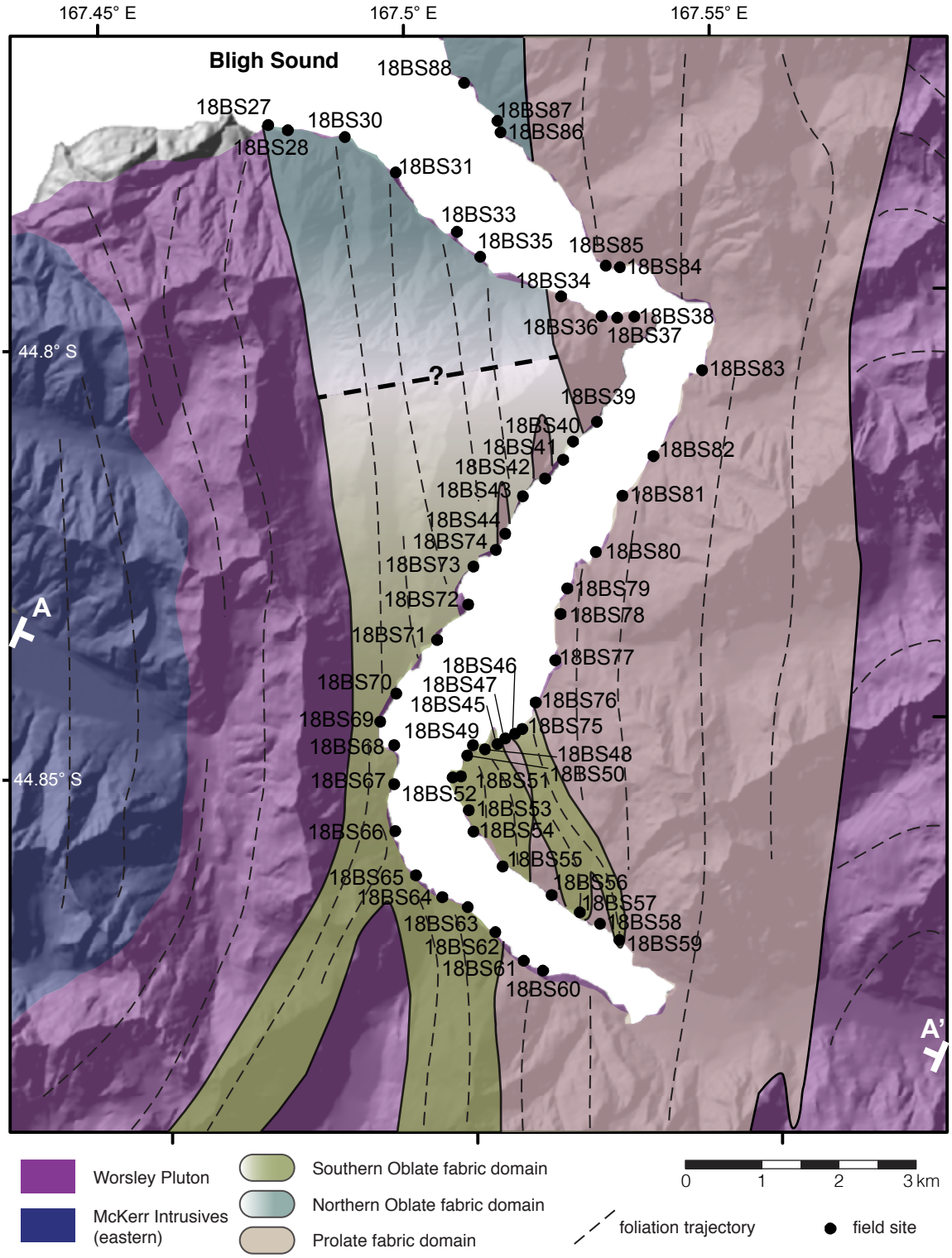
167.45° E
167.5° E
167.55° E
Bligh Sound
18BS88
18BS27
18BS30
18BS28
18BS87
18BS86
18BS31
18BS33
18BS35
18BS85
18BS84
18BS34
18BS36
18BS38
18BS37
44.8° S
?
18BS83
18BS39
18BS40
18BS41
18BS82
18BS42
18BS43
18BS81
18BS44
18BS74
18BS80
18BS73
18BS72
18BS79
18BS78
A
18BS71
18BS77
18BS46
18BS70
18BS47
18BS76
18BS45
18BS69
18BS75
18BS49
18BS68
18BS48
44.85° S
18BS67
18BS51
18BS50
18BS52
18BS53
18BS66
18BS54
18BS55
18BS65
18BS56
18BS64
18BS57
18BS63
18BS58
18BS62
18BS59
18BS61
18BS60
A'
Worsley Pluton
McKerr Intrusives (eastern)
Southern Oblate fabric domain
Northern Oblate fabric domain
Prolate fabric domain
0
1
2
3 km
foliation trajectory
field site

Figure 3.2: Detail map of Bligh Sound showing stations of 2018. The spatial extent of fabric facies is outlined here. It is also likely that low-strain fabrics are present to the west of the oblate zone based on available foliation measurements. The nature of the transition between the northern and oblate domains, denoted by a dashed line and question mark, is unknown. Hillshade models in this thesis based on NZ 8m Digital Elevation Model (2012) *2016.*

3.2.1 Fabric facies

Bligh Sound dissects the western part of the Worsley Pluton, which is primarily a two-pyroxene diorite. Locally, the rocks of the Worsley Pluton are composed of plagioclase + orthopyroxene + clinopyroxene + potassium feldspar ± amphibole + oxides ± biotite ± quartz. Plagioclase is the dominant matrix constituent of these rocks, with mafic aggregates and grains suspended therein. Layers of garnet pyroxenite and hornblende diorite are also present in the northern reaches of Bligh Sound.

The center of the Worsley Pluton is dominated by the igneous two-pyroxene diorite described by Allibone (2009), but at Bligh Sound, the Worsley Pluton experienced at least upper-amphibolite facies conditions. Metamorphism is evidenced by microscopic textures suggesting the growth of pyroxene minerals on primary igneous pyroxene. In rocks deformed by the George Sound shear zone, the presence of metamorphic amphibole and biotite also suggests that retrograde hydration reactions occurred in sections of the Worsley Pluton.

Undeformed samples of the Worsley Pluton were collected in 2019 from the eastern margin of the pluton. These rocks exhibit igneous textures such as euhedral feldspar crystals, but on the micro-scale also exhibit retrograde metamorphic textures such as hornblende rims on pyroxene. In rare samples, a very weak foliation defined by the alignment of plagioclase laths and mafic aggregates is visible. These undeformed samples primarily serve as a benchmark for undeformed textures that

developed outside of the George Sound shear zone, and for understanding how metamorphism may have variously affected different parts of the Worsley Pluton.

Deformed rocks of the Worsley Pluton at Bligh Sound exhibit penetrative gneissic, L-tectonite, and protomylonitic to mylonitic fabrics. Lineations are typically defined by mafic phases—pyroxene, hornblende, and biotite—that are formed into elongate aggregates. Asymmetric shear-sense indicators including sigmoidal and deltaic porphyroclasts, hornblende fish, and S-C fabrics within mylonitic rocks consistently indicate down-to-the-southwest shearing. The tectonic fabrics at Bligh Sound that define the George Sound shear zone are generally steeply-dipping, N- to NW-striking foliations with lineations that generally plunge steeply to moderately to the south, southwest, and west (Fig. 3.3 a). Fabric orientations combined with the shear sense indicators suggest oblique sinistral motion of rocks on either side of the George Sound shear zone at Bligh Sound.

When the orientation data are presented colored by their geographic location (Fig. 3.3 c), there is some discernible dependency of fabric orientation on location. Clusters of data of similar colors appear with varying degrees of overlap, suggesting that fabrics with different orientations exist in different parts of Bligh Sound. The spatial variability in fabric orientation also correlates with spatial variability in shape fabric symmetry and microstructural characteristics, as was originally noted by Moyer (2019) and will be discussed below. By grouping data from stations into structural domains, we may analyze how fabric orientation varies with mineral assemblage, strain symmetry and strain magnitude. This allows us to suggest links between variability in shear zone geometry and variability in the processes of deformation in the George Sound shear zone.

The results of finite strain analysis prompted Moyer to define four separate structural domains at Bligh Sound. Spatially, these domains define two N-S trending

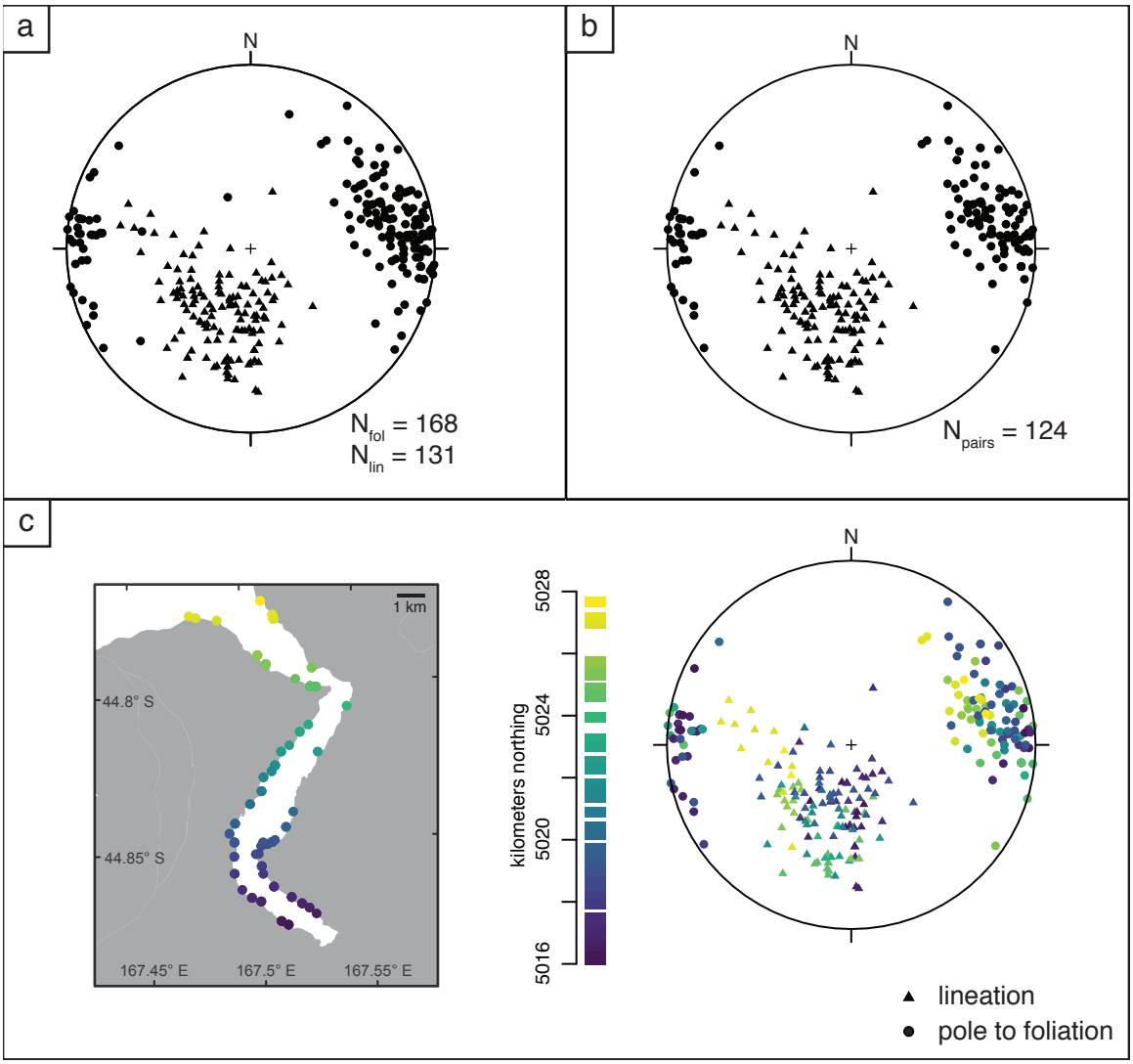

Figure 3.3: Foliation and lineation data from Bligh Sound plotted on stereonets. (a) all foliation and lineation data. (b) Foliation/lineation pairs representing the subset of the data used for orientation statistics. (c) Paired orientation data colored by geographic location—in this case, by the UTM northing value of the station at which the data were collected. In th simplified map of station locations at left, the station colors corresponding to the color of the corresponding data.

zones: one in which rocks exhibit prolate shape fabrics and one in which oblate fabrics dominate. The oblate domain lies to the west of the prolate domain and may be further divided into at least two additional domains based on microstructural properties. A northern oblate domain contains syn-tectonic hornblende while a southern oblate domain contains biotite shear bands. Moyer (2019) suggested an additional central oblate domain, although there is little geological evidence indicating that the rocks and structures in the central oblate domain differ significantly from those in the southern oblate domain. A statistical test of whether or not the orientational data from these domains significantly differ is discussed in a later section. A brief summary of the finite strain analysis of Moyer follows below, followed by details of the three main structural domains present at Bligh Sound.

Finite strain analysis paired with petrographic characterization of fabrics allowed Moyer to distinguish between fabrics of the George Sound shear zone that are distinct in their shape fabric symmetry, relative strain magnitude, and/or the minerals that define shear fabrics. Details on the determination of shape fabric symmetry and strain magnitude can be found in Moyer (2019). Figure 3.4 presents the results of the R_f/ϕ method of determining the finite strain ellipsoid for fourteen samples from Bligh Sound, plus two samples from the undeformed margin of the Worsley Pluton (19HB85D and 19HB89B). These data show that there are two sets of shape fabrics at Bligh Sound: a prolate population and an oblate population.

The classification of fabrics at Bligh Sound takes on a hierarchical structure. At the highest level, fabrics are classified based on their shape fabric symmetry as either prolate or oblate. In the field, oblate fabrics were observed to be protomylonitic to mylonitic. Within in the oblate domain, we may further subdivide fabrics into two populations based on the syn-kinematic metamorphic minerals present. As will be shown below, these final two oblate populations also differ in the

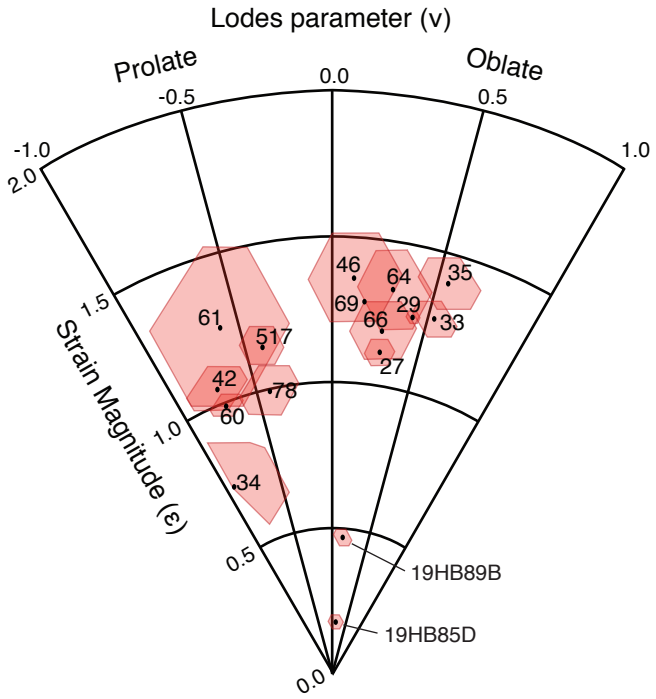

Figure 3.4: Nadai-hsu plot of the results of the R_f/ϕ method of finite strain analysis applied to samples from the Worsley Pluton by Moyer (2019). Points on the diagram represent finite strain ellipsoids and are parametrized by an angular component, the Lode's parameter, and a radial component, a measure of the magnitude of strain. The former quantifies the anisotropy of the shape of an ellipsoid, and the latter is proportional to the octahedral shear strain, which may be thought of as a measure of the average distortion of material lines (Vollmer 2018; Brandon 1995). Red regions represent 95% confidence regions determined by bootstrapping ellipsoid data. Two sets of shape fabric ellipsoids representing different populations of fabrics at Bligh Sound are apparent. Adapted from Moyer (2019).

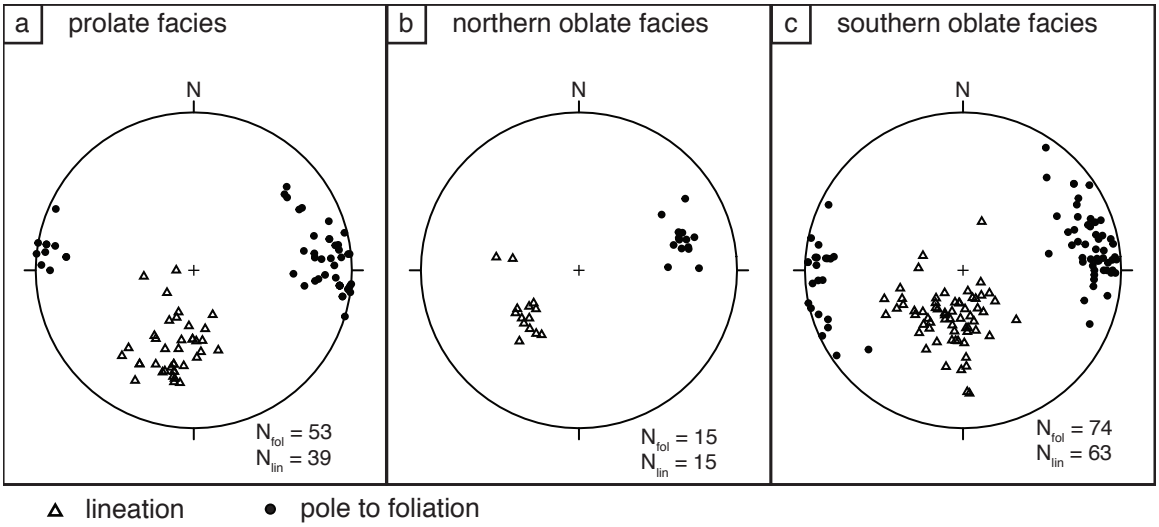

Figure 3.5: Stereonet plots of foliation and lineation directions—including both paired and unpaied data—from the three fabric facies present at Bligh Sound.

orientation of their foliations and lineations, which are distinct from the orientation of fabrics in the prolate domain as well. We make no further subdivisions of prolate fabrics. In all cases where shear sense indicators are present—in both the field and in thin section—sinistral-oblique, top-down-to-the-southwest shear sense is evident in each domain. The details of field structural measurements and microstructural observations are described in further detail below. The orientations of fabrics in each facies are presented in the stereonets in figure 3.5 to enable comparisons between facies.

Prolate Fabrics

The prolate domain as defined by Moyer is characterized by relatively low-strain, L>S fabrics in which metamorphic pyroxene appears to have developed syn-kinematically. Shape fabric analysis of samples from this domain yields prolate shape fabric ellipsoids. Foliations are steep to subvertical, striking N–S, with lineations plunging moderately to steeply to the south (Fig. 3.5 a).

The mineralogy of rocks in this domain is dominated by plagioclase, clinopyroxene, orthopyroxene, and potassium feldspar, with opaque oxides (primarily ilmenite) and minor hornblende also present. Clinopyroxene rims and asymmetric tails on orthopyroxene grains indicates that some of the pyroxene present in the sample is metamorphic. Similarly, where present, hornblende appears on the margins of pyroxene aggregates. These texture indicate the metamorphic growth of pyroxene and amphibole, which is indicative of upper-amphibolite to granulite facies conditions.

In thin section, microstructures indicate that metmorphism and deformation progressed in concert and are suggestive of the temperatures at which the prolate fabric developed. Elongate aggregates of orthopyroxene and clinopyroxene are present in all prolate samples, and all contain evidence for the metamorphic growth of clinopyroxene. Elongate aggregates of recrystallized ortho- and clinopyroxene, and asymmetric tails of clinopyroxene on orthopyroxene indicate contemporaneous metamorphism and deformation (Fig. 3.6 a, b). The grain boundaries of plagioclase grains that comprise the matrix of the prolate samples show cuspate-lobate textures indicative of high-temperature deformation (Fig. 3.6 c, d). Anti-perthitic textures within plagioclase grains are common in these samples.

Asymmetric kinematic indicators are not apparent in most prolate samples at the micro-scale. Only 18BS60A, which is derived from a pod of rocks with prolate fabrics surrounded by rocks of the southern oblate facies, exhibits asymmetric porphyroclasts. Otherwise, pyroxene aggregates are elongate and may be up to one centimeter long. Aggregates are composed of orthopyroxene, clinopyroxene, ilmenite, and rarely hornblende. Commonly, clinopyroxene appears to be replacing orthopyroxene (Fig. 3.6 b). When present, hornblende is aligned with the pyroxene aggregates. Hand samples from the prolate domain exhibit weakly asymmetric

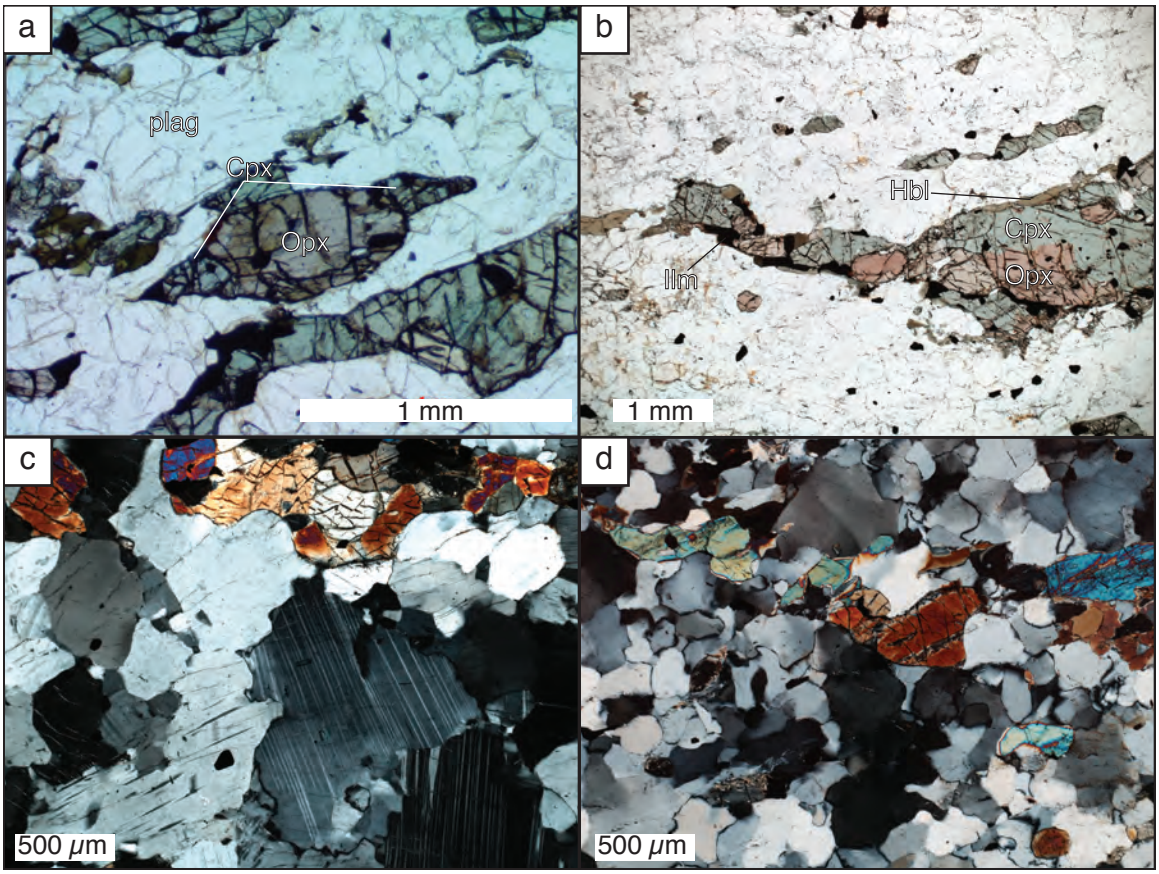

Figure 3.6: Microstructures in prolate samples. (a) Cpx tails on Opx grain in sample 18BS60 (from Moyer, 2019) (b) tail of recrystallized pyroxene, hornblende, and opaques on a pyroxene aggregate in sample 18BS78. Cpx appears to be replacing Opx within the aggregate and a rim of hornblende is present on the Cpx. (c) cuspate-lobate grain boundaries in plagioclase and anti-perthitic exsolution textures in sample 18BS42. (d) cuspate-lobate grain boundaries in matrix plagioclase and a trail of pyroxene, hornblende and opaques at top of image in sample 18BS78.

fabric elements that indicate top down-to-the-SW shear sense.

Isolated sections of rocks exhibiting prolate fabrics—which we refer to as prolate pods—appear within the oblate zone and are separated from the prolate zone to the east by rocks with oblate fabrics. The existence of prolate pods is inferred from the presence of field sites at which prolate fabrics are present, but oblate fabrics dominate at adjacent field sites to the east and west. Prolate pods may therefore be on the order of tens of meters in width (measured perpendicular to shear zone strike). The rocks within these pods exhibit the prolate, L-tectonite fabrics defined by pyroxene aggregates, consistent with rocks from the main prolate zone to the east. In thin section, however, samples from these prolate pods display mineralogical assemblages and microstructures more closely-resembling those of oblate samples.

Northern Oblate Fabrics

The northern part of the zone of rocks with oblate shape fabrics is characterized by S > L tectonites in which metamorphic hornblende appears to have grown on pyroxene aggregates syn-kinematically. Shape fabric analysis of samples from this domain yields oblate shape fabric ellipsoids of similar or higher strains than those in the prolate domain. Foliations dip moderately to the WSW and contain lineations that plunge moderately to the SW (Fig. 3.5 b).

Rocks in the northern oblate domain are composed of plagioclase, clinopyroxene, orthopyroxene, potassium feldspar, hornblende, and opaque oxides. Hornblende tails and corona on pyroxene aggregates indicate the metamorphic growth of hornblende as a result of hydration reactions. Similar to the rocks of the prolate domain, the presence of pyroxene and the growth of hornblende indicates that these rocks have experienced at least upper-amphibolite conditions. However, the amount of metamorphic hornblende in the northern oblate domain is significantly greater than

that of the prolate domain, suggesting a greater degree of hydration in this part of the George Sound shear zone.

In thin section, the rocks of the northern oblate domain are characterized by the presence of hornblende-defined microstructures adjacent to pyroxene grains. Syn-kinematic hornblende is apparent in asymmetrical tails on pyroxene porphyroclasts and aggregates, and in shear bands that developed on the margins of pyroxene grains, sometimes forming chains of pyroxene aggregates connected by hornblende shear bands (Fig. 3.7 a). Tails of Cpx are common on pyroxene aggregates and some Cpx rims appear on Opx grains (Fig. 3.7 b). Plagioclase in the matrix of samples from the northern oblate domain commonly exhibits interlobate grain shapes with cuspate-lobate grain boundaries, and grain-size reduction of plagioclase is common near hornblende shear bands (3.7 c). Plagioclase grains may also encompass trains of oxides or biotite. A strong lattice-preferred orientation of plagioclase crystals is also present in the matrix of some northern oblate samples.

Southern Oblate Fabrics

The southern oblate domain is characterized by S > L tectonites in which metamorphic biotite and hornblende appear to have developed on pyroxene syn-kinematically and have organized into shear bands. There is no obvious indicator of a transition zone between the northern and southern oblate domains. The shape fabric ellipsoids calculated for samples in this domain do not indicate significantly higher or lower strains than those of the northern oblate domain, which are similar to or greater than the magnitudes recorded by the prolate shape fabric ellipsoids. Rocks from the south of the oblate zone primarily differ from those to the north in their microstructural characteristics and fabric orientations. Foliations are steep–subvertical and strike to north and northwest and contain lineations plunging

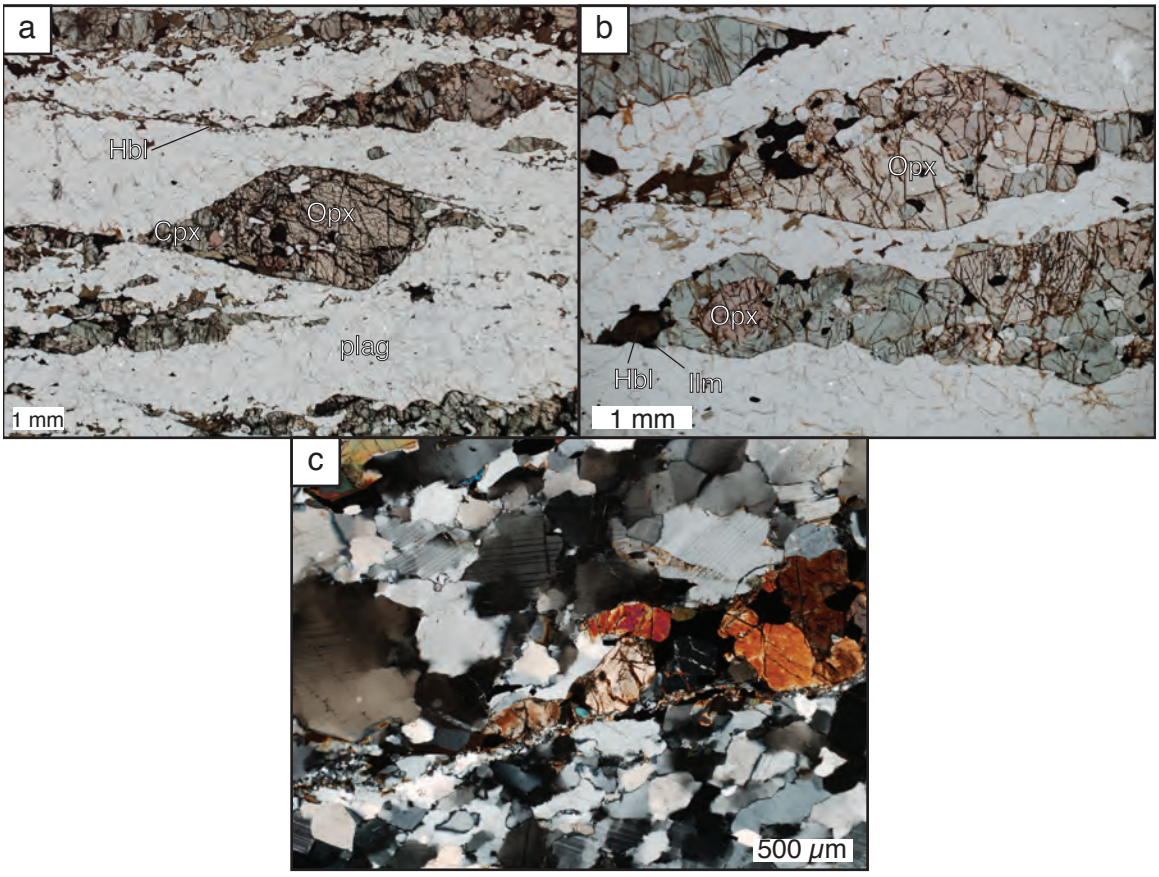

Figure 3.7: Microstructures in 18BS35A from the northern oblate domain. (a) asymmetric Opx porphyroclast with Cpx + Hbl tails. (b) Opx aggregates with Cpx, Hbl, and opaque tails; Cpx rim on Opx grain visible bottom left. (c) Plagioclase microtexutres and a hornblende shear band. Coarser plagioclase at the top of image exhibits lobate grain boundaries, and there is a reduction in plagioclase grain size closer to the hornblende shear band that cuts through the image.

steeply to the south and southwest (Fig. 3.5 c).

The southern oblate domain contains amphibolite-facies rocks composed of plagioclase, orthopyroxene, clinopyroxene, potassium feldspar, hornblende, biotite, and opaque oxides. Metamorphic hornblende and biotite are present primarily in tails on pyroxene grains and aggregates. These hydrous minerals are in greater abundance than in the northern oblate domain, suggesting a greater degree of hydration of southern oblate domain rocks. Biotite also appears in minor quantities within the plagioclase matrix.

A greater degree of strain localization on the micro-scale is apparent in the southern oblate domain compared to either the northern oblate or prolate domains. Shear bands are pervasive in thin sections from this domain, and contain fine-grained hornblende, biotite and quartz (Fig. 3.8). This is in contrast with the northern oblate domain in which shear bands appear less frequently and are dominated by hornblende alone. Shear bands appear to trail off of large (> 3 mm) orthopyroxene grains—sometimes mantled by smaller ortho- and clinopyroxene grains—or smaller, elongate aggregates of equant ortho- and clinopyroxene (Fig 3.8 a, b). Adjacent to shear bands, plagioclase displays significant grain-size reduction. Away from shear bands, coarser plagioclase grains have irregular grain shapes, exhibit subgrain domains and bulging grain boundary textures, and share a strong lattice-preferred orientation (Fig. 3.8 c, d).

Pods of the prolate fabrics are also found within the oblate domain. Samples 18BS60 and 18BS61 both exhibit prolate shape fabric ellipsoids, but are derived from within the southern oblate domain. Both samples, however, have well-developed asymmetric fabrics and syn-kinematic hornblende and biotite, comparable to the rest of the southern oblate domain.

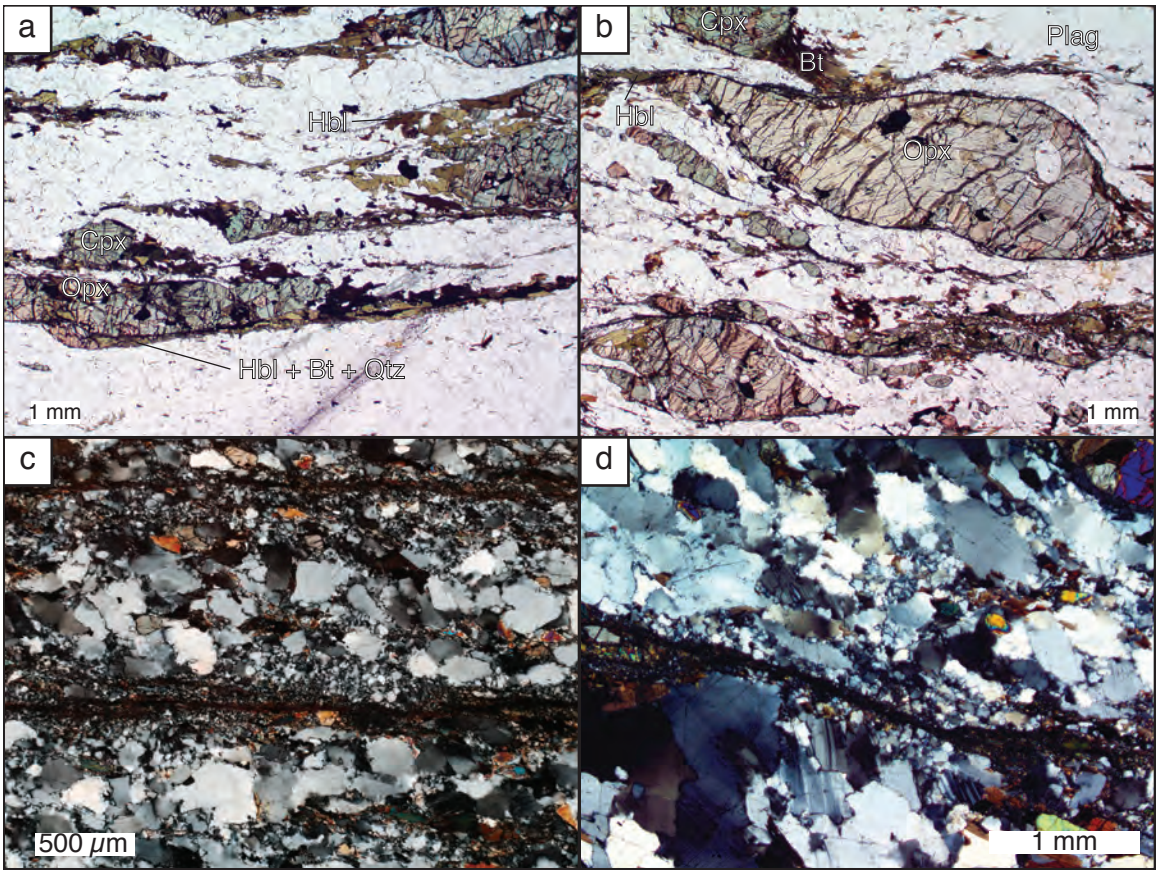

Figure 3.8: Microstructures in samples from the southern oblate domain. (a) hornblende, biotite, and quartz shear bands originating on Opx grains in pyroxene aggregates in 18BS64A. (b) at top: Cpx-dominated aggregate with biotite tails; at center: large, deformed Opx grain mantled by Cpx with Hbl + Bt shear bands; at bottom left: sigmoidal Opx + Cpx aggregate with recrystallized tails of pyroxene and hornblende; 18BS69A. (c) shear bands separated by domains of coarser plagioclase that is grain-size reduce closer to the shear bands; 18BS26A (d) plagioclase bulging and subgrain textures in 18BS69A.

3.2.2 Statistical Analysis

The statistical tools introduced earlier in this chapter provide a means of further quantifying the orientations of fabrics in the George Sound shear zone and the differences between different sets of fabrics. Statistical inference also allows us to quantify our uncertainty in the data and to perform hypothesis tests. For data derived from Bligh Sound, I apply these tools to fabric orientation data separated into the fabric facies defined above.

The orientation data are plotted in equal volume plots in figure 3.9 and are paired with stereonet plots of the same paired foliation/lineation data. Because the populations of orientations within each domain are roughly unimodal, the Fréchet mean and variance are appropriate statistical descriptors of the data. I also perform a matrix Fisher maximum likelihood estimation of the orientation data sets for each domain. A summary of all of these statistics for each domain is presented in table 3.1. Based on the results of the matrix Fisher maximum likelihood estimate, we opt to use the MCMC approach to statistical inference following the recommendations of Davis and Titus (2017).

The original domains defined by Moyer (2019), included a central oblate domain in addition to the northern and southern oblate domains. However, statistical hypothesis tests do not suggest that the fabric orientations from this domain differ significantly from those of Moyer's original southern oblate domain. I performed MCMC simulations on the data from the original central and southern domains to conduct a two-sample hypothesis test. The MCMC simulations allow me to construct 95% credible ellipsoids which are shown in figure 3.10a in an equal volume plot, and projected onto a lower hemisphere stereonet in figure 3.10b. The 95% credible ellipsoids overlap, which does not allow us to reject the null hypothesis that

Fabric Facies	N_{fol}, N_{lin}, N_{pairs}	Fréchet Mean Strike/Dip Rake	Fréchet Variance	$\hat{\mathbf{K}}$ eigenvalues from matrix Fisher MLE
Prolate	53, 39, 36	179/79 50 SW	0.09	25.6, 11.3, 7.5×10^{-7}
Northern Oblate	15, 15, 14	164/57 78 SW	0.04	73.8, 23.5, 2.7×10^{-6}
Southern Oblate	74, 63, 60	171/81 66 SW	0.10	16.1, 8.6, 2.1
		original divisions of Moyer, 2019:		
Central Oblate	51, 45, 44	171/83 67 SW	0.11	13.7, 8.3, 1.9
Southern Oblate	23, 18, 16	173/75 63 SW	0.06	56.8, 12.4, 1.7×10^{-6}

Table 3.1: Statistical descriptors of fabric orientations at Bligh Sound.

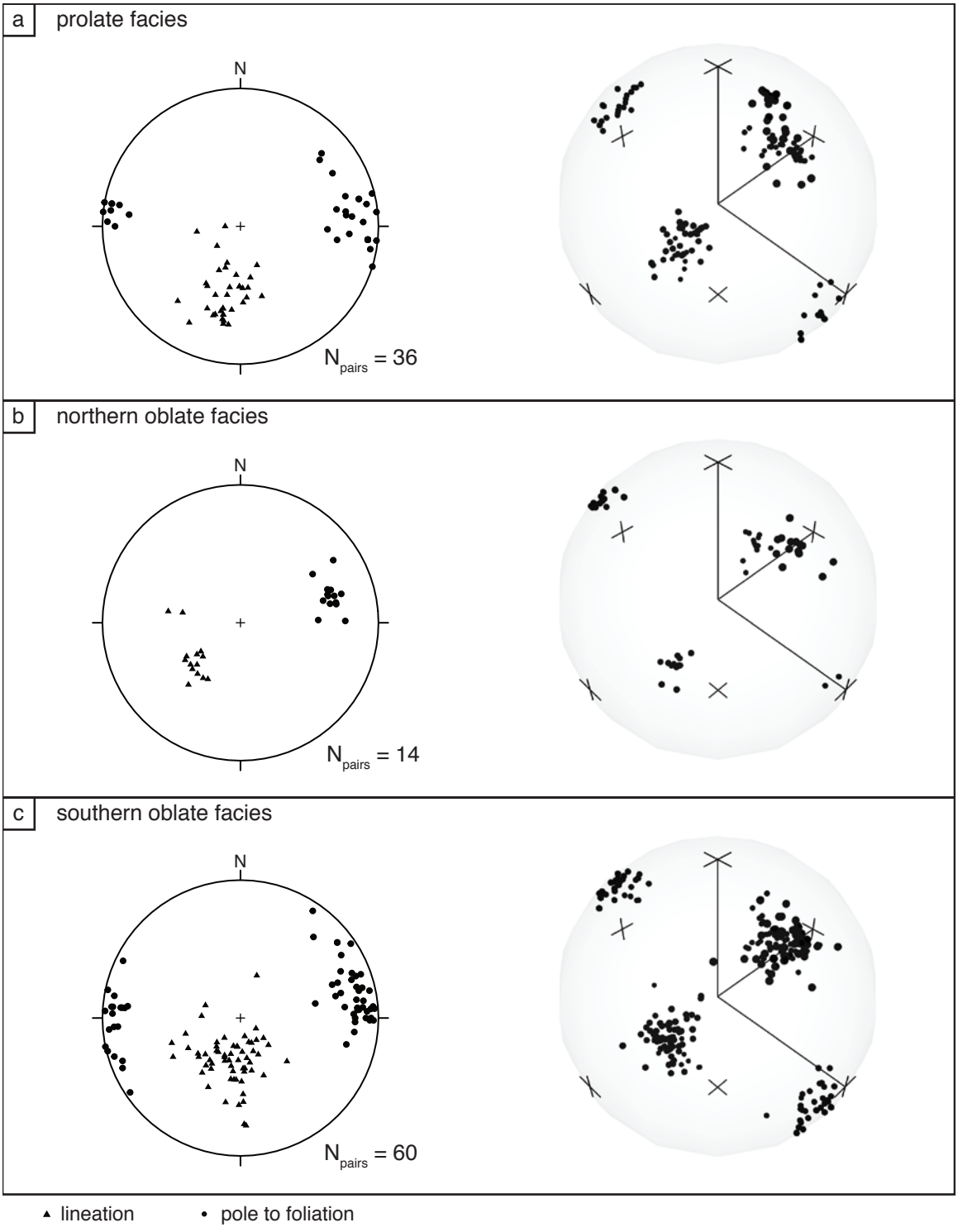

Figure 3.9: Equal volume plots and lower-hemisphere stereonets of the paired foliation/lineation orientations from each fabric facies at Bligh Sound to demonstrate the clustering of paired foliation/lineation measurements from each facies.

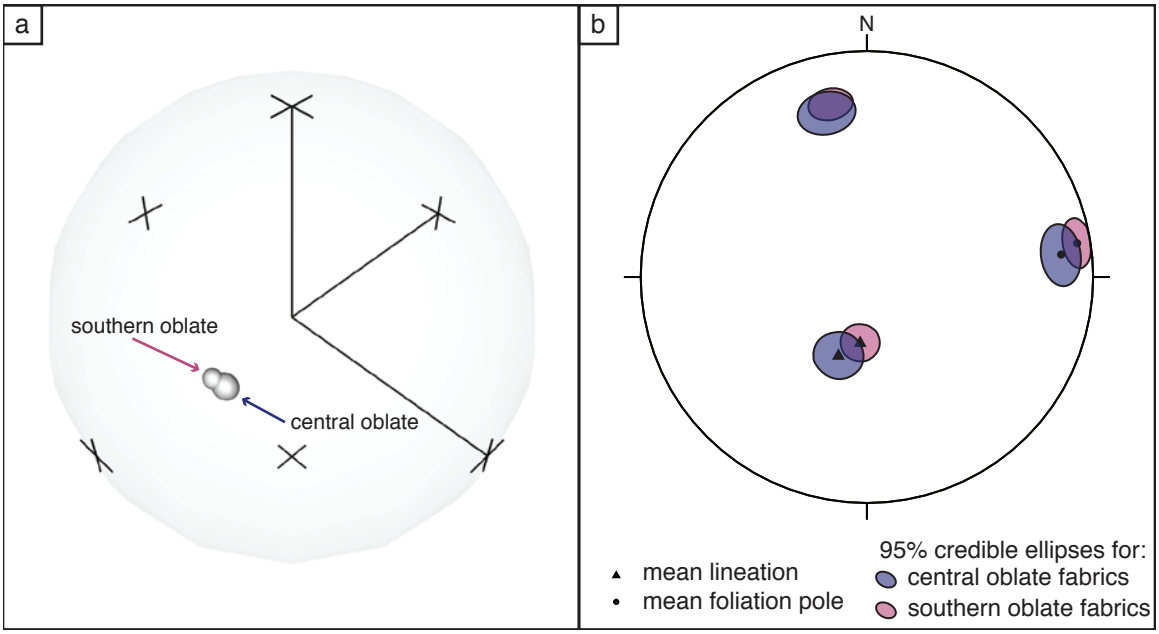

Figure 3.10: (a) The equal volume plots shows two 95% credible ellipsoids determined via MCMC simulations of the paired foliation/lineation orientation data from the central and southern oblate domains of Moyer (2019). Because of the overlap between these ellipsoids, the two-sample hypothesis test fails to reject the null hypothesis that these datasets are drawn from populations with the same mean orientation. In (b), these credible ellipsoids are projected onto a lower-hemisphere stereonet and appear as three ellipses with mean foliation and lineation directions plotted.

the orientations from the central and southern domains were drawn from the populations with the same mean orientation. In lieu of any other geologic evidence—no finite strain analyses were conducted on samples from the central domain, no thin sections or hand samples are available to discern lithologic differences, and notes of field observations do not suggest significant differences between stations of the southern and central domain—I therefore opt to combine the data from field sites originally split between the central and southern domains by Moyer. Throughout the preceding and subsequent parts of this section, I have combined the data from the central and southern domains and simply referred to these as the southern oblate domain.

With the remaining simplified fabric facies—prolate, northern oblate, and

southern oblate—I also generate 95% credible regions for the mean foliation/lineation orientations via MCMC simulations. These are plotted in an equal volume plot and are projected onto lower-hemisphere stereonets in figure 3.11. Between the three, now simplified, domains, we can see that there is no overlap between any of the 95% credible regions, allowing us to reject the null hypothesis that any two of the sets of orientation data were sampled from the same population of orientations.

For comparison with the orientation data and with other field areas that lack good paired foliation/lineation data, I also analyze the directional data from each fabric facies. In this case, I use the bootstrapping method to simulate sample datasets and generate 95% confidence ellipses for the mean foliation and lineation separately. These results are plotted in stereonets in figure 3.11c where they are also compared with the projected 95% credible regions. The confidence and credible regions are comparable although the confidence ellipses appear to reflect more of the anisotropy in the original samples.

Geologically, these statistical tests lend us more confidence in our observations of differences in fabric orientations between the fabric facies at Bligh Sound, and allow us to more confidently make interpretations about the underlying differences in process that produced such variation.

3.2.3 Mineral Compositions

Four thin sections from Bligh Sound samples were analyzed via EDS, which enabled me to determine the compositions of minerals within each of the structural domains at Bligh Sound. In particular, I analyzed pyroxene, hornblende, biotite, and plagioclase feldspar in order to look for variations in the major element compositions of these minerals. Variations in mineral composition between samples

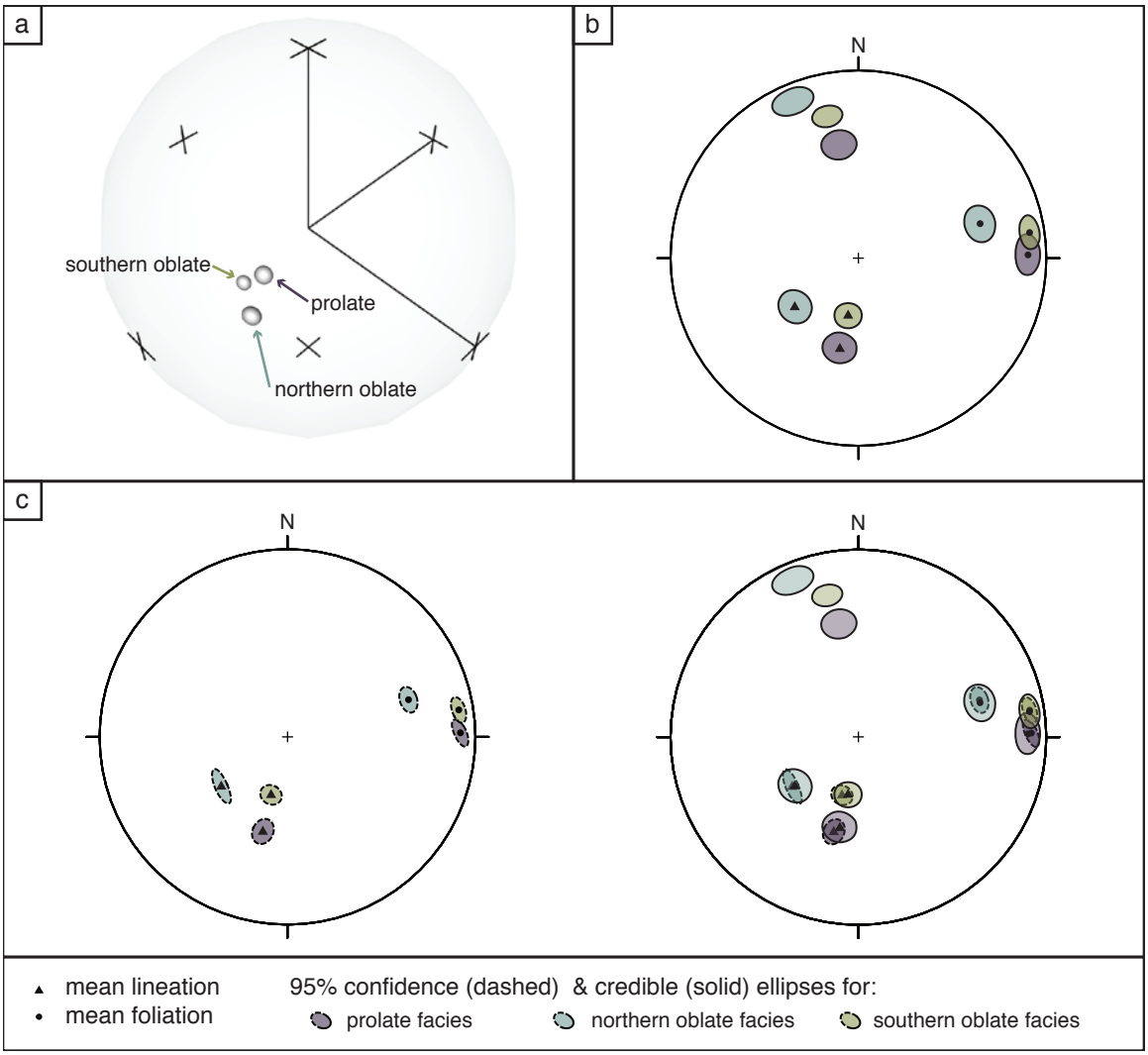

Figure 3.11: (a) Equal-volume plots of the 95% credible regions determined for orientations from each fabric facies at Bligh Sound from MCMC simulations. (b) 95% credible regions projected onto a hemispherical stereonet for comparison with mean foliation and lineation orientations. Although the projected credible regions for the prolate and southern oblate fabrics overlap, note that the 3D credible ellipsoids in (a) do not—this overlap is an result of projecting the credible ellipsoids onto a hemispherical plot. The paired foliation/lineation orientations from these facies are still statistically different. (c) 95% confidence ellipses from bootstrapping directional foliation and lineations data. Directional inference and orientational inference results are compared at right, showing good agreement between the two methods.

could indicate how metamorphic processes varied between structural domains. I present data from four samples samples—one located within the prolate domain, one from the northern oblate domain, and two located within the southern domain. Within the southern oblate domain, I analyzed one true oblate sample and one prolate sample from a pod of prolate material surrounded by oblate fabrics. Representative mineral compositions, in terms of major element oxide weight percentages (wt. %), from EDS are be presented in tables 3.2–3.6 with oxide weight percentages normalized to facilitate comparison. Total oxide weight percentages for non-hydrous minerals (pyroxene and feldspar) are normalized to 100%, while amphibole and biotite totals are normalized to 98% and 95%, respectively, because of the assumed amount of oxygen bound in OH groups in the mineral structure that is not easily detectable via the EDS method. All mineral compositions and raw spectral analyses are presented in appendix B.

Pyroxene

Both orthopyroxene and clinopyroxene are present in deformed samples of the Worsley Pluton at Bligh Sound. As discussed above, these both appear as primary igneous pyroxene in aggregate cores, and some clinopyroxene also exhibits evidence for syn-deformational metamorphic growth. Both types of pyroxene were analyzed and the compositions of igneous and metamorphic pyroxene were compared. Representative pyroxene analyses for each sample are presented in table 2.

Slight differences in the composition of pyroxenes from different structural domains are apparent in figure 3.12 and tables 3.2 and 3.3. Pyroxenes have comparable major element compositions between the two prolate samples (18BS42A and 18BS60A), and between the two oblate samples (18BS35A and 18BS64A). Between prolate and oblate samples, slight differences in clinopyroxene compositions

	Prolate				Northern Oblate		Southern Oblate	
Sample:	18BS42A		18BS60A		18BS35A		18BS64A	
Spectrum ID:	585	596	982	994	615	628	652	675
SiO_2 (wt. %)	51.67	52.15	52.21	52.52	50.92	51.04	51.27	50.80
Al_2O_3	4.13	3.28	2.85	2.87	3.63	3.40	2.46	2.77
TiO_2	0.00	0.00	0.00	0.00	0.00	0.00	0.00	0.00
FeO	21.63	21.44	22.08	21.77	25.41	25.15	26.06	27.40
MgO	21.65	22.21	21.37	21.80	18.77	18.76	18.77	17.79
MnO	0.64	0.60	0.57	0.66	0.60	0.54	0.71	0.83
CaO	0.28	0.33	0.67	0.38	0.45	0.87	0.50	0.42
K_2O	0.00	0.00	0.00	0.00	0.00	0.00	0.00	0.00
Na_2O	0.00	0.00	0.27	0.00	0.23	0.25	0.22	0.00
Total	100.00	100.00	100.00	100.00	100.00	100.00	100.00	100.00
Wo	0.01	0.01	0.01	0.01	0.01	0.02	0.01	0.01
En	0.63	0.64	0.62	0.63	0.56	0.55	0.55	0.52
Fs	0.36	0.36	0.37	0.36	0.43	0.43	0.44	0.47

Table 3.2: Representative orthopyroxene compositions

are apparent, but orthopyroxene compositions are more markedly different between the two structural domains (Fig. 3.12).

Orthopyroxene analyses in all samples exhibit enstatite compositions. More oblate samples (18BS35A and 18BS64A), however, are relatively enriched in iron (by ~3–6 wt. % FeO) compared to the prolate samples, which plot closer to the ferrosilite field in figure 3.12. Similarly, clinopyroxene in oblate samples is enriched in iron relative to the prolate samples, but not to the same degree as orthopyroxene (by only ~1–1.5 wt. %).

In all samples, clinopyroxene compositions resemble that of augite (Fig. 3.12; Table 3.3), specifically sodium-rich augite (cf. Deer et al. 1962). A significant variation in composition not shown on the pyroxene quadrilateral diagram is the Na_2O content of the clinopyroxenes, which is generally high (1.53–2.08 wt. %) for all the Bligh Sound samples. Where it appears both in aggregates and in

	Prolate				Northern Oblate		Southern Oblate	
Sample:	18BS42A		18BS60A		18BS35A		18BS64A	
Spectrum ID:	586	587	954	1005	621	643	656	666
SiO_2 (wt. %)	51.72	51.72	52.61	52.37	50.78	51.23	51.70	51.66
Al_2O_3	6.03	5.60	4.64	4.80	6.25	5.78	4.39	4.90
TiO_2	0.38	0.46	0.34	0.36	0.50	0.59	0.39	0.44
FeO	8.61	9.68	8.81	8.96	10.19	10.80	10.59	10.04
MgO	11.51	11.88	11.87	11.90	10.64	10.66	11.14	11.12
MnO	0.22	0.25	0.25	0.00	0.21	0.27	0.27	0.00
CaO	19.45	18.53	19.74	20.00	19.47	19.00	19.94	20.15
K_2O	0.00	0.00	0.00	0.00	0.00	0.00	0.00	0.00
Na_2O	2.08	1.89	1.73	1.61	1.97	1.68	1.58	1.69
Total	100.00	100.00	100.00	100.00	100.00	100.00	100.00	100.00
Wo	0.46	0.43	0.46	0.46	0.46	0.45	0.45	0.46
En	0.38	0.39	0.38	0.38	0.35	0.35	0.35	0.36
Fs	0.16	0.18	0.16	0.16	0.19	0.20	0.19	0.18

Table 3.3: Representative clinopyroxene compositions

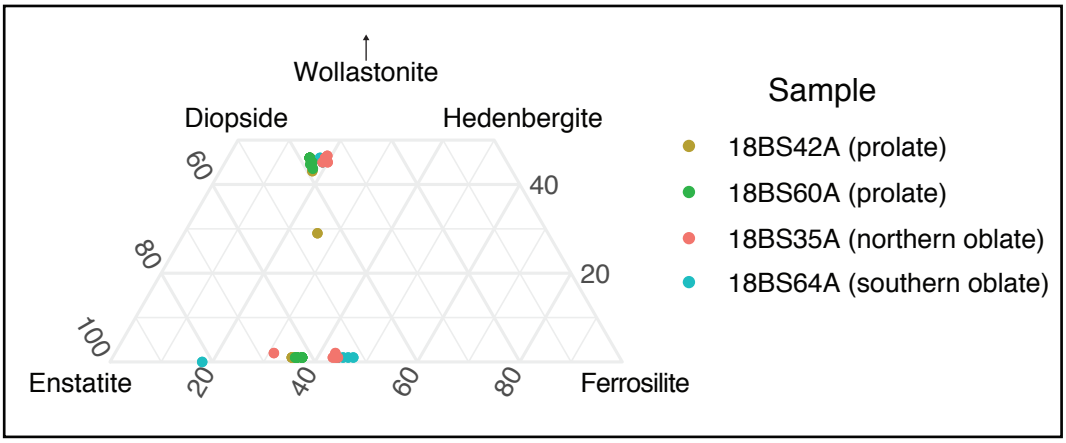

Figure 3.12: Pyroxene quadrilateral showing the compositional variations of pyroxenes between the various fabric facies of Bligh Sound. Pyroxenes from the oblate facies are generally enriched in Fe relative to those of the prolate fabrics.

	Prolate		Northern Oblate		Southern Oblate	
Sample:	18BS60A		18BS35A		18BS64A	
Spectrum ID:	946	984	627	638	674	684
SiO_2 (wt. %)	40.43	41.92	40.49	40.80	41.10	40.71
Al_2O_3	15.98	14.25	15.61	15.04	14.11	14.79
TiO_2	2.73	2.30	2.20	2.34	2.23	2.47
FeO	13.77	13.84	15.29	15.65	16.88	16.55
MgO	9.83	10.82	9.10	9.16	8.96	8.60
MnO	0.00	0.00	0.00	0.00	0.00	0.00
CaO	11.26	10.84	11.04	10.87	10.59	10.65
K_2O	2.37	2.11	2.68	2.47	2.09	2.13
Na_2O	1.62	1.93	1.58	1.67	2.04	2.10
Total	98.00	98.00	98.00	98.00	98.00	98.00

Table 3.4: Representative hornblende compositions

syn-kinematic tails or metamorphic rims, the Na2O content of metamorphic clinopyroxene is 0.12–0.29 wt. % greater than that of igneous clinopyroxene.

Amphibole

Amphiboles on pyroxene tails in the northern oblate domain fall primarily into the calcic-group, with some sodic-calcic amphiboles. No precise name may be assigned without knowledge of the valence state of iron, but the compositions of all analyzed amphiboles in the Worsley Pluton at Bligh Sound indicate that they may be classified as hornblendes.

The primary variation in hornblende compositions is in the amount of FeO and MgO present in hornblende. Iron (FeO) content is 1.5–3 wt. % greater in hornblende of the oblate domain than those of the prolate domain, with those of the southern oblate domain containing the greatest amount of FeO, and lowest content of MgO (Table 3.4). The relative enrichment in FeO of hornblendes in the oblate domains mirrors the pattern of increasing FeO content in pyroxenes of the oblate domain.

Biotite

Biotite is present in Worsley Pluton samples from the region of the southern oblate domain at Bligh Sound. EDS data are only available for samples 18BS64A and 18BS60A—the former is a true oblate sample while the latter comes from a pod of rocks with prolate fabrics within the southern oblate domain. Rocks from both the northern oblate domain and the prolate domain in the east of Bligh Sound contain little to no biotite. Where present, biotite primarily occurs in tails on pyroxene and hornblende. Rarely, biotite appears as isolated fragments within the plagioclase matrix.

The composition of biotite in the southern domain varies primarily in its Fe, Mg, and Ti content, as shown in table 3.5. The oblate sample (18BS64A) contains less TiO_2 (by 1–2 wt. %), significantly more FeO (by ~5 wt. %), and less MgO (by ~2 wt. %) than the sample from the prolate pod of the southern domain (18BS60A). The iron-enrichment of biotite in oblate samples relative to prolate samples again parallels trends of iron enrichment observed in pyroxene and amphibole compositions.

Feldspar

Plagioclase feldspar exhibits a similar composition across the George Sound shear zone at Bligh Sound and is unzoned. Plagioclase has consistently andesine-like compositions, occupying a narrow range of An_{31-35}, and there is no systematic variation in the composition of plagioclase between different domains (Table 3.6).

	Prolate		Southern Oblate	
Sample:	18BS60A		18BS64A	
Spectrum ID:	987	995	671	695
SiO_2 (wt. %)	37.21	37.47	36.85	36.94
Al_2O_3	14.91	14.85	14.61	14.77
TiO_2	6.34	5.56	4.59	4.27
FeO	13.67	12.96	18.00	18.08
MgO	13.19	14.52	11.43	11.61
MnO	0.00	0.00	0.00	0.00
CaO	0.00	0.00	0.00	0.00
K_2O	9.69	9.65	9.52	9.32
Na_2O	0.00	0.00	0.00	0.00
Total	95	95	95	95

Table 3.5: Representative biotite compositions

	Prolate				Northern Oblate		Southern Oblate	
Sample:	18BS42A		18BS60A		18BS35A		18BS64A	
Spectrum ID:	589	606	968	1008	623	641	680	687
SiO_2 (wt. %)	61.88	62.17	61.43	61.00	60.92	60.99	61.39	61.54
Al_2O_3	24.47	24.20	24.69	25.00	24.94	25.02	24.86	24.69
TiO_2	0.00	0.00	0.00	0.00	0.00	0.00	0.00	0.00
FeO	0.00	0.00	0.00	0.22	0.00	0.00	0.00	0.00
MgO	0.00	0.00	0.00	0.00	0.00	0.00	0.00	0.00
MnO	0.00	0.00	0.00	0.00	0.00	0.00	0.00	0.00
CaO	5.04	4.94	5.38	5.61	5.89	5.88	5.54	5.36
K_2O	0.34	0.15	0.29	0.00	0.38	0.27	0.00	0.00
Na_2O	8.28	8.54	8.20	8.17	7.87	7.83	8.21	8.42
Total	100	100	100	100	100	100	100	100
XCa	0.25	0.24	0.27	0.27	0.29	0.29	0.27	0.26
XK	0.02	0.01	0.01	0.00	0.02	0.02	0.00	0.00
XNa	0.73	0.75	0.72	0.73	0.69	0.70	0.73	0.74

Table 3.6: Representative plagioclase compositions

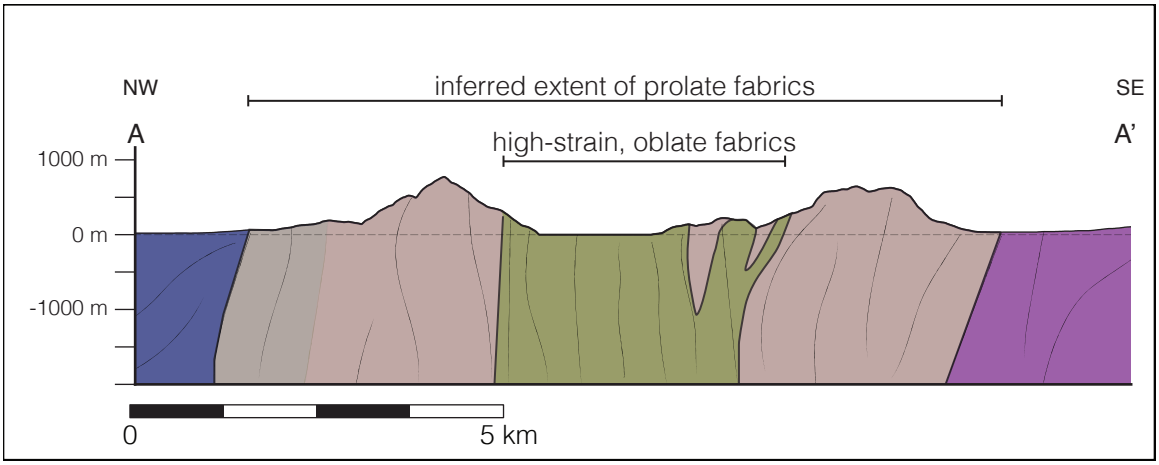

Figure 3.13: Cross section of southern section of the GSSZ at Bligh Sound. Figure 3.2 locates the profile A-A' and contains the legend for symbology. The cross section highlights the relationship between prolate and southern oblate fabrics, with pods of the former be preserved in the latter as strain localized. We extend the prolate domain from 3.2 to the west of the high-strain domain based on the orientation of fabrics reported in the Fiordland QMAP database.

3.2.4 Summary

Between each fabric facies, the significant differences in strain symmetry, microstructural character, the orientation of foliation and lineation, and some mineral compositions all indicate that each fabric facies represents the result of different deformation and metamorphic processes. The occurrence of these facies in three separate regions of Bligh Sound further indicates that the processes that formed the fabrics were spatially localized. The cross section in figure 3.13 summarizes our interpretations of the 3D structure of the GSSZ based on fabric orientations measured in the field.

Microstructural evidence, primarily in the form of feldspar textures provides some indication of the temperature conditions in which each fabric formed. Within the prolate and northern oblate fabrics, cuspate–lobate grain boundaries in plagioclase suggests deformation via grain boundary migration (GBM), which would indicate deformation at high temperatures (~600–1000°C; Rosenberg and Stünitz

2003). In the southern oblate fabrics, however, subgrain domains and grain boundaries with fine bulges suggest that plagioclase in the southern oblate facies deformed via a combination of subgrain rotation recrystallization and bulging recrystallization. These deformation mechanisms may indicate deformation at slightly lower temperatures than those in which the prolate and northern oblate fabrics formed, but other factors, such as the levels of fluid availability and strain rates may also account for the different microstructures. The details of temperature and other factors controlling plagioclase deformation are further discussed in chapter four as these textures are shared by fabrics at other field areas. The high temperatures suggested by plagioclase microstructures are further corroborated by the syn-kinematic growth of pyroxene and hornblende, which are indicative of upper-amphibolite metamorphism.

The northern and southern oblate facies appear to have experienced a greater degree of retrograde metamorphism than the prolate facies, which is relatively poor in hydrated minerals like hornblende and biotite. The apparent replacement of orthopyroxene by clinopyroxene (Fig 3.7), and growth of hornblende and ilmenite in tails on pyroxene aggregates suggests a metamorphic reaction involving the breakdown of orthopyroxene. Williams et al. (2014) document a metamorphic reaction occurring under dry conditions in a granite that cooled from high-pressure (1 GPa) granulite conditions (metamorphism at ca. 750°C) that may provide an model for the metamorphic reactions that produced the observed assemblages at Bligh Sound. In that case, the general reaction involved the reaction of calcic plagioclase and orthopyroxene to produce garnet, clinopyroxene, quartz, and sodic plagioclase. In the presence of water, however, Williams et al. (2000) indicate that hornblende may also be produced. It is conceivable that hornblende rather than garnet could crystallize with abundant water.

An alternative process for producing hornblende at amphibolite conditions described by Beach (1980) simply involves the reaction of clinopyroxene or orthopyroxene with plagioclase and water to yield hornblende. In the case of clinopyroxene reacting out, this reaction also yields quartz. Biotite then may result from further hydration of hornblende via another reaction described by Beach (1980), in which hornblende reacts with potassium and water to produce biotite, quartz, and excess iron or magnesium, calcium, sodium, and water. At Bligh Sound, the potassium may have been delivered via metasomatic fluids, which we know must have been present to produce the implied hydration reactions, or may be derived from the potassium feldspar that appears in minor quantities in the matrix and bordering pyroxene aggregates. Some combination of reactions similar to the three mentioned above likely acted in concert to produce the metamorphic clinopyroxene and the tails of both biotite and hornblende observed in the oblate fabrics of the Worsley Pluton.

There is evidence for increasing degrees of metamorphism and strain localization from prolate to northern oblate to southern oblate facies. The southern oblate fabrics exhibit the greatest degree of strain localization on the microscale, as well as the greatest abundance of hornblende and biotite of the three fabric facies. The syn-kinematic textures exhibited by the neocrystallized pyroxene, hornblende, and biotite indicate that metamorphism accompanied deformation. The linked increase in metamorphic minerals and strain localization suggests a possible feedback between metamorphic processes and deformation processes.

The inclusion of pods of prolate fabrics within rocks of the oblate facies similarly suggests the prolate facies may represent an early fabric that was overprinted by higher strain, oblate fabrics. The fact that these prolate pods contain more hornblende and biotite than rocks from the rest of the prolate facies may imply that

fluid flow through the oblate domain exposed these prolate pods to greater degrees of metamorphism.

Statistical tests on the fabric orientation data confirm that each facies features a unique fabric geometry. The variations in fabric orientation between each facies were used by Moyer (2019) to constrain the flow geometry of the GSSZ at Bligh Sound. Inferring a temporal relationship between the fabric facies—with prolate the earliest, crosscut by northern oblate and finally southern oblate fabrics—the steepening and anticlockwise rotation of lineations between the northern and southern oblate facies was interpreted as indicative of triclinic transpression in the GSSZ. The hypothesis tests on fabric orientations confirm that the strain geometry between the northern and southern oblate domains is statistically different, adding confidence to Moyer's interpretation.

3.3 George Sound

Roughly ten kilometers to the south of Bligh Sound, George Sound exposes a quite heterogeneous section of rocks. George Sound primarily dissects the eastern McKerr Intrusives—a dioritic pluton containing xenoliths of metasedimentary and granitic rocks—and the Expedition Pluton, a Carboniferous granite, crops out in the southernmost parts of the fjord. Near the mouth of George Sound, the fjord exposes a large section of the George Sound Paragneiss, which is a Paleozoic package of folded metasedimentary rocks that have been intruded by the McKerr Intrusives (Daczko et al. 2002). Deformation associated with the George Sound shear zone, however, is concentrated to the east of this unit, and I will focus on the structure and geology of the innermost sections of George Sound. This area represents a transition zone between the GSSZ in the Worsley Pluton to the north, and the

Misty Pluton to the south, and therefore provides an important link for correlating GSSZ fabrics along strike.

Unlike at Bligh Sound, where the GSSZ is a single, several-kilometer-wide zone, the GSSZ at George Sound appears in multiple meter- to kilometer-wide strands that are separated by rocks with low-strain and magmatic fabrics (Fig. 3.14). The definition of structural domains in this region is therefore less straightforward than at Bligh Sound as we must consider both differences in lithology and structural character. We also lack the quantitative finite strain data for rocks at George Sound that was used in defining structural domains at Bligh Sound. I therefore use a qualitative assessment of strain intensity based on field observations when discerning the different facies of fabrics that are present. A suite of lower-hemisphere stereonets in figure 3.15 breaks up the structural data based on the rock unit and apparent relative strain intensity as recorded in field notes.

3.3.1 Fabric facies

Fabric facies are here organized based on field observations of the apparent differences in strain magnitude. I classify fabrics from George Sound into three main groups: undeformed, low-strain, and high-strain. Undeformed plutonic rocks are coarse grained and exhibit magmatic textures and flow fabrics. The difference between low-strain and high-strain fabrics is relative and does not have the quantitative backing as fabric definitions at Bligh Sound. Low-strain fabrics include those that exhibit a foliation or lineation only, and typically lack shear sense indicators. High-strain fabrics exhibit a well-developed foliation and lineation, and are frequently mylonitic (i.e., showing evidence for grain-size reduction). In some cases, the isoclinal folding of foliation or dikes indicates high strain. Shear sense indicators in high-strain zones and more rarely in low-strains zones almost always

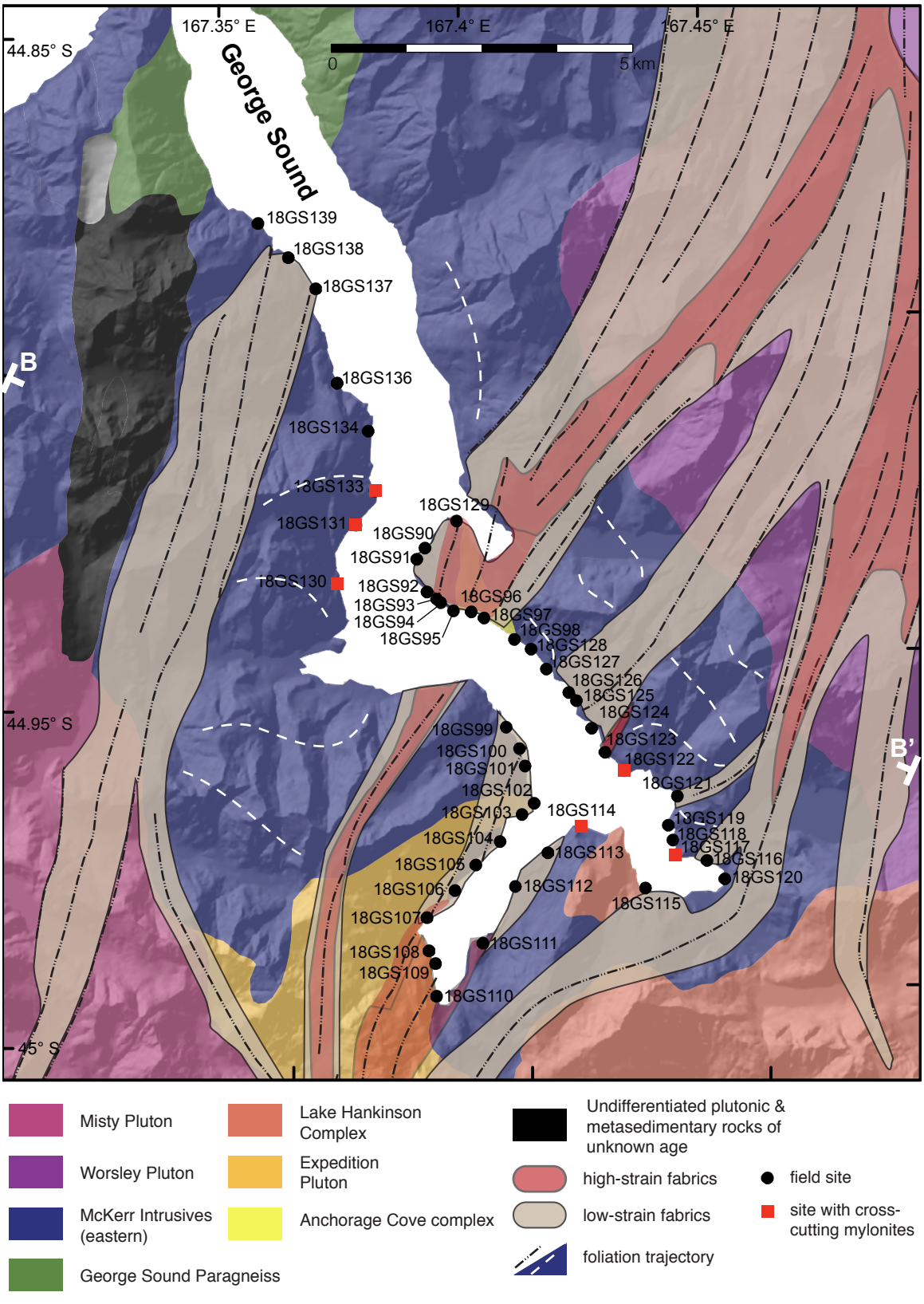
167.35° E
167.4° E
167.45° E
44.85° S
44.95° S
45° S
0
5 km
George Sound
B
B'
18GS139
18GS138
18GS137
18GS136
18GS134
18GS133
18GS131
18GS130
18GS129
18GS90
18GS91
18GS92
18GS93
18GS94
18GS95
18GS96
18GS97
18GS98
18GS128
18GS127
18GS126
18GS125
18GS124
18GS123
18GS122
18GS121
18GS119
18GS118
18GS117
18GS116
18GS120
18GS99
18GS100
18GS101
18GS102
18GS103
18GS104
18GS105
18GS106
18GS107
18GS108
18GS109
18GS110
18GS111
18GS112
18GS113
18GS114
18GS115
Misty Pluton
Worsley Pluton
McKerr Intrusives (eastern)
George Sound Paragneiss
Lake Hankinson Complex
Expedition Pluton
Anchorage Cove complex
Undifferentiated plutonic & metasedimentary rocks of unknown age
high-strain fabrics
low-strain fabrics
foliation trajectory
field site
site with cross-cutting mylonites

Figure 3.14: Detail geologic map of George Sound showing stations of the 2018 field season. Domains of high and low-strain fabrics are based on observations presented in this section and inferences to the north and south of George Sound are based on fabric measurements reported in the Fiordland QMAP database.

indicate a component of sinistral motion, consistent with the observed sense of shear on the George Sound shear zone elsewhere.

Undeformed McKerr Intrusives

At several locations, the eastern McKerr Intrusives appear unaffected by deformation in the George Sound shear zone. This is expressed in massive, unfoliated diorite, weak magmatic flow fabrics, and by preserved magmatic brecciation and magma-mixing textures between felsic and mafic material (Fig. 3.16). Where fabrics are observed, foliations are variably striking and steeply dipping (Fig. 3.15).

In thin section, the massive, unfoliated diorite of the McKerr Intrusives features subhedral grains of biotite and hornblende without a preferred orientation throughout a plagioclase-rich matrix. The igneous origin of this rock is recorded in relict plagioclase laths. Epidote minerals throughout the thin section contain inclusions of hornblende, biotite, and quartz—with quartz often present in symplectic lamellae (Fig. 3.16).

Low-strain McKerr Intrusives and Expedition Pluton

Low-strain fabrics include weakly foliated or lineated rocks of the McKerr Intrusives and Expedition Pluton. Examples of low-strain fabrics in the McKerr Intrusives include coarse gneissic foliations or fabrics defined by aligned mafic aggregates (Fig. 3.17). In the Expedition Pluton, low-strain fabrics are defined by penetrative

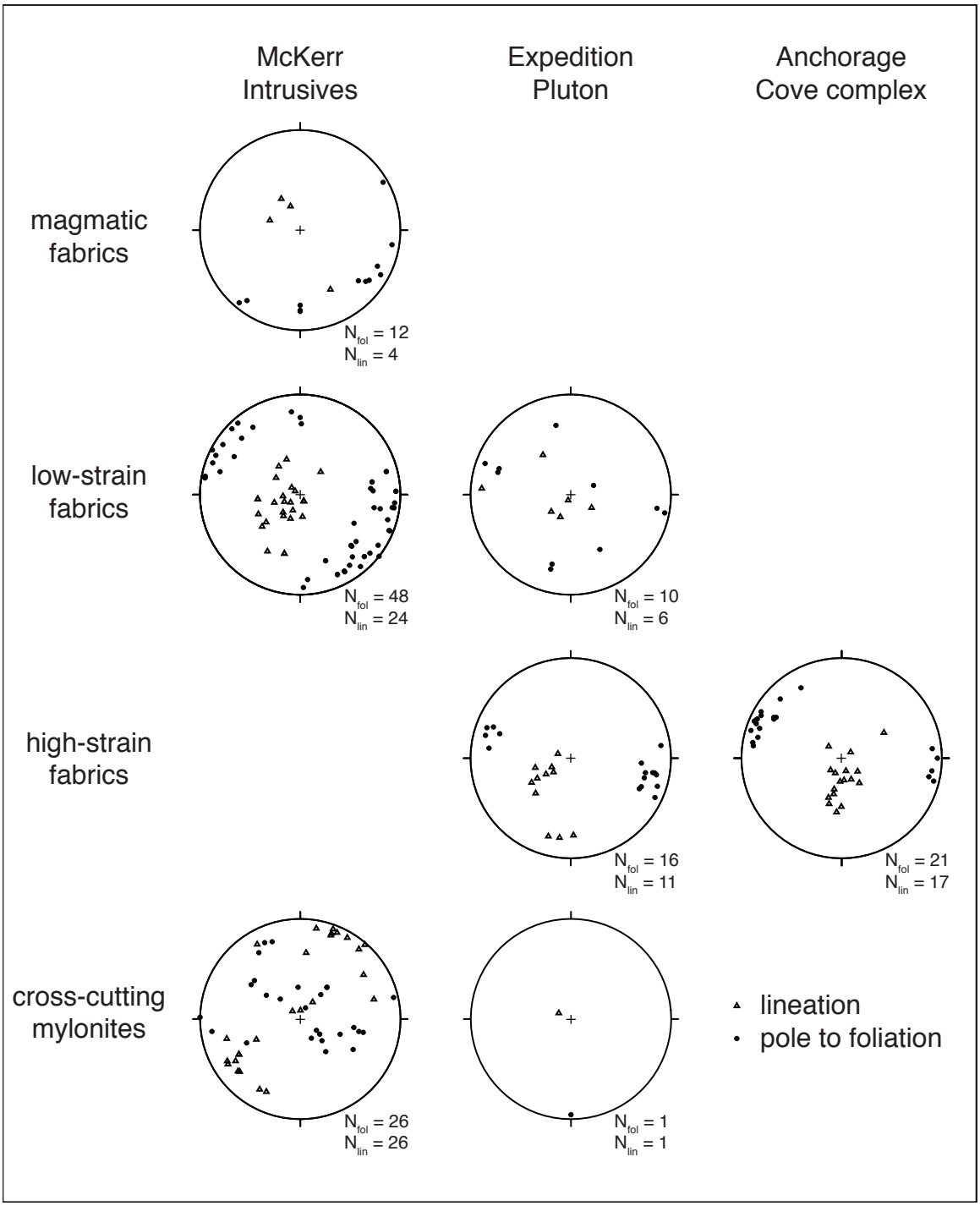

Figure 3.15: Equal-area stereonets of fabrics orientations at George Sound broken out by lithology and apparent strain intensity.

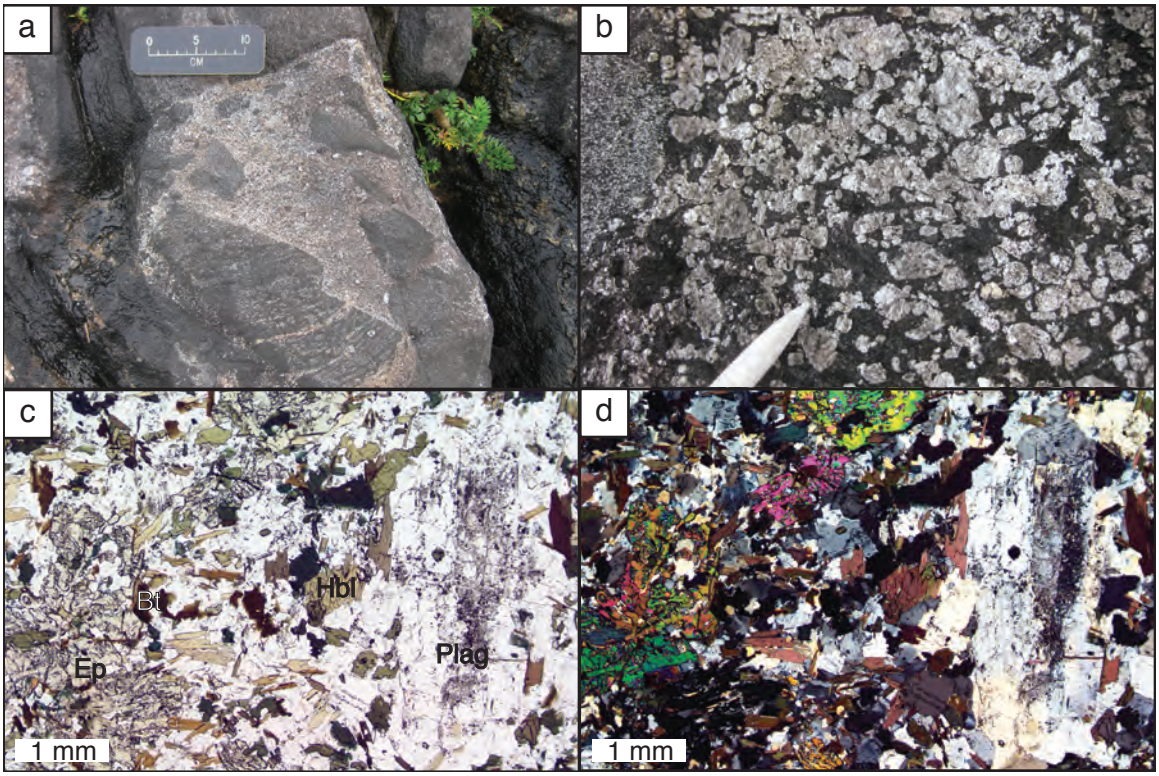

Figure 3.16: Field photos of magmatic textures at George Sound including (a) magmatic brecciation textures and (b) magma mixing textures at station 19GS127 where felsic and dioritic material of the McKerr Intrusives appears to have mixed. Photomicrographs of undeformed eastern McKerr Intrusives from sample 18GS120A showing the same field of view in (c) PPL and (d) XPL. The preservation of igneous textures indicated by the plagioclase lath at right suggests this rock experienced little deformation.

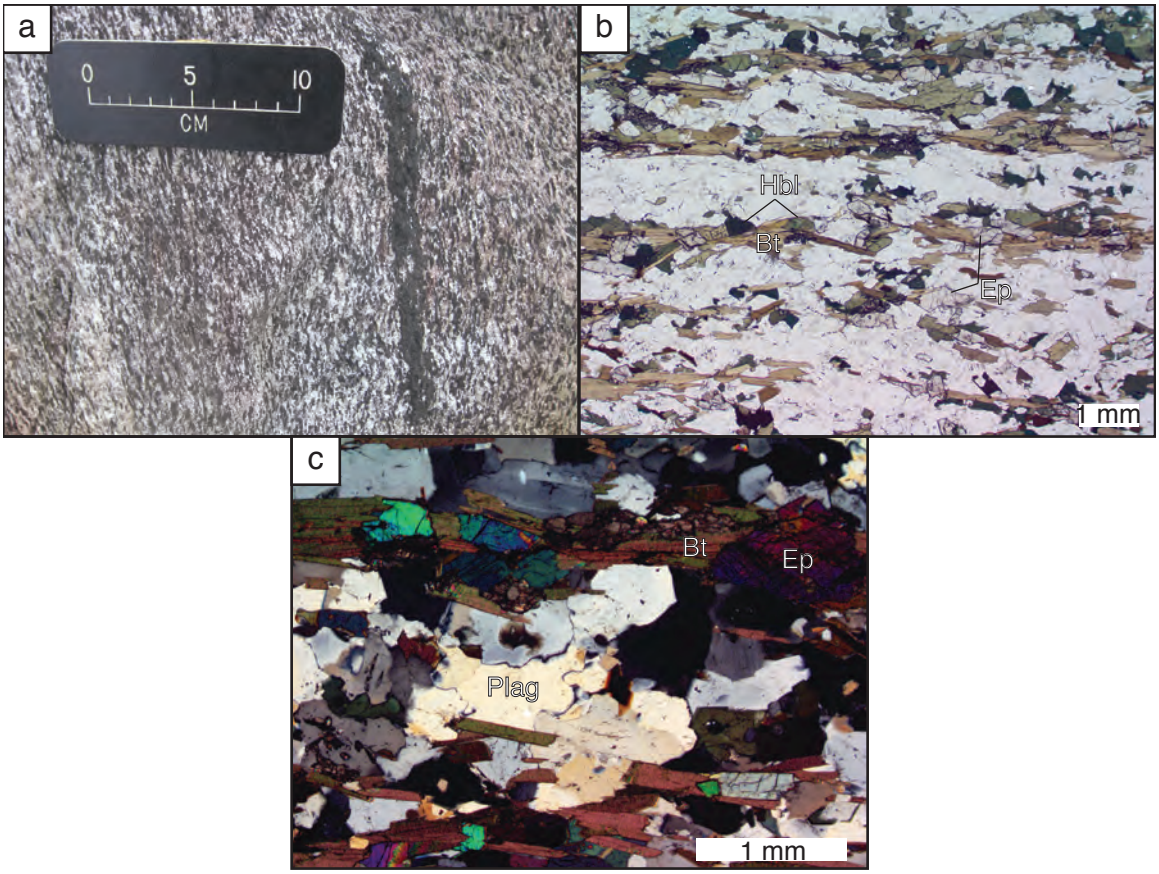

Figure 3.17: (a) Photo of low-strain fabrics in the McKerr Intrusives defined by mafic aggregates (station 18GS98). (b) and (c) are photomicrographs of sample 18GS97A, which has a smoother fabric than that in (a). Foliation in these is defined by biotite, hornblende, and epidote, with minor titanite. In (c), plagioclase feldspar exhibits cuspate-lobate grain boundaries and pinning by biotite.

foliation and/or lineation commonly defined by the alignment of biotite and sometimes hornblende. Essentially any non-mylonitic fabric in the Expedition pluton has been defined as low-strain. In this zone, rare asymmetric fabric elements like hornblende fish indicate sinistral, top-to-the-northwest motion.

Foliation in the McKerr Intrusives is steeply dipping and strikes vary widely from south to east. The lineation plunges moderately to steeply to the southwest and northwest (Fig. 3.15). In the Expedition Pluton, however, there is no clear pattern of fabric orientations, which are widely distributed (Fig. 3.15), which may in part

be a result of the low number of measurements from these fabrics. Variability in low-strain fabric orientations may in part be attributed to local folding of fabrics.

High-strain Expedition Pluton and the Anchorage Cove complex

Fabrics that appear to have accumulated more strain relative to those described in the previous section appear within the Expedition Pluton and in the Anchorage Cove complex. In the Expedition Pluton, high-strain fabrics include mylonitic zones < 1 meter-wide. In the lithologically heterogeneous Anchorage Cove complex, foliations in all lithologies and isoclinal folds of dikes and foliation indicate high strains. I use the term Anchorage Cove complex to describe the rocks present at Anchorage Cove—a relatively small (~1 km-wide), but lithologically complex section of George Sound. This is not an officially-defined lithostratigraphic unit and is simply meant to refer to the collection of rocks found at a structurally significant location. The Anchorage Cove complex includes sheets of amphibolite, metasedimentary rocks, granitic material, McKerr Intrusives diorite, and folded, cross-cutting pegmatitic dikes.

In all lithologies of the Anchorage Cove complex, asymmetric kinematic indicators suggest sinistral shear sense. In dioritic layers, this is indicated by the arrangement of mafic aggregates into fabrics oblique to the primary foliation (Fig. 3.18). Similar oblique fabrics are present in metasedimentary layers, defined by quartz and accompanied by asymmetric aggregates of mafic minerals and garnet (Fig. 3.18). In amphibolites, hornblende and biotite may define S-C fabrics. The direction of shear suggested by theses kinematic indicators is not always parallel to the mineral stretching lineation present at Anchorage Cove.

In thin section, metasedimentary units contain layers of fragmented garnet mixed with biotite, quartz, white mica, and feldspar. These layers alternate with

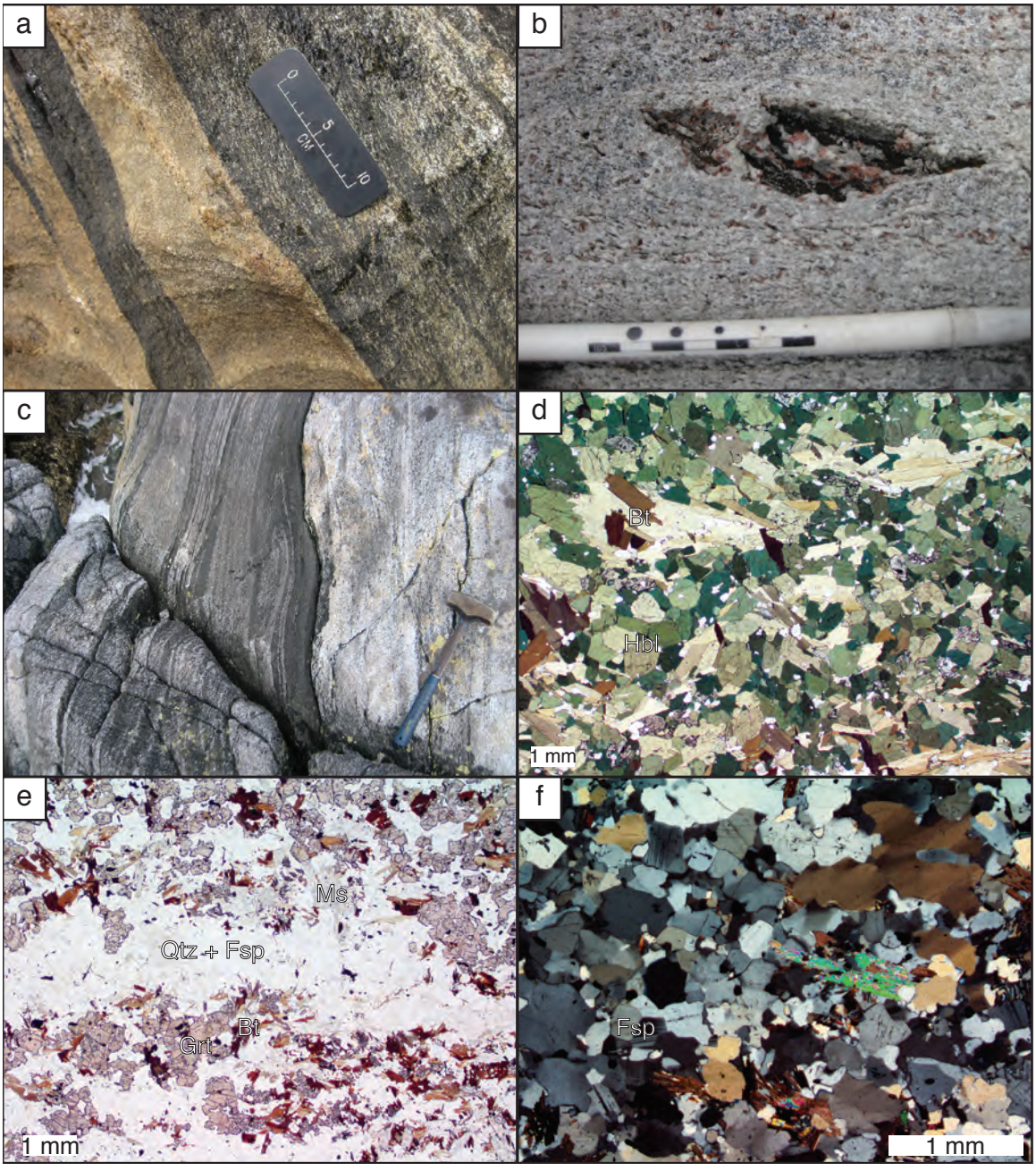
a
b
c
d
Bt
Hbl
1 mm
e
Ms
Qtz + Fsp
Bt
Grt
1 mm
f
Fsp
1 mm

Figure 3.18: Field photos and photomicrographs of the high-strain fabrics in the different lithologies of the Anchorage Cove complex (station 18GS129). (a) dark, dioritic material at right with fabric defined by mafic aggregates that are inclined to the compositional layering, suggesting sinistral shearing. (b) preferentially weathered sigmoidal aggregate of mafic minerals and garnet in a quartz-rich metamsedimentary layer, indicating sinistral motion. (c) shows isoclinal folds are developed in a section of interlayered dioritic and granitic material. (d) A photomicrograph from a sample of amphibolite (18GS129C) showing intact subhedral grains of biotite and hornblende that do not define a clear fabric at the micro scale (e) Photomicrograph in PPL of the metasedimentary rocks (18GS129A), showing the layering of mafics and garnet fragments with quartz and feldspar-rich domains, (f) in which amoeboid quartz grains contain elongate subgrain domains.

domains of only quartz and feldspar. These quartz and feldspar domains consist primarily of fine, interlobate grains, although some coarser quartz grains have amoeboid shapes and contain elongate subgrain domains (Fig. 3.18 e, f). In thin section, layers of amphibolite exhibit little evidence for grain-scale deformation and fabrics are defined by the alignment of subhedral grains of hornblende and biotite with quartz inclusions (Fig. 3.18 d).

Mylonitic zones in the Expedition Pluton occur in several locations within George Sound. In outcrop, these appear within locally homoegeneous sections of the Expedition Pluton, as well as in areas containing interlayered granitic and metasedimentary rocks. At the latter, isoclinal folding of compositional layering provides further indication of high strains, and sigmoidal feldspar porphyroclasts indicate sinistral shear sense consistent with other high strain GSSZ fabrics. In thin section, layers of quartz alternate with mixed potassium feldspar + plagioclase + quartz domains. White mica a biotite are often present in seams separating these domains (Fig. 3.19). Quartz layers contain irregular grains, often with subgrain domains.

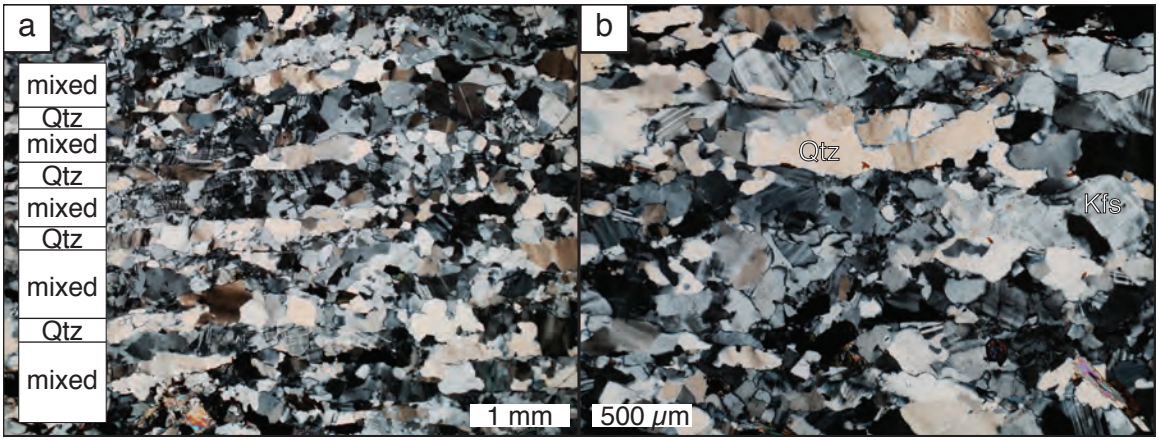

Figure 3.19: Photomicrographs of mylonitic fabrics in the Expedition Pluton. In (a), quartz-dominated domains alternate with domains of mixed feldspar and quartz. In (b), white mica can be seen defining boundaries between some of these layers. Quartz contains subgrain domains.

Cross-cutting mylonites

Distributed throughout George Sound are isolated, decimeter-wide mylonitic zones that crosscut other fabrics and dikes (Fig. 3.20). Almost all of these occur within the McKerr Intrusives, with one exception in the Expedition Pluton (Fig. 3.20 b). These mylonitic zones are typically moderately- to shallowly-dipping to the northwest and southeast—in contrast with the steep fabrics of other facies (Fig. 3.15). Several subvertical mylonites have also been recorded. Lineation directions in these mylonites are primarily shallowly-plunging to the northeast and southwest, but there are also moderately- and steeply-plunging lineations, defining a weak vertical girdle from NE–SW.

There are also patterns in the spatial distribution of these mylonites and their orientations. All measurements come from stations at the southeast end of George Sound, or from the area northwest of Anchorage Cove. Most mylonites at the southern end dip towards the southeast, and those to the north dip towards the northwest. The strikes of both of these sets of mylonitic foliation roughly parallel

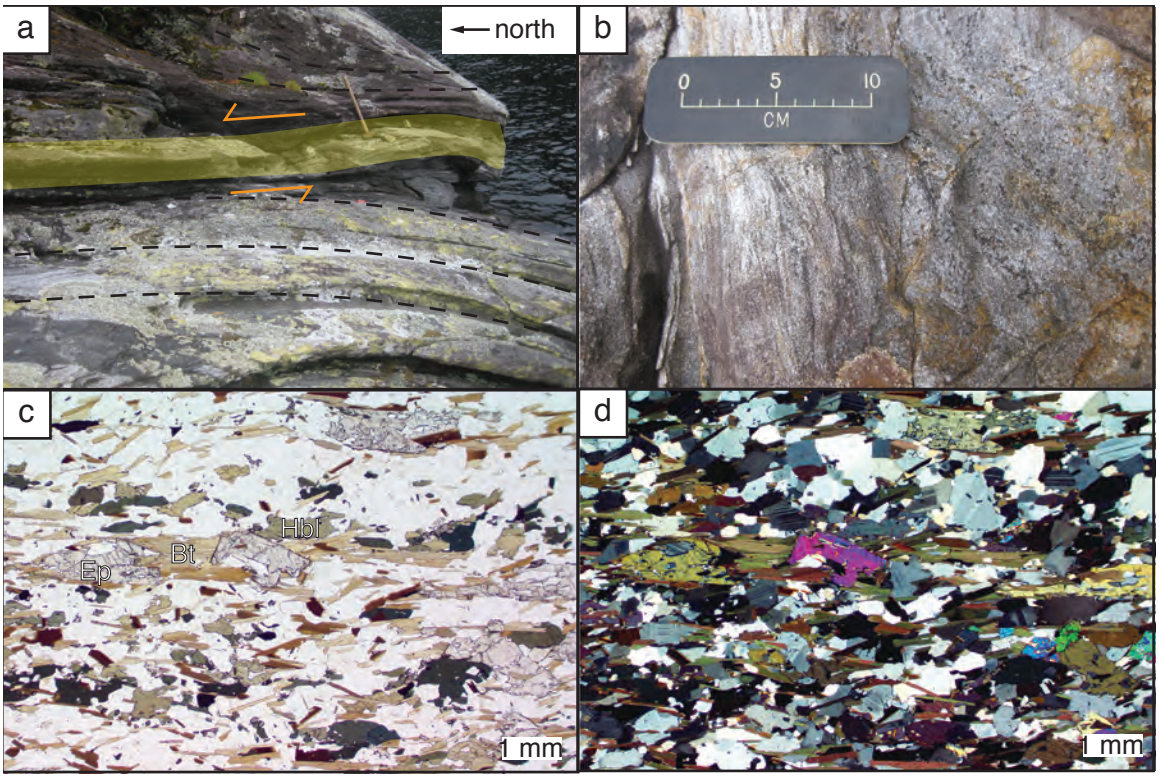

Figure 3.20: Field photos of low-angle cross cutting mylonitic zones at (a) stations 18GS117 and (b) 18GS125. In (a), deflected foliation in the dioritic McKerr Intrusives into a mylonitic zone indicates a top to the north sense of motion. (b) shows evidence for grain-size reduction between granitic host-rock and mylonites. (c) and (d) show photomicrographs in PPL and XPL, respectively, of a thin section from 18GS117. In (c), the foliation is defined by biotite, epidote, and hornblende with minor titanite. In (d), plagioclase exhibits cuspate-lobate grain boundaries and evidence for pinning on biotite.

those of the low- and high-strain GSSZ fabrics, but are shallower. Most mylonites from the southern part of George Sound exhibit sinistral offset, with a dip-slip component consistently indicating top-to-the-north motion. The northwest-dipping mylonites exhibit dextral, top-to-the-north shear sense.

Only one thin section allows us to examine the microstructural properties of the cross-cutting mylonites. The mylonitic zone present at 18GS117 cuts the McKerr Intrusives, which are dioritic at that location. A fabric defined by the alignment of subhedral biotite, epidote, and hornblende defines the foliation in the mylonite (Fig. 3.20 c). Fine-grained plagioclase exhibits cuspate lobate grain boundaries and in places appears pinned on biotite grains (Fig. 3.20d). These plagioclase textures are suggestive of deformation at high-temperatures.

3.3.2 Statistical analysis

For statistical analysis, foliation and lineation data from the fabric facies defined above are further divided based on the rock type in which the fabric appears (Fig. 3.15). Only three of these subsets of data are readily described and compared using the directional and orientational statistical tools—low-strain fabrics from the McKerr Intrusives, and high-strain fabrics from the Expedition Pluton and Anchorage Cove complex. Equal volume plots of paired foliation/lineation orientations from each of these fabric facies are presented in figure 3.21, which shows that orientations within each facies are clustered and therefore may be appropriately described by mean and variance. For the purposes of analyses, I remove the measurements from station 18GS107 from the high-strain Expedition Pluton sample as the data from the mylonite at this station appear as clear outliers (with lineations plunging shallowly to the south). It will be more appropriate to compare these outliers then to the dominantly WNW-dipping foliations and steeply

SW-plunging foliations of other mylonitic fabrics in the Expedition pluton. Other subsets of fabric orientation data either have too few data, or orientations do not follow a clustered, unimodal distribution. The bulk of fabric measurements fall into the former three groups, however, so the statistical analyses remain useful for understanding the geometry of the GSSZ.

Similar to the approach taken with data from Bligh Sound, I plot data, determine descriptive statistics, and perform statistical inference to yield confidence/credible regions for the mean fabric orientations, allowing me to compare the data from the different fabrics. The number of measurements of foliation and lineation directions for the high-strain facies is low, and the paired foliation/lineation measurements comprise and even smaller subset of these. Because of this, for each of the three groups of data that I analyze, I check the results of the orientational analyses by also determining directional statistics for unpaired foliation and lineation data. This allows me to check for biases in the orientational data and ensures that the orientational analyses do not mis-represent geological reality because of a lack of coverage of paired foliation/lineation data. The descriptive statistics—mean direction/orientation and variance—for the fabric facies that were analyzed are presented in table 3.7 for measurements treated as orientation data, and table 3.8 for the directional treatment.

The primary question I aim to address with these statistical analyses is whether or not different rock types record different fabric orientations. Qualitatively, the difference between the geometries of the main George Sound shear zone fabrics—the low-strain fabrics from the McKerr Intrusives, and high-strain fabrics from the Expedition Pluton and Anchorage Cove complex—appears small. Statistical inference, however, allows us to compare the means of our samples of fabric orientations and their uncertainties.

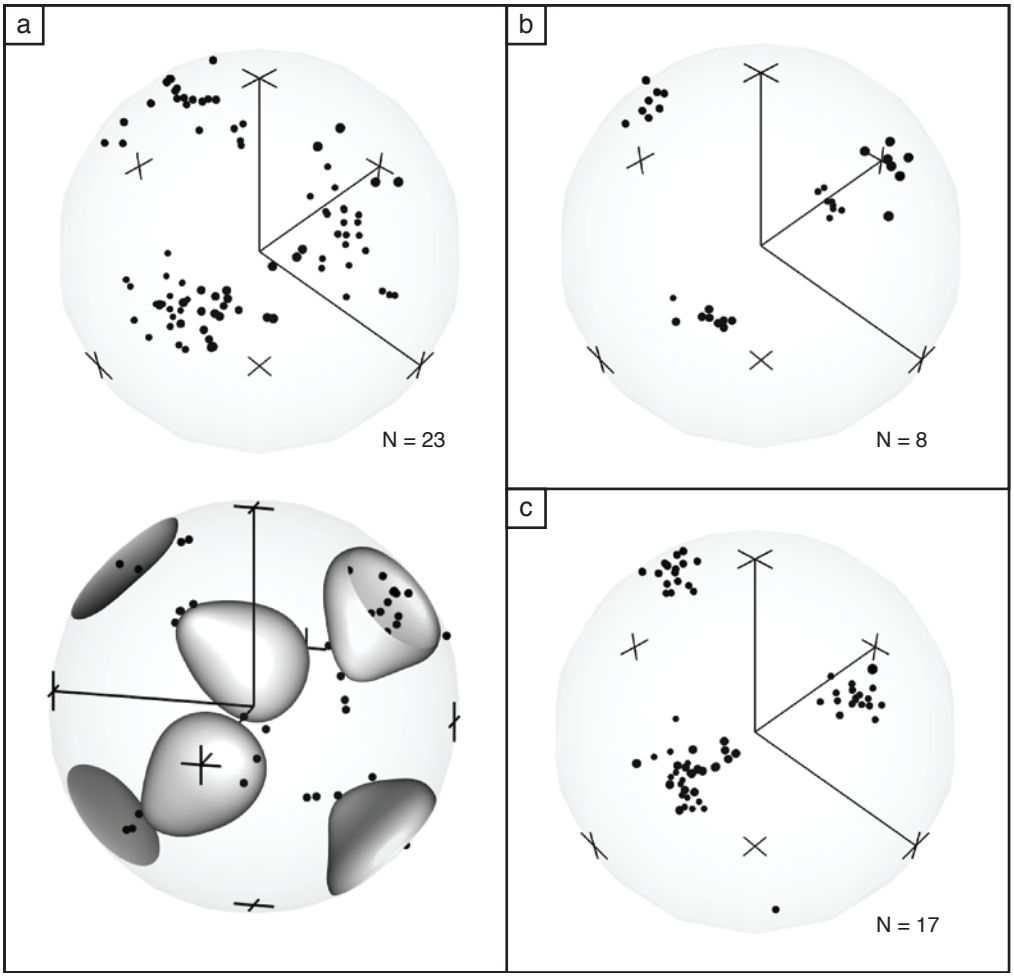

Figure 3.21: Equal volume plots of paired foliation/lineation orientations for (a) low-strain fabrics in the McKerr Intrusives, with a rotated view of the same data contoured with 10-sigma Kamb contour surfaces to emphasize the clustering that is not clear in the plot at top, (b) high-strain fabrics in the Expedition Pluton, and (c), high-strain fabrics at Anchorage Cove. Fabric orientations for each define unimodal clusters.

Fabric Facies	N_{pairs}	Fréchet Mean		Fréchet Variance	$\hat{\mathbf{K}}$ eigenvalues
		Strike/Dip	Trend/Plunge		from matrix Fisher MLE
McKerr, low strain	24	214/84	235/74	0.22	11.8, 4.2, 1.3×10^{-7}
Expedition, high strain	8	191/70	240/64	0.03	69.0, 28.5, 3.4×10^{-6}
Anchorage Cove complex	17	022/81	172/73	0.08	34.6, 10.4, 3.8×10^{-7}

Table 3.7: Statistical descriptors of fabric measurements from George Sound treated as orientation data .

Fabric Facies	N_{fol}, N_{lin}	Fréchet Mean	
		Strike/Dip	Trend/Plunge
McKerr, low strain	48, 24	215/83	238/75
Expedition, high strain	13, 8	194/76	240/64
Anchorage Cove complex	21,17	021/83	175/73

Table 3.8: Statistical descriptors of fabric measurements from George Sound treated as directional data.

Following the same process as in the preceding section, I use orientation statistics on the paired foliation/lineation data to determine 95% credible regions for the means. Following the results of a matrix Fisher MLE ($\hat{\mathbf{K}}$ eigenvalues reported in table 4), I perform MCMC simulations on the orientation data for the three fabric facies. The resulting 95% credible regions are displayed in equal volume plots (Fig. 3.22 a), and projected onto lower-hemispherical stereonets (Fig. 3.22 b). Only the credible regions for the low-strain fabrics from the McKerr Intrusives and the and high-strain Anchorage Cove complex fabrics appear to overlap. Thus, the orientations of fabrics from these two facies are not significantly different and we do not reject the null hypothesis that they are drawn from populations with the same means. The orientation of high-strain fabrics in the Expedition Pluton, however, do differ significantly from fabrics in the Anchorage Cove complex and bulk McKerr Intrusives.

Just as I did with determining descriptive statistics, I have also applied directional statistical inference and the bootstrapping method to the foliation and lineation data only to compare to the orientation analyses. This will also allow me to compare these fabrics with those from other field areas that must be described by directional methods and bootstrapped confidence intervals. The 95% confidence ellipses are presented in a stereonet (Fig. 3.22 c). These corroborate the results of the orientation statistics and the similarities between the low-strain McKerr Intrusives fabrics and the high-strain Expedition Pluton fabrics.

3.3.3 Summary

The distribution of high-strain fabrics at George Sound prompts us to map four main shear zone branches that are separated by zones of magmatic or very weakly deformed rocks (Fig. 3.14). These branches are localized around granitic and

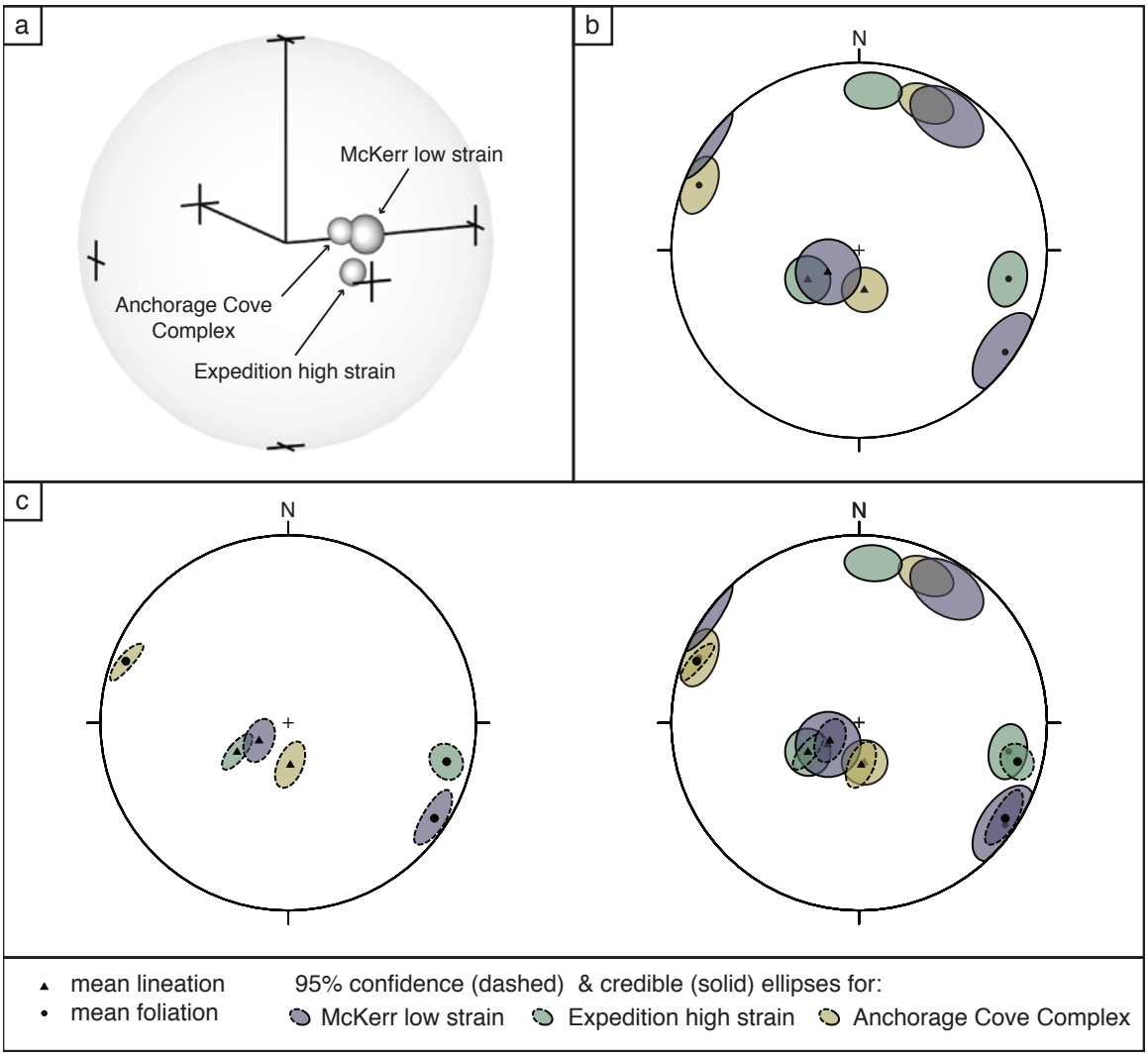

Figure 3.22: (a) Equal-volume plots of the 95% credible regions determined for orientations from the three fabric facies with good orientation data at George Sound from MCMC simulations. (b) 95% credible regions projected onto a hemispherical stereonet for comparison with mean foliation and lineation orientations. (c) 95% confidence ellipses from bootstrapping directional foliation and lineations data. Directional inference and orientational inference results are compared at right, showing good agreement between the two methods.

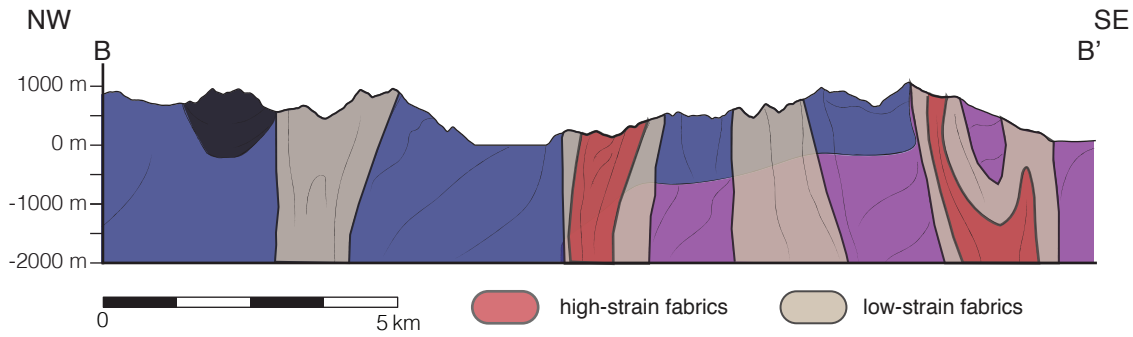

Figure 3.23: Schematic cross-section across the GSSZ at George Sound. Key for geologic units is same as figure 3.14.

metasedimentary xenoliths within the eastern McKerr Intrusives, within the adjacent Expedition Pluton, and near contacts with adjacent rock units. High strain fabrics appear localized in weaker lithologies—metasedimentary and granitic units—and in heterogeneous sections like the Anchorage Cove complex, while lower-strain fabrics appear in the surrounding dioritic McKerr Intrusives. Locally, predominately low-angle mylonites crosscut the NE–SW-striking foliations of low-strain fabrics, and it is difficult to place them confidently within the GSSZ. Geometrically, these mylonites are quite different than the low- and high-strain GSSZ fabrics at George Sound, with shallowly NE- or SW-plunging lineations. The kinematics of these mylonites is variable as well, with some exhibiting sinistral shear and some dextral shear. High-temperature plagioclase microstructures observed in one of these mylonites, however, suggests that it formed at similar temperature conditions as the other GSSZ fabrics. Their crosscutting nature implies that these mylonites postdate at least some of the low-strain fabrics at George Sound, but their relationship to the GSSZ system as a whole remains ambiguous. The 3D geometry of the GSSZ, excluding cross-cutting mylonites, at George Sound is presented in a cross section in figure 3.23.

Microstructures in deformed rocks from George Sound indicate deformation at

intermediate to high temperatures. Again, more detailed discussion of temperature interpretation is reserved for chapter four because of several microstructures are common to each field area. The feldspar microstructures of low strain fabrics in the eastern McKerr Intrusives—cuspate–lobate grain boundaries and pinning by biotite—suggest deformation via grain boundary migration (GBM), which is indicative of deformation at high temperatures. Metasedimentary rocks from the Anchorage Cove complex contain amoeboid quartz grains with elongate internal subgrain domains, suggesting deformation of quartz via a combination of GBM and subgrain rotation recrystallization, similarly suggesting high temperature deformation. Mylonites in the Expedition Pluton, contain polymineralic quartz ribbons which are also indicative of high temperatures. Subgrains within these ribbons may indicate continued deformation at cooler temperatures. The feldspar GBM and pinning microstructures in the crosscutting mylonite from station 18GS117 indicate deformation at conditions similar to those in the Anchorage Cove complex and McKerr Intrusives, so these fabrics must have formed while this section of the crust was still relatively hot.

Mineral assemblages in rocks at George Sound indicate metamorphism at amphibolite facies conditions. Both garnet in metasedimentary units and the assemblage of hornblende, biotite, epidote, and plagioclase in dioritic eastern McKerr Intrusives are consistent with amphibolites facies conditions. The temperatures of deformation indicated by quartz and plagioclase microstructures are also consistent with deformation near amphibolite-grade conditions. However, there is no obvious evidence for the syn-kinematic growth of metamorphic minerals.

Thin sections from samples at Anchorage Cove (station 18GS129), which features significant lithologic heterogeneity, show some evidence that rheologically weaker rocks like metasediments accumulated greater strains than stronger rocks

like amphibolites (compare Fig. 3.18d and e). The former exhibit well-defined folia and evidence for quartz and feldspar recrystallization, while the latter is dominated by subhedral biotite and hornblende without clear preferred orientations. At the outcrop scale, therefore, strain appears localized into weaker lithologies. This pattern is mirrored on the scale of George Sound, where areas containing weak rocks or heterogeneous assemblages—like Anchorage Cove and the branch of George Sound dominated by the granitic Expedition Pluton—also exhibit the highest-strain fabrics. The eastern McKerr Intrusives primarily appear deformed in zones adjacent to these weaker areas, and more magmatic fabrics are found separating these high-strain branches. To the southeast of Anchorage Cove, field observations note that fabrics in the McKerr intrusive become increasingly well-defined with proximity to the high-strain zone centered on Anchorage Cove.

Geometrically, the fabrics at George Sound that we interpret as part of the GSSZ feature fairly comparable steeply S–SW-plunging lineations and subvertical NE–SW-striking foliations. The orientation of mylonitic fabrics preserved in the Expedition Pluton, however, is demonstrated—via statistical hypothesis testing—to be significantly different from the fabrics in the Anchorage Cove complex and McKerr Intrusives. The Expedition Pluton mylonites contain a more NNE-striking foliation. This, however, may simply be the result of the bending of the GSSZ to connect with more N–S-striking fabrics to the south of George Sound. The Expedition Pluton is situated to the SW of most stations where high-strain fabric measurements were collected, so this difference may simply reflect the along-strike variations in the geometry of the GSSZ.

3.4 Mary Peaks

Less than five kilometers to the south of the southern end of George Sound lies the eastern margin of the Misty Pluton, which then extends farther south for another fifty kilometers to Doubtful Sound. The George Sound shear zone follows the boundary of the Misty Pluton for at least the northern forty kilometers (Fig. 3.24). The Misty Pluton—a two-pyroxene to hornblende diorite similar to the Worsley Pluton—is the main host of deformed GSSZ fabrics, although the GSSZ does crosscut an adjacent unit and a screen of granitic material within the Misty Pluton. The primary lithologic units to the west of the Misty Pluton that I will discuss in this section are the Large Granite and Cozette Pluton, which are Carboniferous granites comparable to the Expedition Pluton to the north. These share intrusive contacts with the Misty Pluton that in many places were exploited by the George Sound shear zone during the Cretaceous, and during the Miocene by steeply-dipping oblique-slip thrust faults.

The George Sound shear zone is expressed in a similar manner along most of the length of the Misty Pluton margin. This section is divided into three subsections, each concerned with a different field area, providing four different transects across the GSSZ in this region. The first field area, Mary Peaks, contains the most atypical expression of the GSSZ for the Misty Pluton margin, but the subsequent field areas—Myth Tarn, and the Southern Misty Margin—all contain correlative GSSZ fabrics. Each subsection includes a description of the fabric facies present, statistical analyses of fabric orientations, and presentation of geochemical data if applicable. This section concludes with a summary of the entire Misty Pluton margin and correlation between the difference field areas.

In the Mary Peaks field area (Fig. 3.25), we conducted a transect along a ridge

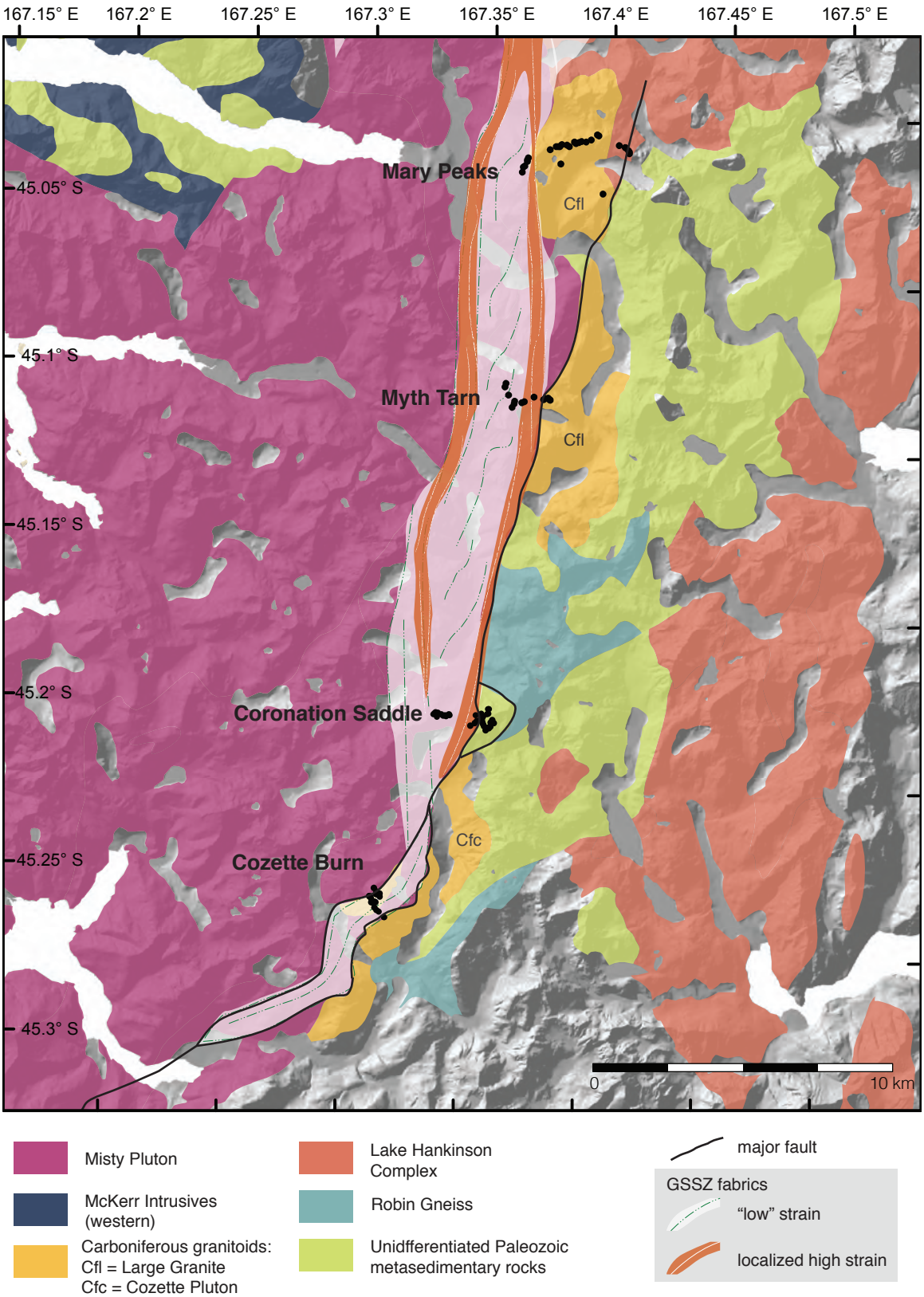
167.15° E
167.2° E
167.25° E
167.3° E
167.35° E
167.4° E
167.45° E
167.5° E
45.05° S
45.1° S
45.15° S
45.2° S
45.25° S
45.3° S
Mary Peaks
Myth Tarn
Coronation Saddle
Cozette Burn
Cfl
Cfl
Cfc
0
10 km
Misty Pluton
McKerr Intrusives (western)
Carboniferous granitoids:
Cfl = Large Granite
Cfc = Cozette Pluton
Lake Hankinson Complex
Robin Gneiss
Unidfferentiated Paleozoic metasedimentary rocks
major fault
GSSZ fabrics
"low" strain
localized high strain

Figure 3.24: Map of the entire eastern margin of the Misty Pluton and the three field areas discussed in this section: Mary Peak, Myth Tarn, and the Southern Misty Margin (comprising the Coronation Saddle and Cozette Burn transects. The GSSZ follows this boundary for most of the length of the Misty Pluton and related deformation fabrics are sometimes found in host rocks to the east.

top that exposes the eastern margin of the Misty Pluton, and a sheared contact with the Large Granite to the east. Farther east, the Large Granite is in contact with the Lake Hankinson Complex, both of which are cross-cut by N–S-striking faults. We collected few data from the eastern end of Mary Peaks and numerous faults complicate the contact between Large Granite and Lake Hankinson Complex. It is therefore unclear what the relationship of fabrics in the Lake Hankinson Complex is to deformation in the George Sound shear zone at Mary Peaks and I will not consider these sparse data in this section.

At Mary Peaks, I define three fabric facies. (1) the Misty Pluton at this location is heterogeneous and at some stations exhibits complex magmatic, metamorphic, and deformation textures. (2) Near the contact between the Misty Pluton and the Large Granite, samples of float indicate deformation of the Misty Pluton, and a 1 meter-wide mylonitic zone in the Large Granite defines the boundary between these units. (3) Farther east, the Large Granite primarily comprises L > S tectonites with shallowly southwest-plunging lineations and steep NE–SW-striking foliations. The orientations of these fabrics are presented in figure 3.26 a.

3.4.1 Fabric facies

Misty Pluton – magmatic and deformed fabrics

The western portion of the Mary Peaks transect crosses variably deformed rocks of the Misty Pluton. The abundance of quartz and potassium feldspar in what was

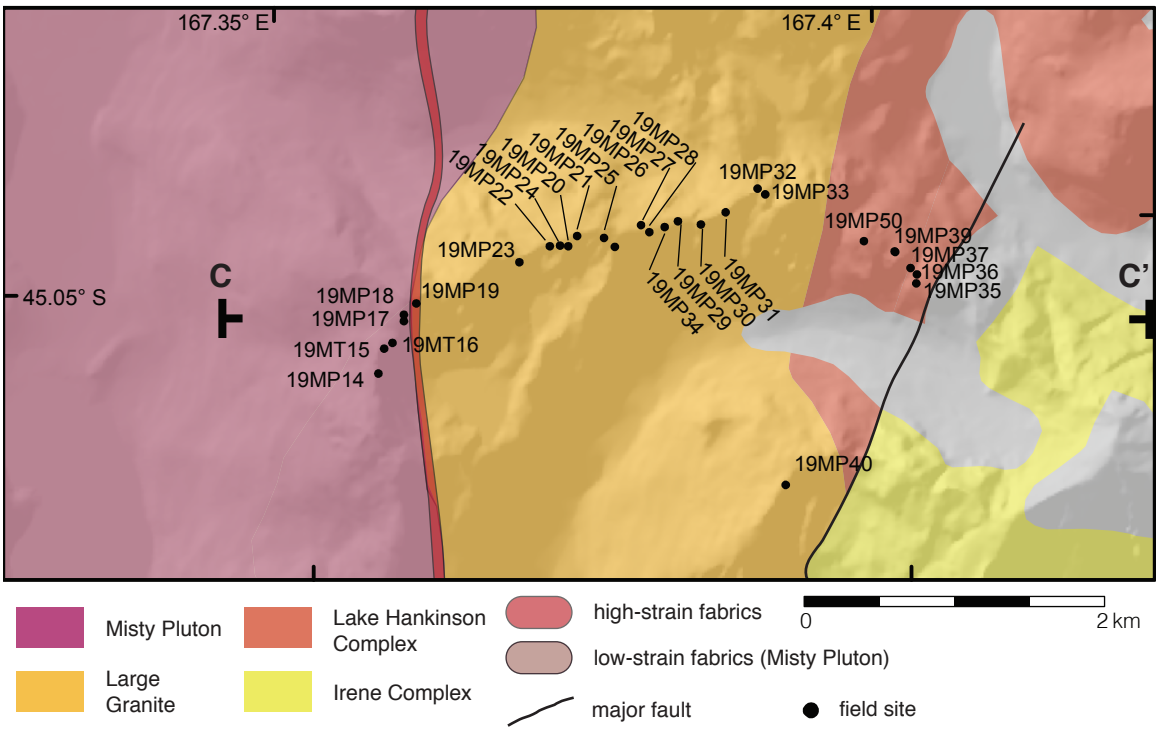

Figure 3.25: Detail geologic map of the Mary Peaks field area showing the extent of GSSZ fabrics identified, which are confined to the Misty Pluton and the western boundary of the Large Granite.

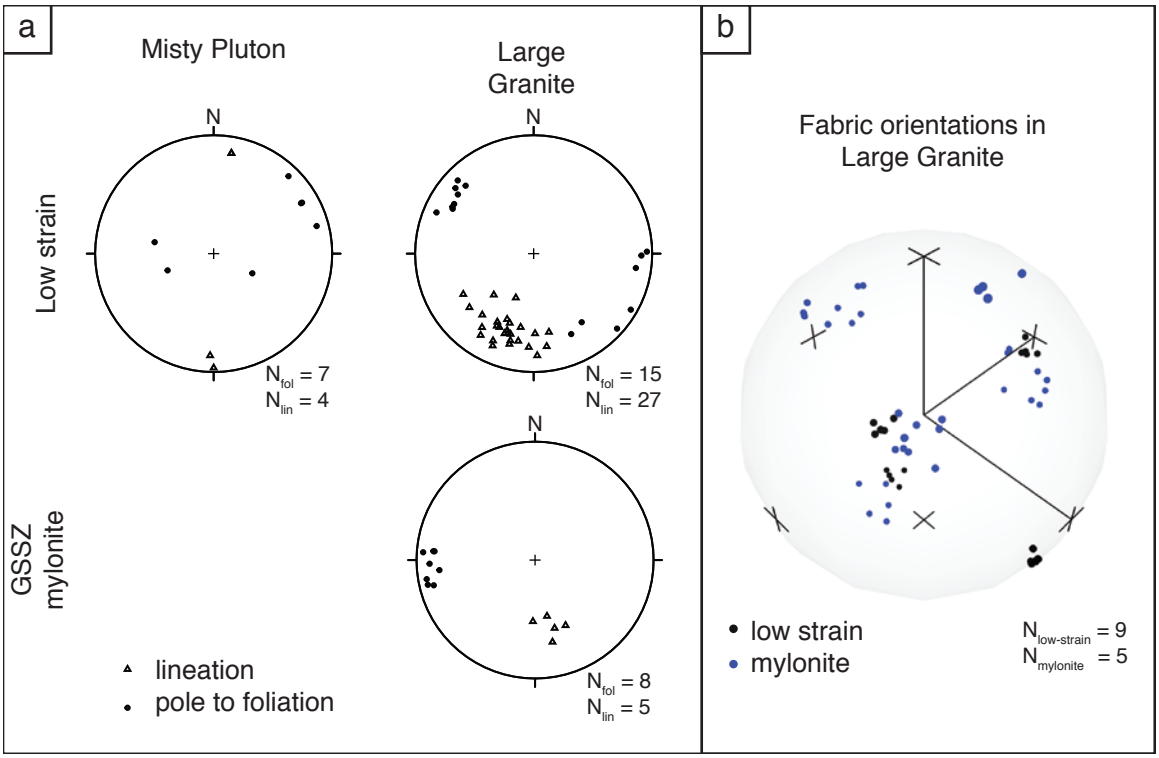

Figure 3.26: (a) Lower-hemisphere stereonets of foliation and lineation directions from the different fabric facies at Mary Peaks. (b) Equal volume plot of paired foliation/lineation data from the low-strain (black) and mylonitic (blue) fabrics in the Large Granite, showing that each of these defines unimodal clusters.

originally considered to be the dioritic Misty Pluton suggests a more complicated petrogenesis than the rest of the Misty Pluton, and complex magmatic, metamorphic, and deformation textures are apparent at the micro scale. These textures suggests the assimilation of parts of the adjacent Large Granite and incorporation of melted granitic material into the Misty Pluton in this region. There is a weak L>S fabric in these rocks defined by the alignment of aggregates of biotite and minor epidote (Fig. 3.27 a). The subhorizontal lineations trend N-S and foliation directions are variable (Fig. 3.26).

There is no outcrop of Misty Pluton near the inferred boundary with the Large Granite to the east, but samples of float on an adjacent peak indicate that it must be present immediately to the west of the mylonitic zone in the Large Granite (discussed below). These samples of Misty Pluton near the mylonite are similar in mineral composition to in situ rocks to the west, but exhibit a stronger foliation (Fig. 3.27 b, c). This foliation is defined by biotite, hornblende, and epidote. In one sample, the disruption of foliation by lobes of coarse quartz and feldspar provides evidence for the presence of melt during deformation (Fig. 3.27 b).

In thin section, the more silicic and complex nature of these rocks relative to the rest of the Misty Pluton is clear. In lower-strain L>S samples, networks of quartz and potassium feldspar separate domains of coarser plagioclase with deformation twins and undulose extinction (Fig. 3.27 d). Within the domains of quartz and potassium feldspar, these minerals are typically fine-grained and exhibit complex interdigitating grain boundaries. Quartz grains show both cuspate-lobate grain boundaries and subgrain domains, with chessboard subgrain patterns apparent in some coarser grains (Fig. 3.27 e). When in contact with potassium-feldspar, plagioclase exhibits myrmekitic textures. Biotite is also commonly found near boundaries between plagioclase and quartz + K-feldspar domains, often on the rims

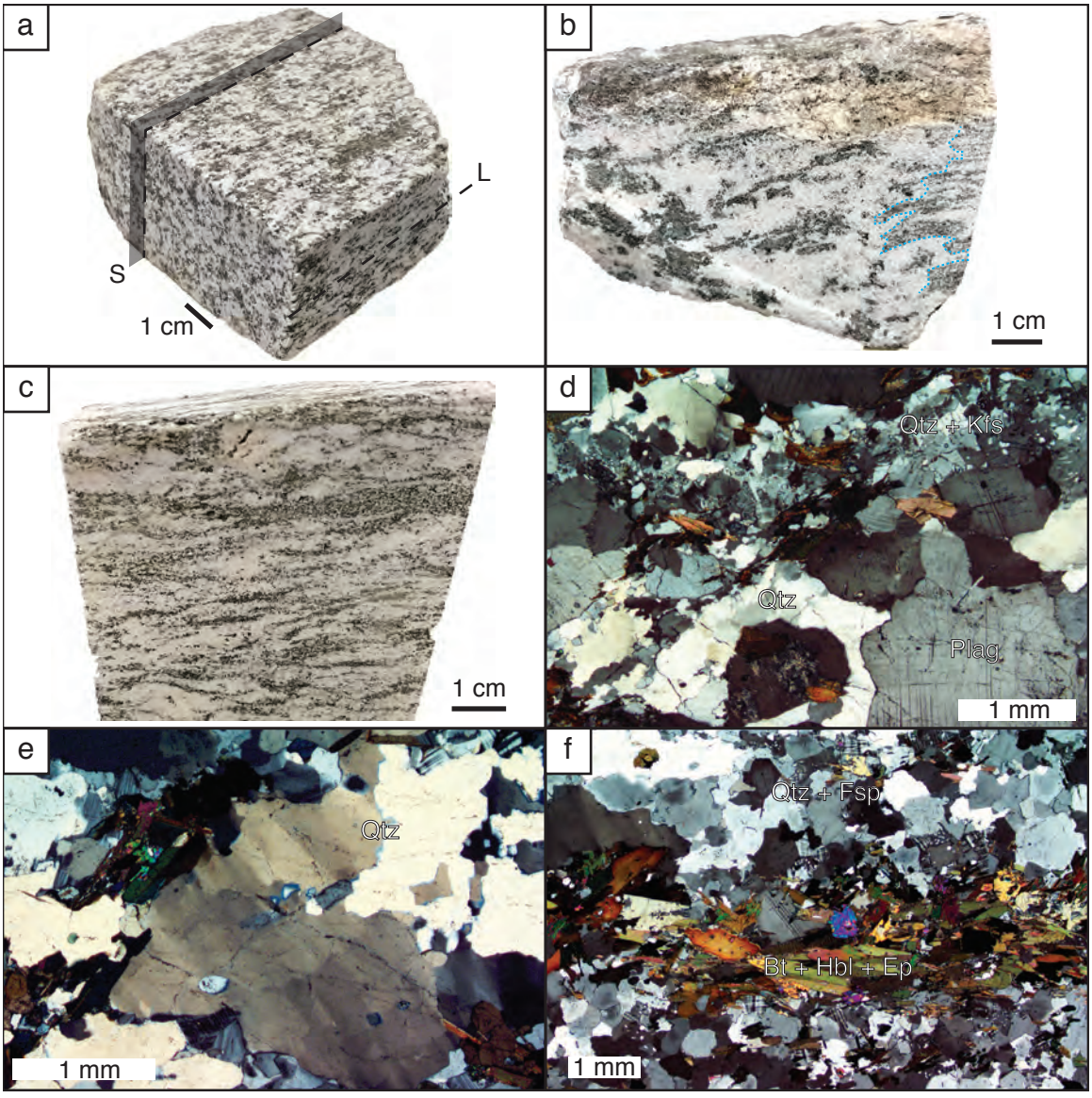

Figure 3.27: a) Low strain, L>S fabric in the Misty Pluton at Mary Peaks defined by biotite aggregates. Petrography suggests this sample is a hybrid of dioritic Misty Pluton and granitic Large Granite material. Sample 19MP14B. (b) Evidence for the overprinting of deformation fabrics by magmatic fabrics in sample 19MP19D (float) with lobes of coarse feldspar, biotite, and hornblende interrupting a finer-grained foliation that is more clearly shown in (c), sample 19MP19C (float). (d) In low-strain sample 19MP14B, coarse grains of plagioclase are separated by networks of fine-grained quartz and feldspar. (e) Quartz grains with cuspate-lobate grain boundaries and chessboard subgrain patterns in sample 19MP19B. (f) In 19MP19D—higher strain than 19MP14B—aggregates of biotite, hornblende, and epidote bounded by zones of mixed feldspar and quartz. Quartz and feldspar exhibit cuspate-lobate grain boundaries, and quartz contains subgrain domains.

of plagioclase grains and sometimes growing along fractures or twin planes. Biotite rims are also present on very fine epidote grains. In one thin section (19MP14A), small fragments of garnet intergrown with biotite are present.

The higher-strain, foliated samples exhibit similar quartz and feldspar microstructures, with irregular grain shapes and cuspate-lobate grain boundaries more apparent in feldspar. Between mafic folia, plagioclase grains appear mixed in with quartz and potassium feldspar, rather than segregated in coarse domains as in lower-strain samples (Fig. 3.27 f).

The networks of quartz and potassium feldspar and high-temperature textures contained therein—interdigitating grains and symplectic textures—suggest possible infiltration of silicic melt into more dioritic material. A likely source for this silicic material is the nearby Large Granite, parts of which may have been assimilated into the Misty Pluton as the latter was intruded, melting some of the granitic material. Sub-solidus deformation textures in both the plagioclase and quartz + K-feldspar domains indicate some post-crystallization deformation. The mixing of these domains in higher-strain float samples, and the interruption of these fabrics by other magmatic textures suggests contemporaneous deformation and magma infiltration on the margin of the Misty Pluton.

High-strain Large Granite

The contact between the Misty Pluton to the west and Large Granite to the east appears defined by a ~1 meter-wide mylonitic zone composed of highly strained and grain-sized reduced granitic material. We infer the contact between the Misty Pluton and Large Granite at Mary Peaks to have originally been intrusive considering the evidence for the assimilation of granitic material in the Misty Pluton to the west and the lack of evidence for faulting near the mylonite. Foliation

in the mylonitic zone is defined by mica shear bands and alternating layers of fine-grained quartz and feldspar, and lineations are defined by elongate quartz grains. The foliations dips steeply to the east, striking N–S, with lineations plunging moderately to the SSE (Fig. 3.26). Asymmetric fabric elements are apparent on the macro scale, but even more clear in thin section, indicating sinistral shear sense.

In thin section, layers of recrystallized quartz and feldspar alternate on the scale of 100s of µm, with occasional intervening biotite and white mica shear bands (Fig. 3.28 a). Asymmetric fabric elements include S-C fabrics defined by quartz shear bands and sigmoidal plagioclase aggregates with recrystallized tails, which indicate sinistral shearing (Fig. 3.28 b). Within plagioclase aggregates, cuspate-lobate grain boundaries are common. Quartz throughout the thin section similarly exhibits such grain boundary textures and amoeboid grain shapes, as well as evident subgrain domains (Fig. 3.28 c).

The orientation of fabrics in this mylonite, the sinistral kinematics, and relatively high-temperature deformation fabrics suggest that it could be a segment of the George Sound shear zone system. It also lies along strike of the segments of the GSSZ identified at George Sound to the north.

Low-strain Large Granite

To the east of the mylonitic boundary with the Misty Pluton, the Large Granite is relatively homogeneous. The Large Granite is dominated by quartz and feldspar, but includes variable quantities of biotite, white mica, epidote, titanite, and opaque minerals. It comprises L>S fabrics with shallowly SSW-plunging mineral lineations defined by quartz and biotite, and steep, NE–SW-striking foliations (Fig. 3.26).

At the microscale, low-strain Large Granite samples are dominated by typically coarse quartz and feldspar exhibiting deformation textures. Amoeboid feldspar

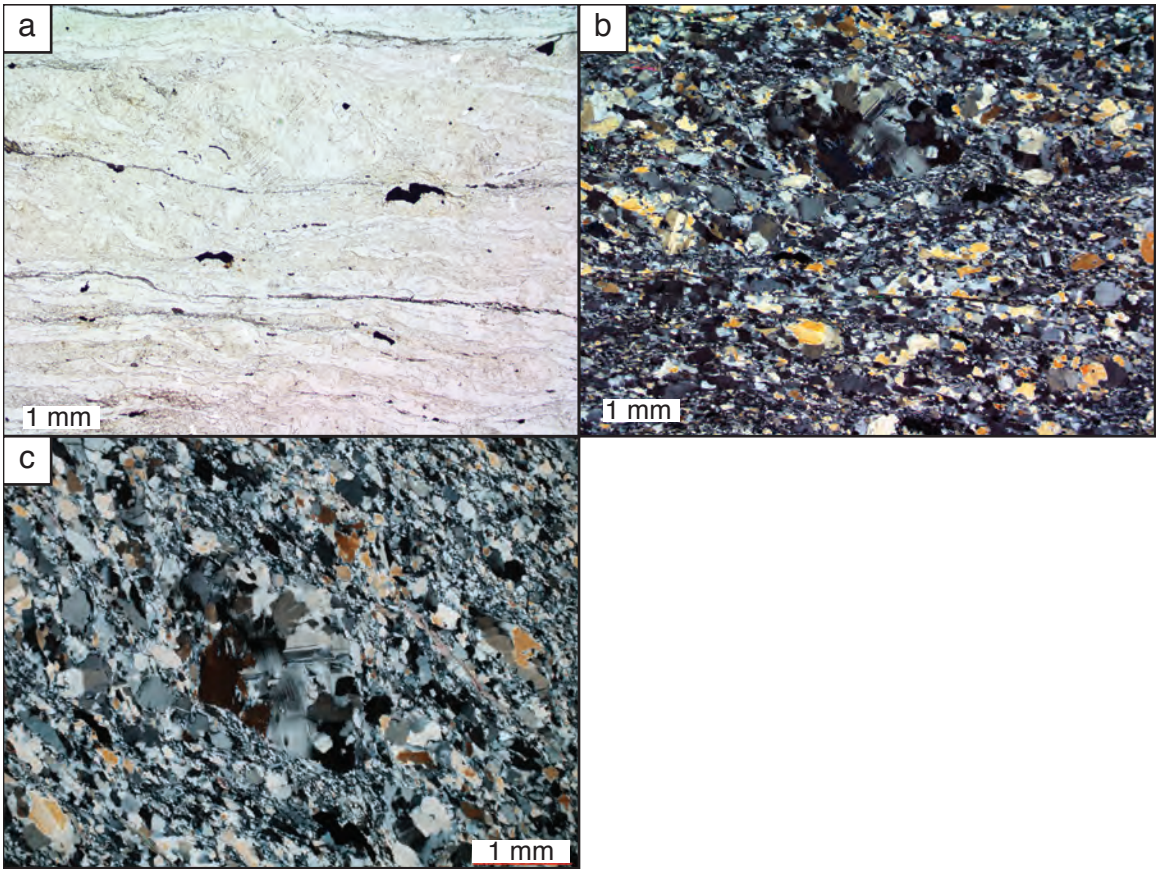

Figure 3.28: Microstructures of the mylonitic Large Granite in sample 19MP19E. (a) Alternating layers of quartz, feldspar, and mica are evident in PPL as feldspar appears darker than quartz. Opaque oxides are also aligned with the foliation. (b) The same field of view as (a) in XPL. The sigmoidal feldspar aggregate in the upper center of the image contains finely-recrystallized tails and indicates sinistral shearing. (c) More detailed view of the feldspar aggregate and surroundings in (b). Cuspate-lobate grain boundaries appear in feldspar within the aggregate at center and elsewhere, and elongate quartz grains may have subgrain domains.

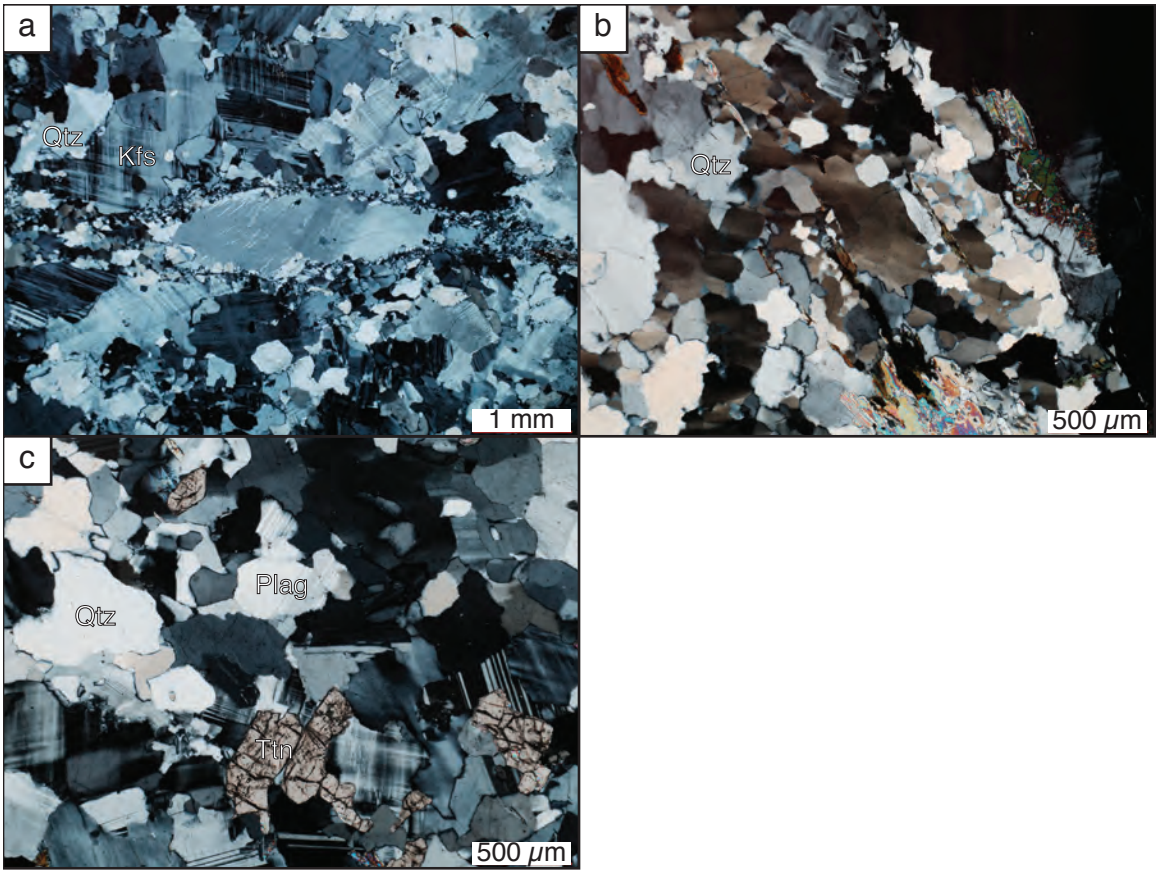

Figure 3.29: Microstructures of the low-strain Large Granite at Mary Peaks indicative of high-temperature deformation. (a) Elliptical feldspar grain exhibiting flame perthite textures and a core-mantle texture with apparent subgrain development along its margins in sample 19MP23. (b) Chessboard subgrain patterns in quartz grains in sample 19MP23. (c) Irregular grain shapes and cuspate-lobate grain boundaries in feldspar and quartz suggestive of GBM.

grains share cuspate-lobate grain boundaries, exhibit flame perthite textures, and in one sample feature core-mantle structures with apparent subgrain rotation (Fig. 3.29 a, c). Quartz grain boundaries are similarly cuspate-lobate and large grains may show chessboard subgrain patterns (Fig. 3.29). There are no clear kinematic indicators at the outcrop or microscale in this part of the Large Granite, so it is difficult to discern if these deformation textures are related to shearing in the George Sound shear zone.

The quartz and feldspar textures in the majority of the Large Granite exposed

Fabric Facies	N_{fol}, N_{lin}	Fréchet Mean	
		Strike/Dip	Trend/Plunge
Large Granite, mylonite	8, 5	356/78	167/42
Large Granite, low-strain	15, 27	031/87	200/31

Table 3.9: Statistical descriptors of foliation and lineation measurements from Mary Peaks treated as directional data.

at Mary Peaks are indicative of high-temperature deformation, and appear relatively low-strain compared to the mylonitized Large Granite to the west. Feldspar textures in these samples are comparable to those observed in plagioclase aggregate porphyroclasts in the mylonite (compare Fig. 3.29 to Fig. 3.28). If these porphyroclasts preserve relict textures of the mylonitized protolith, this would suggest that the mylonitic zone has reworked low-strain fabrics in the Large Granite. The orientation of these low-strain fabrics is comparable to the orientation of NE-striking foliation and shallowly SW-plunging lineations found in GSSZ fabrics at field areas farther south.

3.4.2 Statistical Analysis

There are clear distinctions between the orientations of fabrics from the different facies at Mary Peaks. In the low-strain to magmatic Misty Pluton fabric data, there are too few measurements of foliations and lineations and they do not exhibit any strong patterns that statistical analysis would help to characterize. In the Large Granite, the low-strain and high-strain fabric orientations define unimodal clusters in stereonets, so the statistical descriptors of mean and variance are appropriate for describing the fabric orientations (Fig. 3.26b). These are presented in table 3.9.

For the fabric data from the Large Granite, I rely on directional methods to perform statistical inference. Orientation statistics are not as useful in this case because the paucity of measurements from the mylonitic zone impedes the use of

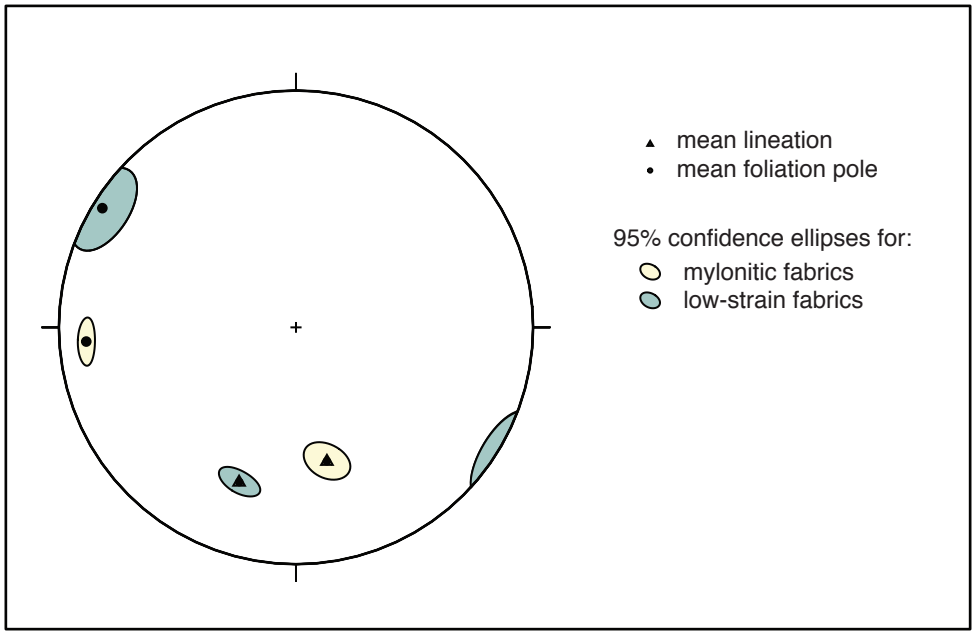

Figure 3.30: 95% confidence ellipses from bootstrapping directional foliation and lineation data from the different fabric facies in the Large Granite at Mary Peaks. There is a clear difference between the orientation of mylonitic and low-strain fabrics.

the MCMC simulation, and because the low-strain fabrics are primarily defined by lineation, so it is more informative to analyze the directions of lineations on their own. I construct 95% confidence ellipses for foliation and lineation directions separately using bootstrapping, which helps us to test whether or not the data from the mylonite and the rest of the Large Granite are derived from the same population. As is apparent in figure 3.30, the 95% confidence ellipses for the mylonite and the low-strain fabrics do not overlap, so there is evidence that we have sampled significantly different populations of fabric directions.

3.4.3 Summary

The mylonitic zone in the Large Granite is the fabric most readily correlated with deformation in the GSSZ. Its N–S-striking foliation connects with other strands of

the GSSZ along strike and sinistral shear indicators are consistent with known GSSZ kinematics. Geometrically, the fabrics in the Misty Pluton and the L>S fabric in the rest of the Large Granite may be consistent with GSSZ deformation. However, the lack of clear kinematic indicators limits our confidence in correlating these with the GSSZ, and geochronologic data (discussed below) suggest that the L-tectonite fabric in the Large Granite predates GSSZ deformation.

It is likely, however, that the rocks of the Misty Pluton to the west of the mylonitic zone were emplaced contemporaneously with GSSZ deformation, as evidenced by the overprinting of deformation fabrics by lobes of coarser, less deformed material (Fig. 3.27b). The fabrics in the samples of float immediately west of the mylonitic zone therefore must be related to GSSZ deformation, but it is unclear whether the measured fabrics at the western end of the transect represent magmatic flow or tectonic deformation. The N–S-trending mineral stretching lineations appear similar to lineation directions elsewhere in the GSSZ along the Misty Pluton margin, and may suggest a tectonic origin. The presence of melt in the Misty Pluton at Mary Peaks during deformation would also mask the full degree to which strain was accommodated in that unit during movement on the George Sound shear zone. When defining the 3D geometry of the GSSZ at Mary Peaks, we therefore include the low-strain fabrics in the Misty Pluton as a broad zone of variable foliations bounded to the east by the steep mylonitic zone in the Large Granite (Fig. 3.31).

Microstructurally, both high-strain and low-strain fabrics in the Large Granite indicate deformation at high temperatures. For the mylonitic zone, deformation at high temperatures is consistent with the syn-tectonic emplacement of the Misty Pluton to the west. Unpublished U-Pb zircon geochronology data from two dikes that crosscut the L-tectonite fabric in the lower strain Large Granite indicate that

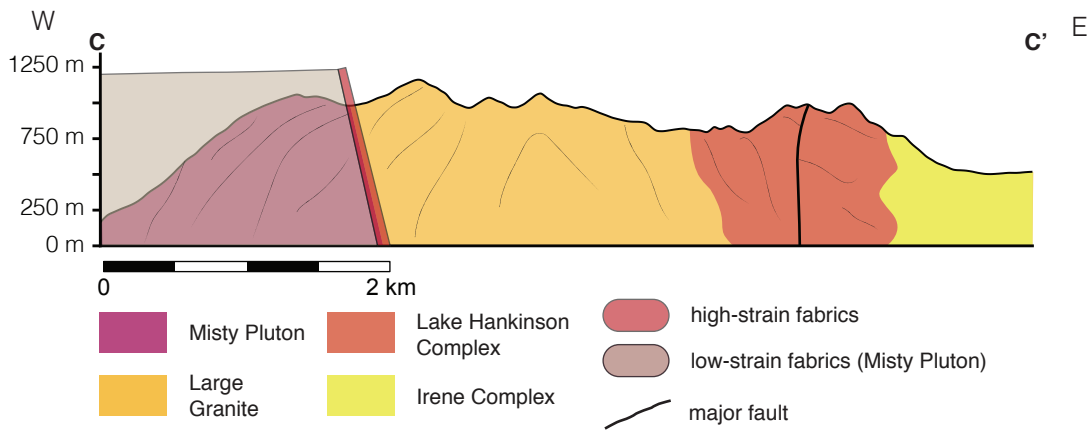

Figure 3.31: Cross section across the Mary Peaks field area. Step high-strain fabrics are confined to the western edge of the Large Granite, while the Misty Pluton's variable magmatic to low-strain tectonic fabrics are included as low-strain GSSZ fabrics.

this fabric is significantly older than the Early Cretaceous GSSZ. These U-Pb zircon analyses yield Carboniferous ages of 317.7 ± 4.4 Ma, and 319.4 ± 3.6 Ma (Schwartz, pers. comm., 2019), putting the timing of formation of the L-tectonite fabric closer to the emplacement of the Large Granite. The high-temperature microstructures within these fabrics may therefore may reflect deformation in a still-cooling pluton.

The mylonite zone along the western edge of the Large Granite that we suggest is part of the GSSZ therefore crosscuts the older L-tectonite fabrics. The age of these fabrics relative to the GSSZ also indicates that they did not develop as part of the GSSZ before strain was localized into the mylonitic zone. The differences between the directions of these fabrics (Fig. 3.30) is therefore explained by them resulting from at least two distinct episodes of deformation: one during the Carboniferous, and one during the Early Cretaceous.

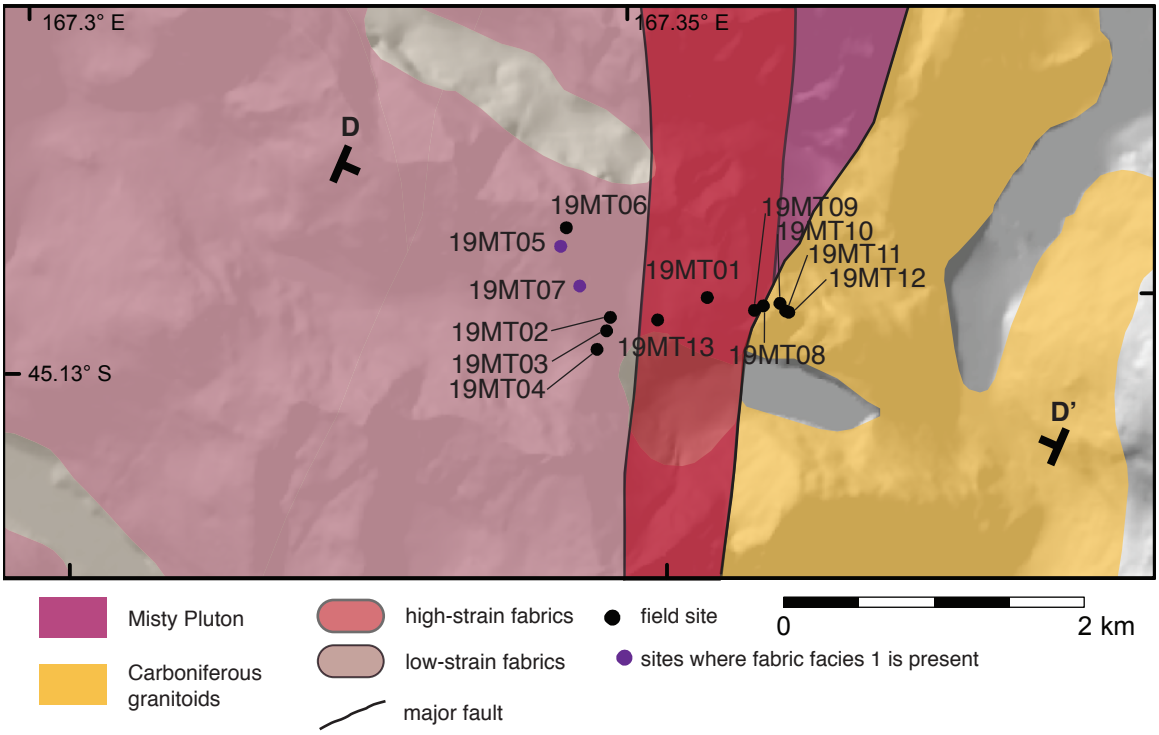

Figure 3.32: Detail geologic map of the Myth Tarn field area, showing the distribution of high and low-strain fabrics discussed in this section. The boundary between the Misty Pluton and Large Granite at this site is defined by a fault.

3.5 Myth Tarn

To the south of Mary Peaks, another transect across the margin of the Misty Pluton was conducted at Myth Tarn. At this field area, however, the George Sound shear zone appears to be contained entirely within the Misty Pluton, which shares a faulted contact with the Large Granite to the east (Fig 3.32). Within one kilometer of the fault, a low-grade, brittle overprint is present in the George Sound shear zone fabrics evidenced by microfaults cross-cutting amphibolite-grade fabrics and the replacement of biotite by chlorite.

Within the Misty Pluton in this area there appear two distinct types of fabrics: facies 1 and facies 2. In facies 1, the foliation is rough and defined by hornblende aggregates with internal quartz blebs, and in facies 2 there is a smooth foliation

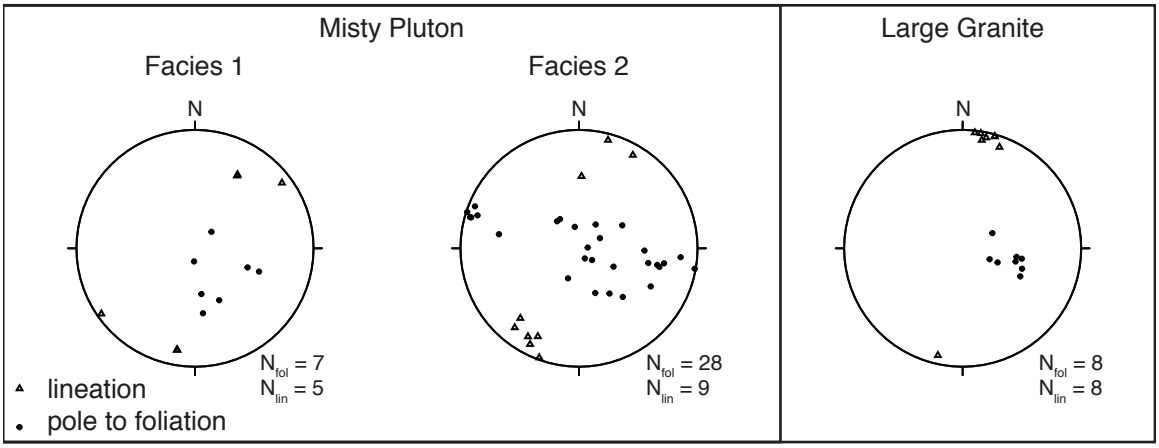

Figure 3.33: (a) Stereonets depicting the orientation of fabrics in the different fabric facies observed at Myth Tarn with two different fabrics present in the Misty Pluton.

defined by hornblende, biotite, and clinozoisite. The Large Pluton at Myth Tarn is characterized by L>S tectonites, similar to those at Mary Peaks. The Misty Pluton here is dominated by hornblende and plagioclase, with varying quantities of clinozoisite and biotite, and sometimes quartz. Garnet is rare and in facies 1 appears associated with leucocratic veins that cross-cut foliation (Fig. 3.34b), while in facies 2 garnet is wrapped by the foliation (Fig. 3.35c). The Large Pluton at Myth Tarn is characterized by L>S tectonites, similar to those at Mary Peaks.

3.5.1 Fabric facies

Misty Pluton Facies 1: Hornblende Aggregates

Some fabrics in the Misty Pluton are defined by the alignment of elongate hornblende aggregates that form a rough foliation (Fig. 3.34a). The aggregates are composed of fine-grained hornblende and the interior of the aggregates commonly contains quartz that is present in interstitial blebs between hornblende or as inclusions in the hornblende itself (Fig. 3.34c). Outside of the hornblende aggregates, plagioclase-dominated domains contain randomly-oriented euhedral

grains of biotite and epidote. Plagioclase itself exhibits amoeboid grain shapes with cuspate-lobate grain boundaries, and evidence for pinning of grain boundaries on biotite (Fig. 3.34d).

Although there are few measurements of fabric orientations for this facies, both orientations and foliation and lineation directions appear loosely clustered (Fig. 3.33). Foliations dip shallowly to moderately to the south and southeast, with lineations that plunge shallowly to the northeast and southwest.

Misty Pluton Facies 2: Smooth Foliation

The most common fabric at Myth Tarn is characterized by a smooth foliation defined by elongate grains of hornblende, biotite, and clinozoisite (Fig. 3.35a). At most stations, these smooth mafic layers alternate with plagioclase-rich layers, although the former may sometimes develop S-C fabrics that indicate sinistral, west-side down shear sense (Fig. 3.36a). Plagioclase exhibits straight or lobate grain boundaries and single grains often fill the space between mafic folia (Fig. 3.36b).

One kilometer to the west of the edge of the Misty Pluton, at station 19MT13, we see the highest-strain variety of fabric facies 2. Here, the Misty Pluton contains folded and boudined pegmatitic veins parallel to the subvertical foliation (Fig. 3.35d). Within the foliation, plagioclase-rich folia exhibit strong pinching and swelling, and mafic folia often appear to completely isolate plagioclase boudins, forming an interconnected network of mafic minerals (Fig. 3.36c). Plagioclase grains are elongate with the foliation, with grain boundaries that are either straight or lobate. Although little asymmetry is apparent on the micro-scale in samples from this zone, asymmetric folding of pegmatite veins (Fig. 3.35e) would be consistent with the sinistral shear sense observed in lower strain fabrics of facies 2.

The orientation of facies two fabrics follows a consistent pattern. Lineations

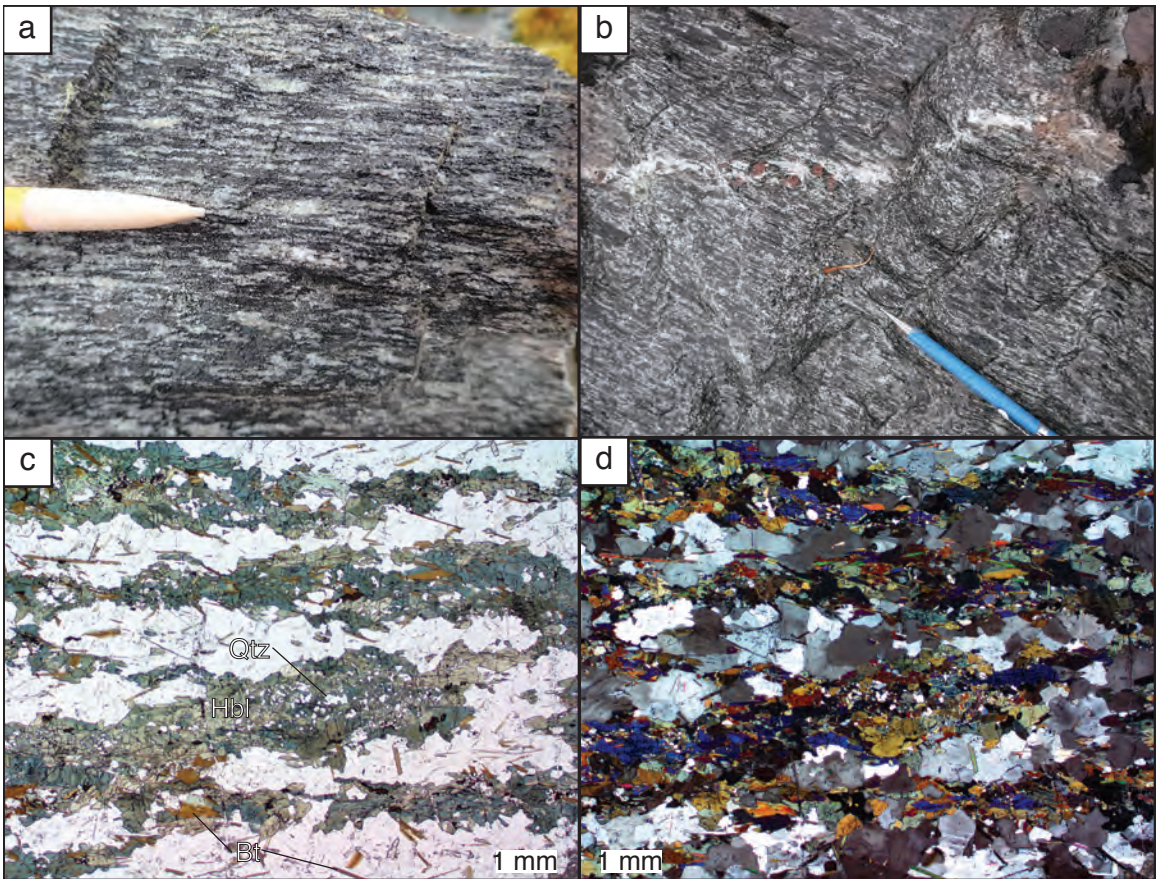

Figure 3.34: Examples of the facies 1 fabric in the Misty Pluton. (a) Rough foliation defined by hornblende aggregates at station 19MT07 where (b) a leucocratic vein with associated garnet crosscuts the foliation. (c) PPL photomicrograph of the hornblende aggregates with internal quartz blebs, suggestive of the retrograde breakdown of pyroxene. Euhedral biotite and epidote appear randomly oriented within the plagioclase domains. (d) XPL photomicrograph of the same view as (c) to show plagioclase grain textures including: amoeboid grains with cuspate-lobate grain boundaries and pinning by biotite. Photomicrographs in (c) and (d) are from sample 19MT05.

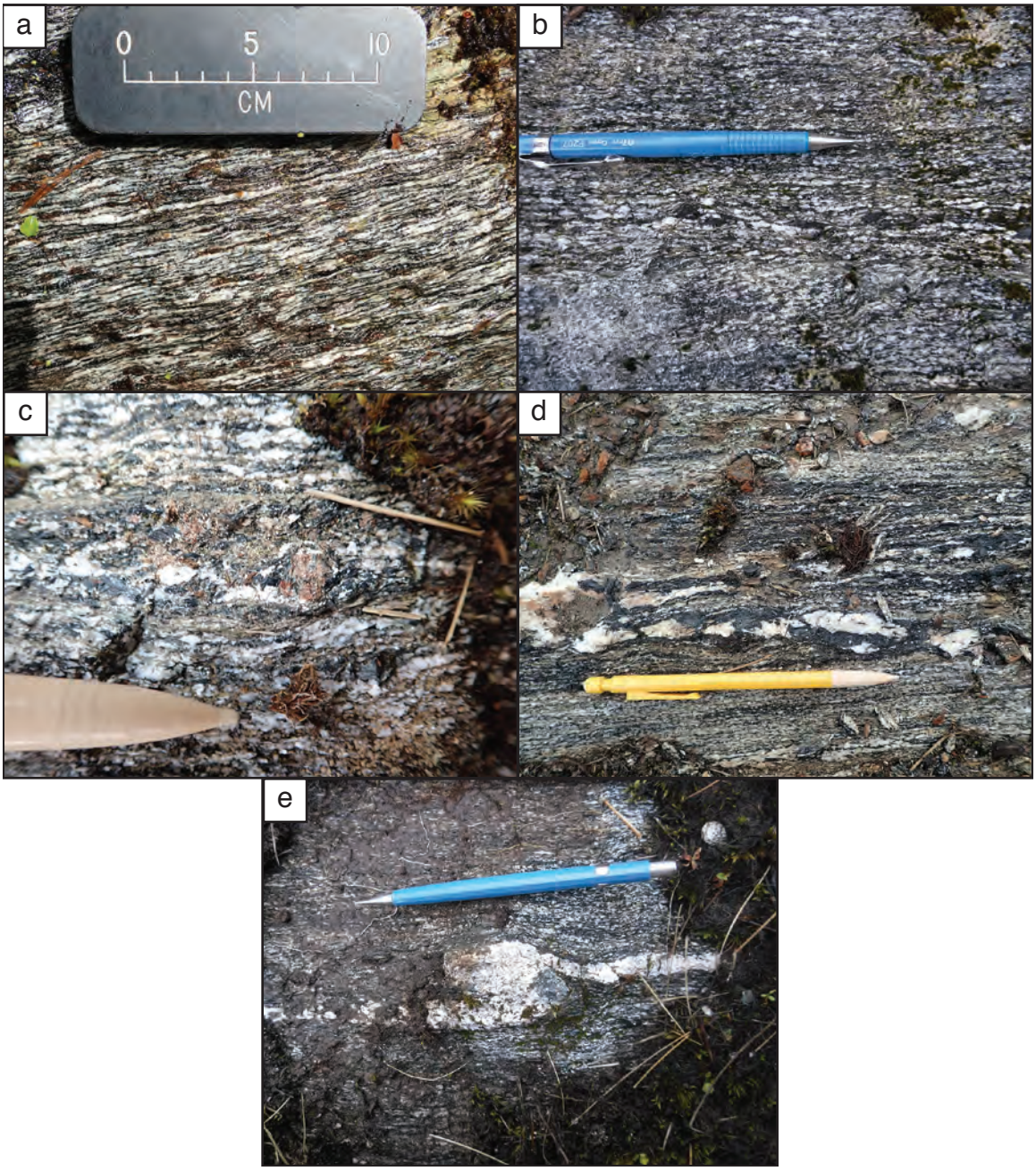

Figure 3.35: Field photos of (a) low-strain and (b, c, d, e) high-strain examples of fabric facies two from the Misty Pluton. (a) Smooth foliation defined by alternating layers of mafic minerals and plagioclase at station 19MT03. (b) Foliation is still smooth and defined by networks of mafic minerals, but plagioclase-rich layers have been boudined. Garnet in (c) is wrapped by the foliation. In (d) and (e), pegmatitic veins have been folded and, in (d), boudined. High-strain fabrics found at station 19MT13.

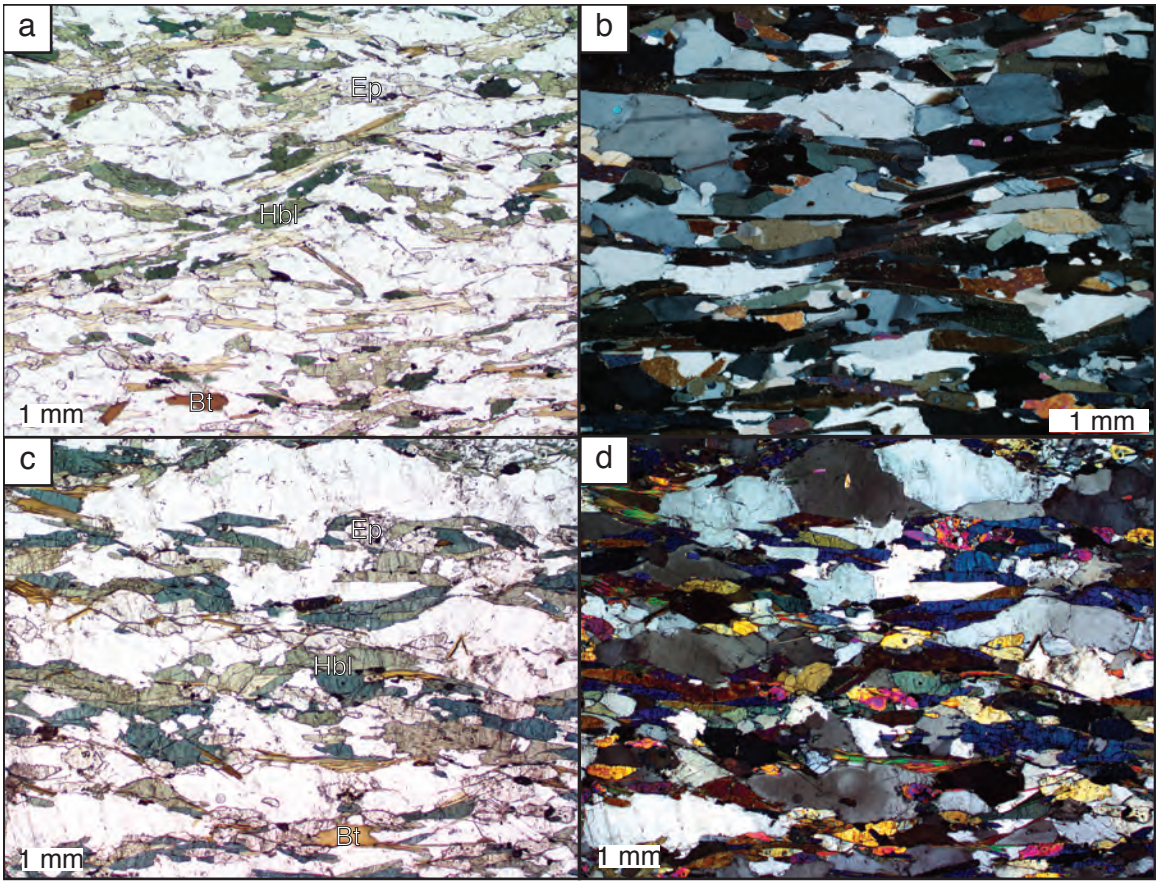

Figure 3.36: Photomicrographs of the facies two Misty Pluton fabrics. (a) Hornblende, biotite, and epidote form an S-C fabric in 19MT06 suggestive of left-lateral shearing. (b) In XPL, plagioclase grains in 19MT06 appear elongate parallel to the foliation and feature straight grain boundaries with adjacent plagioclase, but may have cuspate to lobate phase boundaries with biotite or hornblende, appearing to fill in irregularities in these minerals. In (c) and (d), high-strain fabrics from 19MT13 are defined by similar hornblende, biotite, and epidote folia, but plagioclase domains appear boudined with the mafic minerals forming and interconnected network. In (d) deformation twins and straight to lobate grain boundaries are apparent in plagioclase.

plunge shallowly to the NE and SW, while foliation poles define a girdle representing NE-striking planes that range from subhorizontal to subvertical (Fig. 3.33). When these data are colored by their position along an azimuth of 115—roughly perpendicular to the trend of the contact between the Large Granite and the Misty Pluton—a spatial gradient becomes apparent, with shallow foliations found farthest from the contact and steepening foliations from NW to SE towards station 19MT13 (Fig. 3.38). The deflection of fabrics and the relatively higher-strains in the subvertical fabrics near the boundary with the Large Granite are consistent with a west-side down sense of motion on the George Sound shear zone.

Large Granite

The Large Granite is in faulted contact with the Misty Pluton at the eastern end of the transect at Myth Tarn. Here, the Large Granite is dominated by fine-grained quartz, potassium feldspar, and plagioclase feldspar, with minor epidote, biotite, white mica, and opaque oxides. The L>S fabric in this rock is defined by the alignment of biotite and quartz into thin, discontinuous layers (Fig. 3.37a). Fabric orientations are consistent near the contact with the Misty Pluton, with foliation dipping moderately to the ESE, and subhorizontal lineations trending NNE–SSW (Fig. 3.33).

In thin section, the Large Granite shows evidence for recrystallized quartz and feldspar as part of its L>S fabric. White mica and biotite are the clearest fabric-defining elements and form very thin layers that can be up to 1–2 cm in length. Opaque oxides and epidote are commonly associated with these layers and are often oriented parallel to the foliation/lineation (Fig. 3.37b). Amoeboid and ribbon-like quartz grains feature lobate grain boundaries, exhibit undulose extinction, and may contain subgrain domains (Fig. 3.37c). Feldspar has highly

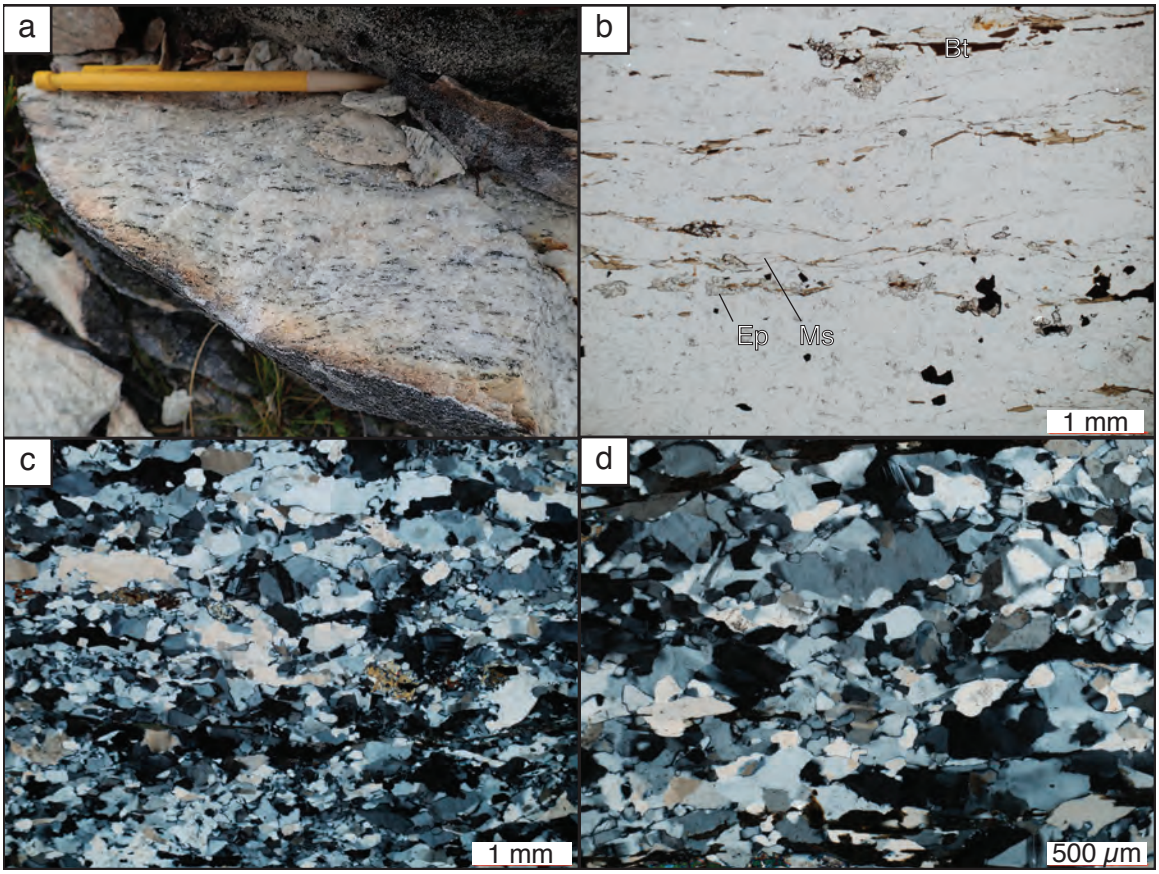

Figure 3.37: (a) In the field, the Large Granite at Myth Tarn exhibits a clear biotite lineation and foliation. (b) In thin section, white mica, biotite, epidote, and opaques can be seen defining the fabric, as well as (c) elongate quartz grains. Quartz shows strongly lobate grain boundaries, as well as some subgrain domains in larger grains. (d) Irregular, interlocking feldspar grains

irregular grain shapes that form an interlocking texture, with individual grains containing deformation twins (Fig. 3.37d).

3.5.2 Statistical Analysis

The apparent spatial dependence of fabrics in the Misty Plutons and deflection of foliation directions into the high-strain zone prompts me to perform a geodesic regression to describe the change in orientaiton. For this, I combine foliation data from both of the Misty Pluton fabric facies because the facies one foliation poles lie

close to the girdle defined by poles from facies one, and their inclusion does not interrupt the color gradient when the data are colored by their position along an azimuth of 115°. Both facies one and facies two are also consistent with deformation at amphibolite facies conditions, and may have formed as a result of deformation in the GSSZ, so a deflection related to motion on a high-strain zone could have affected both fabrics. The geodesic regression is displayed graphically in figure 3.38, in which a great circle arc fits the foliation poles. This represents a rotation axis with a trend/plunge of 008/08, and the regression predicts an anti-clockwise rotation of 91° per kilometer along the azimuth 115°. Permutation tests yield a p-value of 0, so the spatial dependence of foliation directions is significant. These analyses are consistent with the observed steepening of foliation from west to east along the transect, and provide an example of what might be expected were other transect across the margin of the Misty Pluton to be conducted.

For the purposes of statistical inference, I isolate the fabric data from the high-strain zone in the Misty Pluton, which come from stations 19MT13 and 19MT01. I do this because of their apparent higher-strain fabrics than elsewhere in the Misty Pluton at Myth Tarn and because the fabrics from these stations define a unimodal cluster that is describable via the Fréchet mean and variance. It will also be useful to compare these fabrics orientations to those of other high-strain fabrics in the GSSZ.

Fabric measurements from Myth Tarn are best analyzed using directional statistics. The orientation data for the high-strain Misty Pluton fabrics in facies two and for the Large Granite fabrics are too few to conduct statistical inference using the MCMC method. The Large Granite also contains L>S tectonites, so it is most informative to focus on the directional lineation-only data. Within the high-strain fabrics, we were able to collect only two lineation measurements, so I concentrate

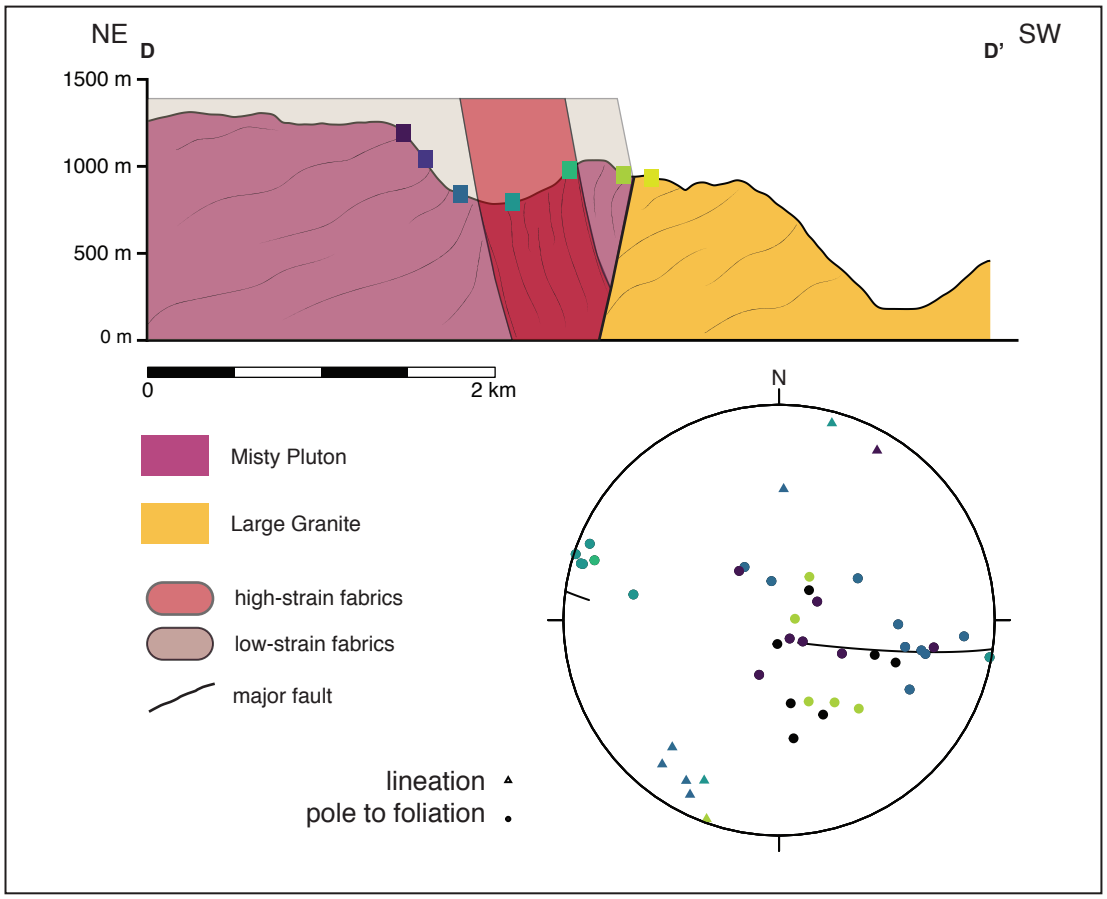

Figure 3.38: Cross section across the Misty Pluton margin and GSSZ at Myth Tarn, showing low-strain fabrics being deflected into a high-strain zone. Included below the cross section is a stereonet with foliation and lineation data from the Misty Pluton colored by their position on a heading of 115°. The color gradient shows that foliation in the Misty Pluton generally steepens towards the east. Colored squares corresponding to the colors of the data on the stereonet represent where along the transect the data came from. The segment of great circle is the best fit of the geodesic regression discussed in the statistical analysis.

Fabric Facies	N_{fol}, N_{lin}	Fréchet Mean	
		Strike/Dip	Trend/Plunge
Large Granite	8, 8	193/33	013/03
Misty Pluton, high strain	7, 2	016/81	N/A
Misty Pluton, all lineations	16	N/A	027/00

Table 3.10: Statistical descriptors of foliation and lineation measurements from Myth Tarn treated as directional data.

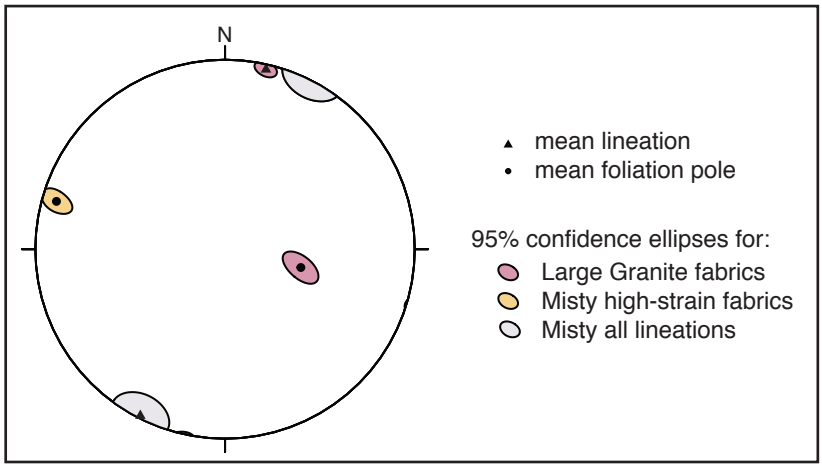

Figure 3.39: 95% confidence ellipses from bootstrapping directional foliation data for the high-strain fabric in the Misty Pluton and foliation and lineation data from the Large Granite.

statistical inference on the foliation data from stations 19MT13 and 19MT01. The average foliation and lineation directions for these groups are presented in table 3.10. Bootstrapping these directional data yields 95% confidence ellipses for the mean foliation directions from high-strain fabrics in the Misty Pluton, and the mean foliation and lineation directions in the Large Granite (Fig. 3.39). I also combine all the lineation measurements from the Misty Pluton and perform bootstrapping because they all plunge gently to the NE and SW. Despite having similar gently-plunging lineations, the direction of lineations in the Large Granite are significantly different from those in the Misty Pluton at Myth Tarn.

3.5.3 Summary

Within the Misty Pluton, both facies one and facies two fabrics likely represent deformation as part of the George Sound shear zone. Both fabrics show evidence of deformation at amphibolite facies conditions—in mineral assemblage and in plagioclase GBM textures—and facies two fabrics contain sinistral, west-side down shear sense indicators. Although clear shear sense indicators were not observed in facies one, its fabrics are geometrically compatible with those of facies two. The textural differences between these fabrics may be the result of variations in starting lithologies. Primarily, facies one contains evidence for the retrograde breakdown of pyroxene into hornblende and quartz, while facies two contains no evidence for the previous existence of pyroxene. Local variation in the Misty Pluton between pyroxene diorite and hornblende diorite is consistent with the observations of other authors, and relict pyroxene within dominantly hornblende diorites has been observed elsewhere in the Misty Pluton (Allibone et al., 2009).

Unlike at the previous field areas, high-strain fabrics at Myth Tarn do not appear to correlate with rocks with different lithology or metamorphic history. The steep high strain zone is composed of facies two fabrics, but these fabrics also appear to the west of this zone with much shallower foliation. The primary differences between the higher and lower strain fabrics are in the texture and orientation of these. The hornblende, biotite, and clinozoisite in the high-strain fabrics define a more interconnected network, perhaps allowing for more slip along grain boundaries and reducing the overall strength of these rocks. Why these textures developed where they did in the shear zone, however, is unclear. The development of the steep, high-strain fabrics may be the result of localization along a lithologic contact—i.e. the intrusive margin of the Misty Pluton. However, the

boundary with the Large Granite to the east is faulted, so it is unclear how close this part of the Misty Pluton was to the original contact.

Foliation and lineation directions within the Large Granite appear roughly parallel to some fabrics in the adjacent Misty Pluton. Lineation directions, however, are the main structure in the Large Granite and do differ significantly between the two units (Fig. 3.39). The Large Granite also lacks obvious shear sense indicators at Myth Tarn. Quartz GBM textures in the Large Granite here also indicate high temperature deformation, but, as at Mary Peaks, it is possible this deformation predates the GSSZ.

3.6 Southern Misty Margin

The southernmost field areas containing rocks of the George Sound shear zone are Coronation Saddle, visited in 2005, and Cozette Burn, visited in 2015. Both of these areas feature transects across the eastern margin of the Misty Pluton (Fig. 3.40). Because of their proximity to each other and similar geology, I lump these field areas into the "Southern Misty Margin" region. Both transects cross screens containing material from the Cozette Pluton and surrounding metasedimentary host rock that were incorporated into the Misty Pluton. At both field areas, later deformation recorded by ≤ 10 m-thick mylonitic shear zones cross-cut and deflect the fabrics of the GSSZ (Blatchford, 2016).

3.6.1 Fabric facies

Similar GSSZ fabrics appear at both Cozette Burn and Coronation Saddle. These have previously been described by Blatchford (2016), so I will simply summarize these fabrics and the major structures here, and present my statistical analyses of

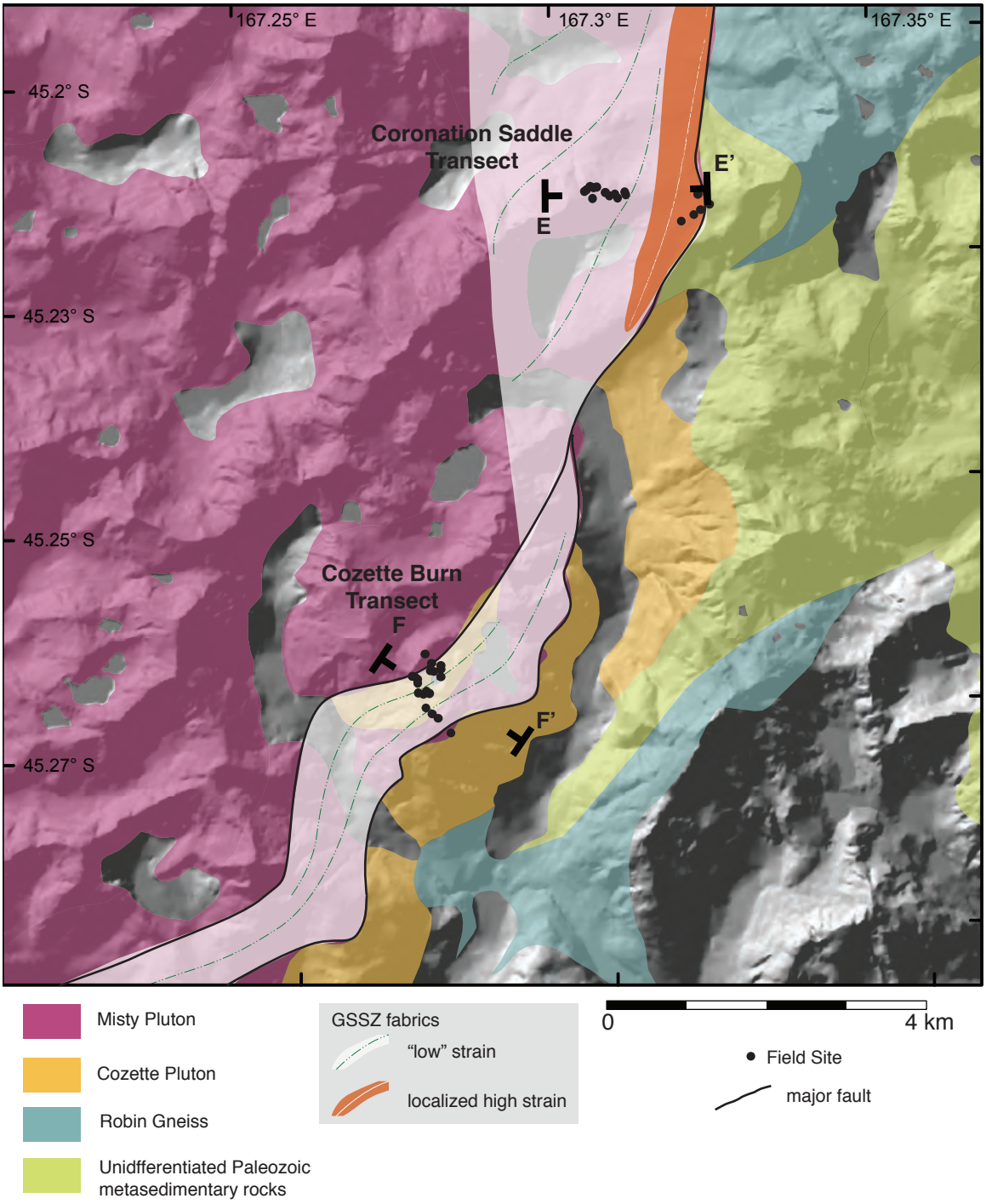

Figure 3.40: Map of southeastern margin of the Misty Pluton showing the location of field sites from the Coronation Saddle (2005) transect and Cozette Burn (Camp 2, 2015) transects. Data from Cozette Burn mostly come from within a fault-bounded slice of the Misty Pluton and a screen of the Cozette Pluton

the structural data. Blatchford identified several phases of deformation in this region, but I will only focus on the foliations and mineral lineations in the Misty Pluton and Cozette Pluton that are part of the phase she termed D_2. Blatchford used these D_2 fabrics to define the "Misty shear zone," but I will argue that these fabrics may be correlated with fabrics that appear to the north at Myth Tarn, and therefore are part of the larger George Sound shear zone system.

Along its southeastern margin, the Misty Pluton is characterized deformation fabrics defined primarily by hornblende aggregates, although igneous textures are locally preserved in parts of the Misty Pluton. At Coronation Saddle, isoclinal folds of igneous fabrics also help to define the deformation fabrics (Blatchford, 2016). The shape preferred orientation of hornblende and feldspar aggregates, are the most ubiquitous fabric-defining feature in the Misty Pluton in the region (Fig. 3.41; Blatchford, 2016). Hornblende aggregates commonly contain quartz blebs in the interior of the aggregates, similar to those in the facies one fabric observed at Myth Tarn (Fig. 3.34). A sample taken from a dioritic dike within the screen of Cozette Pluton at the station 15AB-72 contains relict pyroxene surrounded by finer-grained hornblende and blebs of quartz (Fig. 3.41d). This suggests that the quartz inclusion texture observed in hornblende aggregates elsewhere along the Southern Misty margin and at Myth Tarn may be the result of the complete replacement of pyroxene by hornblende and quartz. Relict, coarse igneous plagioclase grains are common (Fig. 3.41a, c), suggesting emplacement of the Misty Pluton and deformation in this region overlapped in time. Some plagioclase aggregates contain these relict igneous grains surrounded by fine, recrystallized plagioclase grains that share lobate grain boundaries and a strong LPO (Fig. 3.41c).

Deformation in the Cozette Pluton is most apparent in the screen of granitic material at the Cozette Burn field area. Here, the Cozette Pluton exhibits gneissic

layering of quartz ribbons and zones of feldspar (Blatchford, 2016). Quartz ribbons contain elongate subgrain domains, and feldspar zones are comprised of fine-grained feldspar with amoeboid shapes and lobate, interlocking grain boundaries (Fig. 3.41e).

At Coronation Saddle, fabrics exhibit variable orientations. In the Misty Pluton above the screen of host rock material, fabrics primarily consist of foliation visible at the outcrop scale, but igneous textures are preserved at the microscale (Fig. 3.41a). These foliations consistently dip moderately to the N and NW (Fig. 3.42). Fabrics within the screen of granitic material and in the Misty Pluton below this screen—between the screen and the eastern margin of the Misty Pluton—share NE- or SW-trending, shallowly to moderately-plunging lineations. From west to east over the 1 km-long transect, however, there is a gradual transition from unorganized, moderately dipping foliations in the west, to NNE-striking, moderately to steeply-dipping in the east. This is apparent in the color gradient in Figure 3.42 when foliation poles are colored by their east-west position along the transect. The steep foliations in the east correspond to the most well-developed deformation fabrics present at the margin of the Misty Pluton. This pattern is similar to that observed at Myth Tarn.

At Cozette Burn, fabrics in the Misty Pluton and Cozette Pluton parallel each other, with foliations that dip moderately to the N and NW, and NE-trending, shallowly to moderately plunging lineations (Fig. 3.42). Foliations at Cozette Burn parallel those found above the screen of granitic material at Coronation Saddle. Blatchford (2016) also reports that the orientation of magmatic flow fabrics in the Misty Pluton at Cozette Burn parallel the deformed fabrics.

The fabrics at Cozette Burn and Coronation Saddle both contain kinematic indicators representative of sinistral, reverse motion, with the west-side of the shear

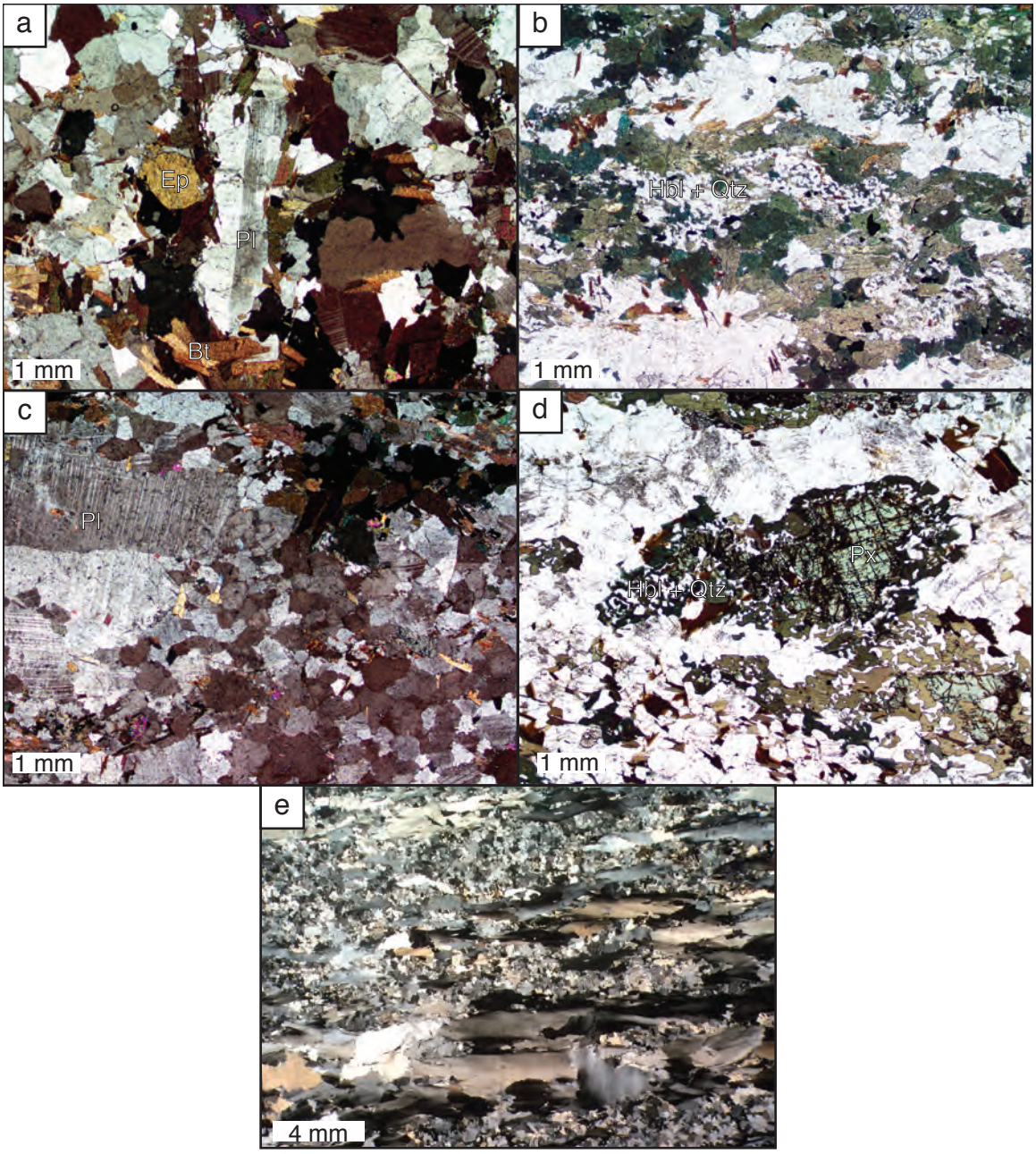
a
Ep
Pl
Bt
1 mm
b
Hbl + Qtz
1 mm
c
Pl
1 mm
d
Px
Hbl + Qtz
1 mm
e
4 mm

Figure 3.41: Microstructural characteristics of the fabrics at Coronation Saddle and Cozette Burn. (a) Relict igneous plagioclase and a generally coarse-grained, irregular feldspar grains in the Misty Pluton at station 05-03-01, the station farthest west of the Misty Pluton edge at Coronation Saddle. Hornblende, biotite, and epidote do not exhibit a strong shape-preferred orientation. (b) Hornblende and feldspar aggregates that define the fabrics in the Misty Pluton at station 05-02-02. Hornblende aggregates commonly contain cores of quartz blebs. Compare to the facies one fabrics from Myth Tarn (Fig. 3.34). (c) Plagioclase with relict igneous textures, but recrystallizing margins and deformation twins in the Misty Pluton at station 05-02-02. Finer-grained feldspar in the right side of the image exhibit a strong LPO and cuspate-lobate grain boundaries. (d) Relict pyroxene surrounded by fine hornblende and quartz blebs. This may represent an early stage in the development of the hornblende aggregates with cores of quartz blebs present in the Misty Pluton elsewhere along the Southern Misty margin and at Myth Tarn. From a dioritic dike within a screen of the Cozette Pluton at station 15AB-72. (e) Microstructural characteristics of the Cozette Pluton at station 15AB-72. Quartz ribbons with elongate subgrain domains alternate with zones of fine, amoeboid feldspar grains suggestive of grain boundary migration. From Blatchford (2016).

zone moving to the SW over NW-dipping foliations (Blatchford 2016). The sinistral component of motion is consistent with observed shear sense elsewhere in the George Sound shear zone. It is, however, unclear what the significance of the vertical component of deformation is as the exposures of GSSZ fabrics in the Southern Misty Margin are bounded by later ductile and brittle structures that may have reoriented. The shallow NE–SW-trending lineations, however, are consistent with those observed to the north at Myth Tarn and Mary Peaks.

3.6.2 Statistical Analysis

To analyze the structural data from the Southern Misty Margin area, I consider three groups of data from the two field regions. All of the F_2 and L_2 data from Blatchford's Cozette Burn (Camp 2) field area have similar orientations. Fabric measurements from the Cozette Pluton and Misty Pluton are combined here because the fabrics in each of these are parallel to each other (Fig. 3.42), and because of the evidence that igneous fabrics in the Misty Pluton are concordant

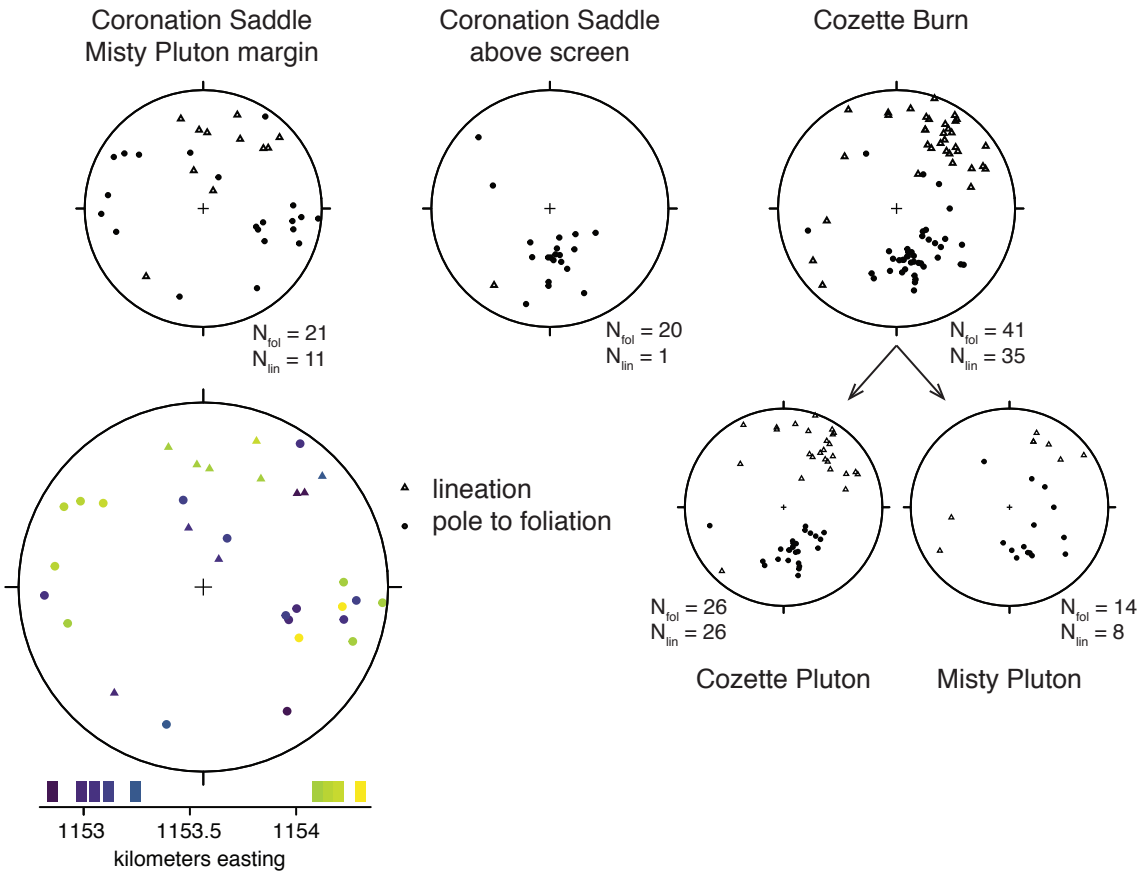

Figure 3.42: Equal-area stereonets depicting the orientation of fabrics from the Coronation Saddle and Cozette Burn transects across the Misty Pluton margin. Breaking fabrics from Cozette Burn into those from the Misty Pluton and those from the Cozette Pluton reveal how similar measurements from the two are. Foliation and lineation data from Coronation Saddle are also colored by their UTM easting coordinates to demonstrate the steepening of foliation from west to east in the Misty Pluton, correlating with the development of more well-defined, potentially higher strain fabrics.

Fabric Facies	N_{fol}, N_{lin}	Fréchet Mean	
		Strike/Dip	Trend/Plunge
Cozette Burn, orientations	30 pairs	254/33	032/24
Cozette Burn, directions	41,35	245/33	033/23
Coronation Saddle, above screen	20,1	268/38	N/A
Coronation Saddle, high strain	10,5	016/90	007/30

Table 3.11: Statistical descriptors of foliation and lineation measurements from the Southern Misty Margin treated as directional data.

with deformation fabrics in the Cozette Pluton across an intrusive contact between the two (Blatchford 2016). With the Coronation Saddle transect, however, I divide the measurements into those collected to the east of the screen of Cozette Pluton and those to the west. The variability of the measurements to the east of this screen do not lend themselves to description via Fréchet mean and variance (Fig. 3.42). However, it will be useful to analyze the orientation of the relatively high-strain fabrics from the four eastern field sites on the Coronation Saddle transect, which have similar steep, NNE-striking foliations and NE-plunging lineations. I will ultimately compare these to the orientation of the similar relatively high-strain fabrics from Myth Tarn. A summary of average fabric orientations and directions is given in table 3.11.

An abundance of paired foliation-lineation data from Cozette Burn allow me to conduct statistical inference using these orientation data, although I also perform inference on the directional data for comparison to datasets without foliation/lineation pairs. The statistical descriptors are listed in table 3.11 and the 95% confidence/credible regions from MCMC simulations using orientation data and bootstrap simulations using directional data are presented in figure 3.43. The lack of paired foliation and lineation data, or of lineation data in general in the Misty Pluton to the west of the screen of host rock prompts me to perform statistical inference using the foliation directions only. Bootstrapping these data

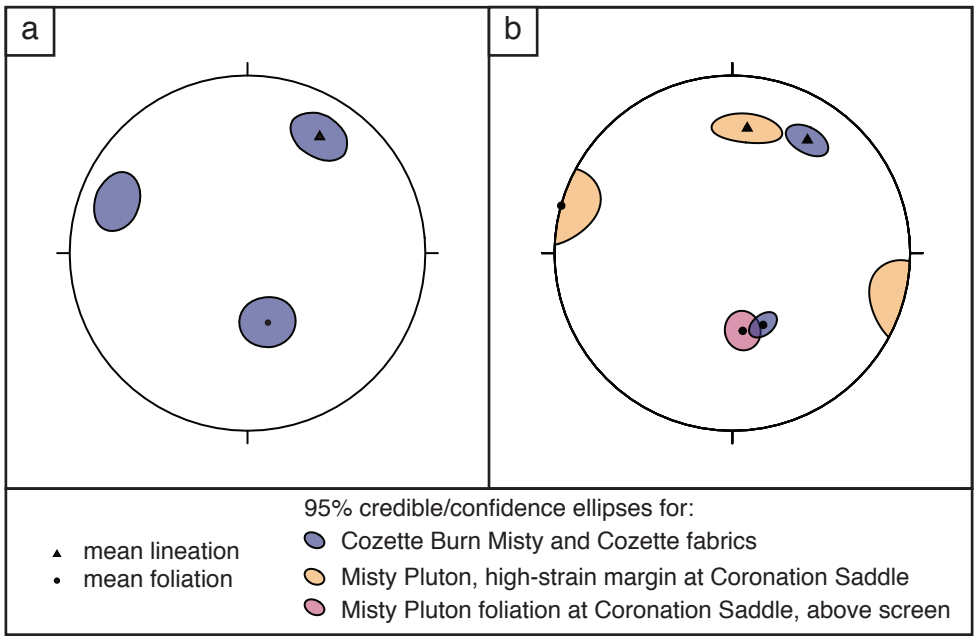

Figure 3.43: (a) MCMC 95% credible ellipsoid for the fabrics at Cozette Burn projected onto a lower-hemisphere stereonet. (b) 95% confidence ellipses from bootstrapping foliation and lineation data separately. The higher-strain fabrics from the eastern edge of the Coronation Saddle transect have a distinct orientation that differs from those fabrics at Cozette Burn.

yields a 95% confidence interval for the mean of this population of planar fabrics, which overlaps with that of the foliation poles at Cozette Burn. I also apply bootstrapping to both the foliation and lineation directions from the high-strain fabrics at the eastern end of Coronation Saddle to construct 95% confidence ellipses (Fig. 3.43). The lack of overlap between the confidence ellipses from these high-strain data confirm that the lineation directions from this zone are significantly different from those at Cozette Burn.

3.6.3 Summary

The Misty Pluton at Coronation Saddle and Cozette Burn contains a very similar fabric and both are consistent with deformation in the GSSZ. Mineral assemblages, metamorphic textures indicating the breakdown of pyroxene into hornblende, and

microstructural evidence for plagioclase subgrain rotation indicate deformation at high-temperature, amphibolite facies conditions. Both field areas also contain sinistral shear sense indicators. In the screen of Cozette Pluton at the Cozette Burn transect, quartz ribbons with elongate subgrains and plagioclase grain boundary migration textures are similarly suggestive of high temperature deformation. This, combined with parallelism of deformed fabrics in the screen of Cozette Pluton and the Misty Pluton (Fig. 3.42), and undeformed magmatic fabrics in the Misty Pluton, indicate that this whole margin of the Misty Pluton was sheared during and following its emplacement. The preservation of relict igneous textures, however, suggests that not much strain was accommodated.

The 3D geometry of the GSSZ along the southeastern Misty Pluton margin is represented in the two cross sections from each field area in figure 3.44. The most well-developed GSSZ fabrics in the Misty Pluton, represented in figure 3.41b, appear at the eastern edge of Coronation Saddle and have the characteristic steep, N–NE-striking foliations of high-strain GSSZ fabrics. The slight deflection of fabrics at Coronation Saddle (Fig. 3.42) and increasing organization of hornblende aggregates into these higher-strain fabrics suggests some strain localization affecting the orientation of earlier low-strain fabrics. These fabrics also have significantly different lineation directions than those in the Misty Pluton and Cozette Pluton to the south at Cozette Burn. As at Myth Tarn, the faulted eastern boundary of the Misty Pluton at this location obscures the extent of this higher-strain zone.

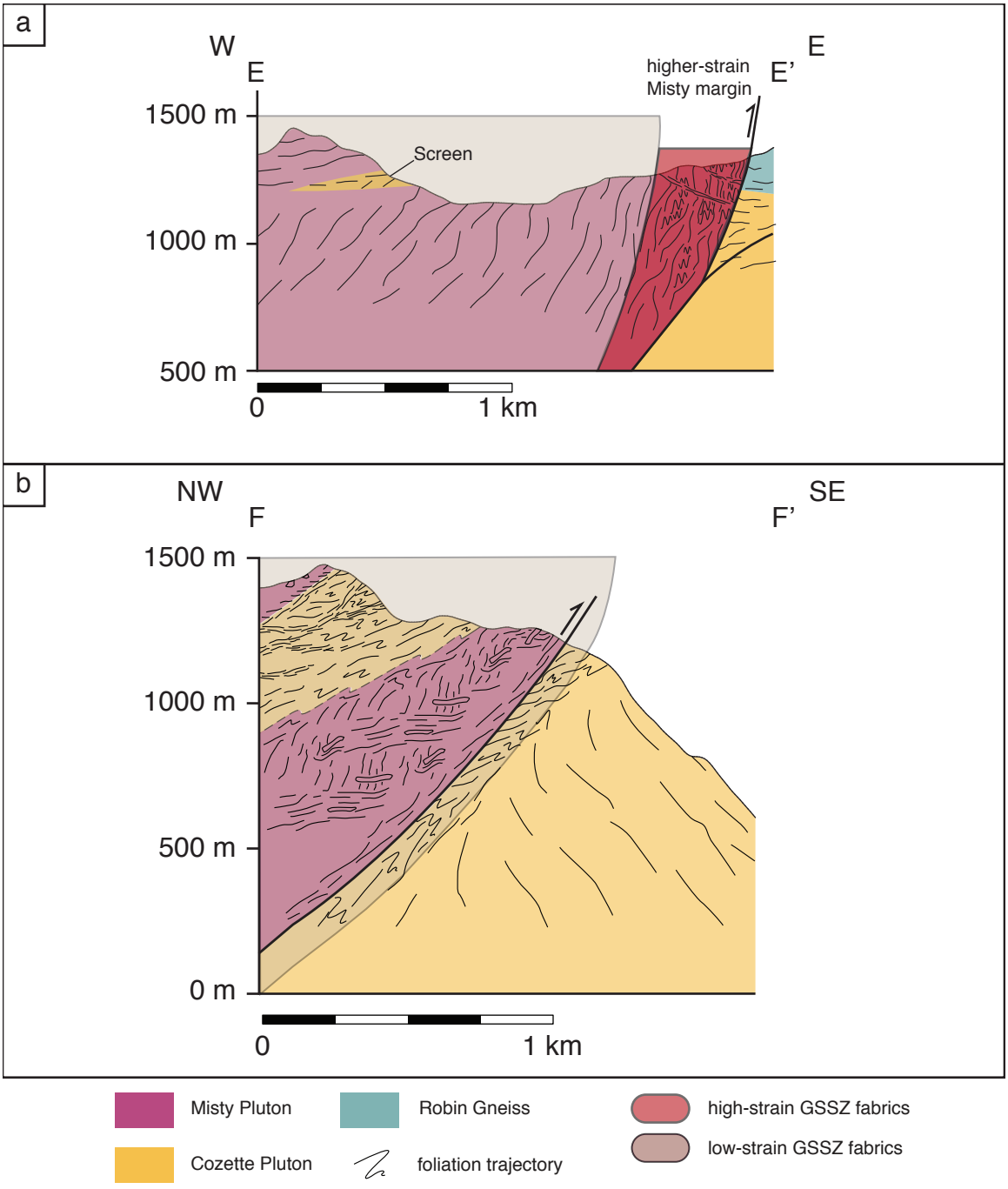

Figure 3.44: Cross sections across the Misty Pluton margin at (a) Coronation Saddle, and (b) Cozette Burn. Fabric orientations vary above and below the screen at Coronation Saddle (see Fig. 3.42), and relatively high-strain fabrics are found at the easternmost edge of the Misty Pluton. Only relatively low-strain fabrics that are comparable to those low-strain fabrics at Coronation Saddle and Myth Tarn are found in the Misty Pluton at Cozette Burn. The faults shown in these cross sections represent later, brittle reactivation of the GSSZ (Blatchford, 2016). Modified from Blatchford (2016).

Chapter 4

Discussion

The broad goals of this project are to characterize the architecture of the entire George Sound shear zone and to illuminate the process involved in its formation. In this chapter, I will: (1) link the structural observations presented for each field area and describe the geometry of the entire GSSZ; and (2) compare what the field, microstructural, and petrologic observations indicate about the formation and evolution of the GSSZ, and how these vary along the strike of the shear zone.

The GSSZ represents a part of a crustal-scale boundary within the Fiordland magmatic arc that was formed due to oblique convergence between Gondwana and subducting oceanic lithosphere of the paleo-Pacific ocean. The integrated picture of the GSSZ presented here provides a new view of the structure and behavior of a crustal-scale boundary at middle- to lower-crustal depths, which are rarely accessible directly by geologists. By providing an example of how deformation is accommodated in the lower crust, the GSSZ allows us to better understand how an entire crustal-scale boundary within a continent may deform.

4.1 Architecture of the George Sound shear zone

The entire George Sound shear zone is characterized by amphibolite grade fabrics that contain obliquely sinistral kinematic indicators. Although each field area presents only a slice of the GSSZ, mapping the extent of these fabrics at each field area and interpolating between transects, we construct a large-scale view of the entire shear zone system. These inferences are based on the roughly parallel N–S-striking shear fabrics at each field area, and on reported fabric orientations in the Fiordland QMAP database, which can fill in some gaps between field areas and allow us to make a smooth connection between the deformed zones (Turnbull et al. 2010). Extensions of branches of the GSSZ outside of the field areas, such as to the west of Myth Tarn and Mary Peaks are similarly inferred based on the presence of steep, N–S-striking foliations on the Fiordland QMAP. The map of the entire GSSZ is presented in figure 3.1, and a similar map showing the location of field sites from the Fiordland QMAP is shown in appendix A.

The George Sound shear zone is composed of two main N–S-striking zones—at Bligh Sound and south of George Sound—connected by a large right-stepping bend at George Sound where steep fabrics strike to the NE. At Bligh Sound, deformed fabrics define a zone roughly 10 kilometers wide, while along the margin of the Misty Pluton, the zone is only 1–3 kilometers wide. The GSSZ at George Sound is split into at least four main branches as evidenced by the distribution of deformed fabrics throughout the fjord. These branches are $\leq$1 km wide and separated by zones of relatively undeformed rocks of the eastern McKerr Intrusives. The westernmost GSSZ branch is perhaps the least studied, and its continuation to the south is based on previously reported foliation measurements (Turnbull et al. 2010). This branch may merge or be cut by the Caswell thrust zone to the south at

Caswell Sound as suggested by Klepeis and Clarke (2003). Whether or not it continues to the northeast is unknown. We infer that the other branches at George Sound coalesce to the north and south into the observed single strands of the GSSZ at Bligh Sound and along the margin of the Misty Pluton.

Within this first-order mapping of deformed fabrics, we divide the GSSZ into two domains defined by relatively low-strain and high-strain fabrics. We correlate the highest strain fabrics from each field area: the oblate fabrics from Bligh Sound, the fabrics in the Anchorage Cove complex and mylonites in the Expedition Pluton at George Sound, the mylonite at Mary Peaks, and the subvertical fabrics in the Misty Pluton at Myth Tarn (Fig. 4.1). These high-strain zones are then bordered by the lower-strain fabrics observed at each field area: the prolate fabrics from Bligh Sound, the deformed McKerr Intrusives at George Sound, and the variable fabrics in the Misty Pluton from Mary Peaks to Cozette Burn. A second high-strain strand in the Misty Pluton is inferred to the west of the one observed at Myth Tarn because of reported subvertical fabrics on the Fiordland QMAP (Turnbull et al. 2010). The existence of this zone, however, is speculative without additional geologic data.

We interpret the high-strain fabrics to have accumulated the most finite strain, and generally represent the localization of strain into narrower zones. It is important to note that these correlations are not necessarily temporal. For example, high-strain zones may have localized in the Worsley Pluton prior to those in the Misty Pluton because the former was emplaced prior to the development of the GSSZ. Despite this, we correlate these fabrics because they represent a similar process of localizing strain into narrow zones within the GSSZ. These localization processes are discussed further in the following sections. Correlations of high-strain fabrics are based on 4 criteria: (1) steep, N–S-striking foliations, (2) amphibolite-facies mineral assemblages, (3) kinematic indicators exhibiting a

Field Area	GSSZ Fabrics		Factors controlling strain localization
	Low strain	High strain	
Bligh Sound	prolate Worsley Pluton	northern and southern oblate	metamorphic reactions, fluids
George Sound	McKerr Intrusives and Expedition Pluton fabrics	Ancorage Cove complex, Expedition mylonites	lithologic contacts; distribution of weak lithologies
Mary Peaks	igneous + tectonic Misty Pluton fabrics?	Large Granite mylonite	eastern contact of Misty Pluton (lithologic boundary)?
Myth Tarn	Misty Pluton facies one and facies two	steeply-dipping facies two	
Coronation Saddle/ Cozette Burn	Misty Pluton facies one	steeply dipping facies one	

Figure 4.1: Summary of fabric correlations along the strike of the George Sound shear zone.

component of sinistral motion, and (4) apparent continuity between field areas (i.e., intervening QMAP foliation measurements suggest that parallel fabrics are present between field areas). A summary of how fabrics between each field area are correlated is presented in figure 4.1.

Structural measurements, primarily the orientation of foliation, provide an indication of the three-dimensional geometry of the GSSZ. These data were used to construct the cross sections presented in chapter 3 and allow us to interpret the vertical component of GSSZ architecture. Additionally, because the McKerr Intrusives at George Sound were metamorphosed at shallower depths in the crust than the surrounding Misty and Worsley Plutons (ca. 0.86 GPa at George Sound versus >1.2 GPa for the Misty and Worsley Plutons), we can observe parts of the GSSZ at both middle- and lower-crustal levels (Anderson et al. 2019; Allibone et al. 2009b and references therein). A summary stereonet presenting the average orientation of the highest-strain fabrics at each field area is presented in figure 4.2.

Except in parts of the Misty Pluton, both high- and low-strain fabrics in the GSSZ are commonly steeply-dipping to subvertical. This is true in both lower crustal sections in the Misty and Worsley Plutons, and in the middle crustal section exposed at George Sound. The presence of steep fabrics in both the lower and middle crustal exposures of the GSSZ suggests that this shear zone may define a vertical crustal boundary, and is consistent with being a transpressional structure. It is possible this may have extended into fault zones in the upper crust.

Low-strain fabrics in the Misty Pluton have variable orientations, often contain relict magmatic textures (e.g., 3.27, 3.41b), and in places appear deflected into higher strain zones. The southernmost exposure of the GSSZ near Cozette Burn features a SW-striking foliation that is significantly shallower than observed elsewhere. Two possibilities or a combination thereof are a likely explanation for

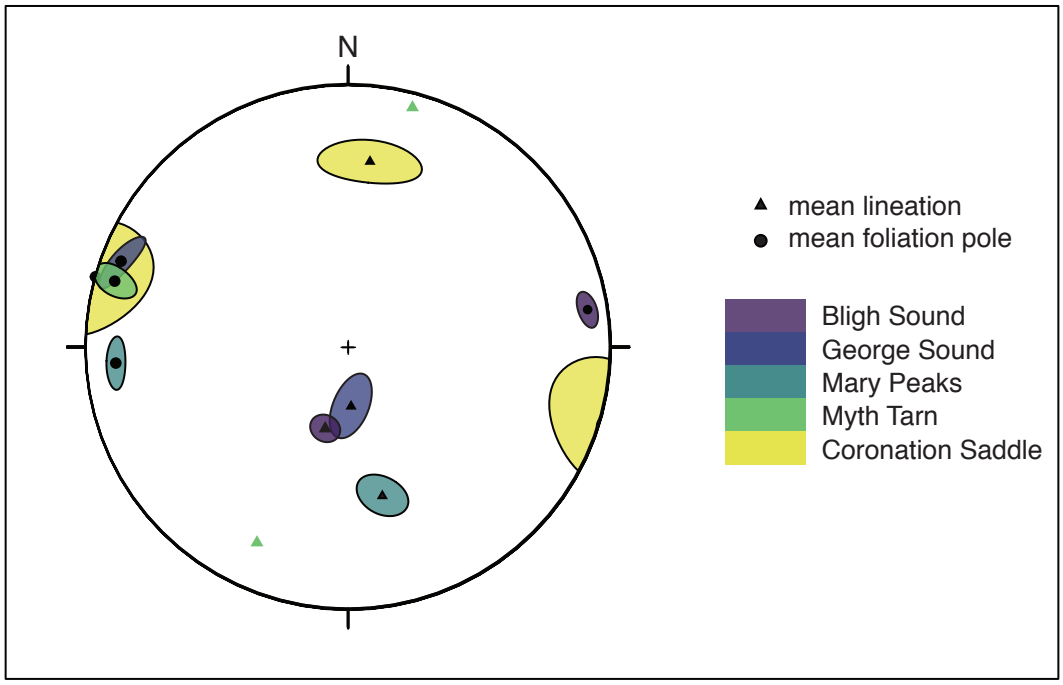

Figure 4.2: Stereonet summary of the orientation of average foliation and lineation directions and associated 95% confidence intervals from the highest-strain fabrics in each field area. No average lineation direction is reported for Myth Tarn and instead the two lineations directions from the high-strain fabrics there are plotted. This plot emphasizes the shallowing of lineation directions from northern field areas to southern ones.

this: 1) GSSZ fabrics in this area are relatively low strain, and low-strain fabrics at Coronation Saddle and Myth Tarn also exhibit a variable and shallow foliation, and/or 2) because these structural measurements come from an area bounded by reverse faults, movement on these may have rotated these fabrics relative to the rest of the GSSZ. Because of the possibility of the GSSZ fabrics having been reoriented, I do not consider the shallow foliation at Cozette Burn to represent a significant change in the architecture of the GSSZ.

Lineation directions within the GSSZ are much more variable than foliation, with mineral lineations plunging 60–70° S at Bligh and George Sound and 0–30° to the S and NNE at field areas along the Misty Pluton margin (Fig. 4.2). Lineations are an expression of the finite strain accumulated in a shear zone and their direction relates to the flow geometry of a shear zone and the amount of accumulated finite strain (e.g., Fossen and Tikoff, 1983). Variations in lineation direction therefore may represent variations in the boundary conditions of the shear zone, such as changes in plate convergence directions, or in the amount of finite strain accumulated. In the following section, I will explore potential explanations for the along-strike variability of lineation directions in the GSSZ.

4.2 Deformation processes in the George Sound shear zone

Throughout the GSSZ, near vertical foliations that formed at upper amphibolite facies cut across relatively undeformed igneous host rock of the Worsley Pluton, eastern McKerr Intrusives, Expedition Pluton, Large Granite, and Misty Pluton. However, the variety of rocks deformed in the GSSZ and the variable signatures of magmatic and metamorphic processes along its length suggest that the development

of the GSSZ may have been mediated by several different deformation processes.

Similarities in how the rocks deformed along the entire length of the GSSZ are also evident, including common microstructures observed at each field area. As I will summarize below, metamorphic and microstructural signatures suggest that rocks of the GSSZ deformed within a similar range of temperatures conditions. In dioritic and metasedimentary rocks throughout the GSSZ, mineral assemblages indicate amphibolite facies metamorphism. At Bligh Sound, syn-kinematic metamorphic textures indicate that metamorphism and deformation occurred simultaneously, but other field areas lack clear evidence for syn-kinematic metamorphic mineral growth.

Deformed hornblende aggregates in the Misty Pluton indicate the breakdown of pyroxene at amphibolite facies. The intergrowths of hornblende and quartz observed in the Misty Pluton at Myth Tarn and the southern Misty margin field areas are indicative of the replacement of pyroxene by quartz and hornblende. The relict pyroxene at the center of a hornblende and quartz intergrowth in sample 15AB72 (Fig. 3.41d), and similar textures observed in other plutons (e.g., Beach 1974; Beard et al., 2005) provides strong evidence for the hornblende and quartz aggregates observed in the Misty Pluton at Cozette Burn, Coronation Saddle, and the facies 1 fabrics at Myth Tarn being derived from the breakdown of pyroxene.

Microstructurally, GSSZ rocks also exhibit evidence of deformation via micro-mechanisms that are characteristic of high temperature deformation. Although not always the dominant deforming minerals (as in the southern oblate fabrics at Bligh Sound where biotite shear bands are ubiquitous), where present, both quartz and feldspar consistently show microstructural evidence for dynamic recrystallization (Moyer 2019). Most indicative of high-temperature deformation are feldspar grain boundary textures which suggest the feldspar deformed via grain boundary migration at most field areas. Some authors have presented evidence of

grain boundary migration textures in feldspar developing at temperatures around 1000°C (Lafrance et al. 1996), but others have shown that the deformation mechanisms of feldspars are sensitive to the presence of fluids and varying strain rates, and plagioclase GBM and subgrain rotation recrystallization have been reported in rocks deformed below 670°C (Tullis and Yund 1991; Rosenberg and Stünitz 2003). They suggest that this is may be the result of the presence of melt or fluids during deformation, which can enhance dynamic recrystallization (Dell'angelo and Tullis 1988). In quartz, subgrain rotation recrystallization has been interpreted to be dominant at temperatures in the range 400–500°C, with GBM dominant at higher temperatures and chessboard subgrains, such as those in the Misty Pluton and Large Granite at Mary Peaks, developing around 650°C (Stipp et al. 2002). Quartz ribbons, such as those in the mylonites of the Expedition Pluton, have been observed in rocks deformed at 680–750°C (Hippertt et al. 2001). It is therefore clear that both low- and high-strain fabrics in the GSSZ likely developed over a range of temperatures consistent with amphibolite facies conditions.

Despite similar temperature conditions along the GSSZ, variations in the geometry of fabrics and in how deformation was distributed through heterogeneous sections of the crust are evident. Below, I discuss how strain partitioning may have influenced the geometry of fabrics and how different strain localization processes may have narrowed the GSSZ at each field area.

4.2.1 Strain partitioning

As previously mentioned, lineation directions within the GSSZ vary significantly, shallowing from a 70° S plunge at Bligh Sound to 30° at Coronation Saddle, with a shift occurring between George Sound and Mary Peaks (Fig. 4.2). Varying lineation directions must indicate changes in the flow geometry of the GSSZ, and the geologic

context of the GSSZ may provide some indication of the cause of this change.

The shift in lineation plunges from steep to shallow correlates with the presence of adjacent structures. The southern extent of the GSSZ is also known to be bordered by several contractional structures that were also active during the Early Cretaceous, including the Caswell Sound fold thrust belt (Dazcko et al. 2002), the South Adams Burn thrust, and the Te Au Saddle thrust (Blatchford 2016). Figure 4.3 shows the position of these contractional structures relative to the George Sound shear zone. The presence of structures accommodating both contractional and transcurrent motion within the crust is an expression of the obliquely convergent environment in which the Fiordland arc was situated in the Early Cretaceous. To the north, at Bligh Sound, the pure and simple shear components of these motions combine in a triclinic transpressional system (Moyer 2019). The transpressional nature of the GSSZ at Bligh Sound accounts for the steep and locally variable lineations that are not directed along-strike nor down-dip, as is expected in monoclinic simple shear or transpressional shear zones (e.g., Lin et al. 1998).

Along the margin of the Misty Pluton, however, we lack evidence for transpressional flow in the GSSZ, and the shallow to subhorizontal lineations are not inconsistent with a shear zone dominated by monoclinic simple shear. The presence of adjacent contractional structures further suggests that the pure and simple shear components of deformation may be partitioned between contractional and transcurrent structures—i.e., the GSSZ. Whereas at Bligh Sound, pure and simple shear components were accommodated almost entirely within the GSSZ, to the south of George Sound, the Caswell Sound fold thrust belt, South Adams Burn thrust, and Te Au Saddle thrust may have accommodated the pure-shear component of deformation while the GSSZ accommodated obliquely sinistral simple shearing.

Variations in lineation direction along the length of the GSSZ may therefore be

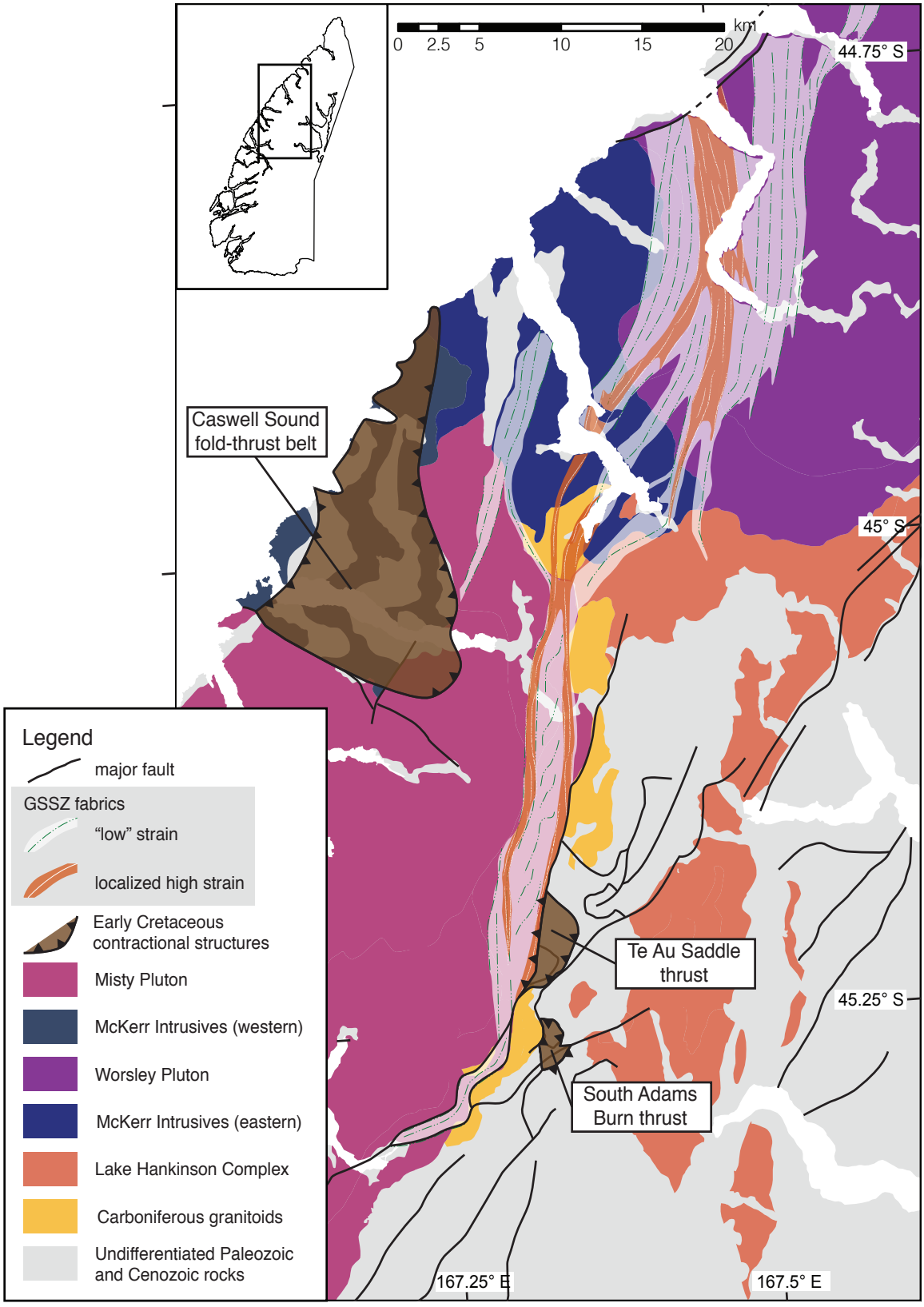
km
0 2.5 5 10 15 20
44.75° S
45° S
45.25° S
167.25° E
167.5° E
Caswell Sound fold-thrust belt
Te Au Saddle thrust
South Adams Burn thrust
Legend
major fault
GSSZ fabrics
"low" strain
localized high strain
Early Cretaceous contractional structures
Misty Pluton
McKerr Intrusives (western)
Worsley Pluton
McKerr Intrusives (eastern)
Lake Hankinson Complex
Carboniferous granitoids
Undifferentiated Paleozoic and Cenozoic rocks

Figure 4.3: Simplified geologic map of western Fiordland showing the extent of the GSSZ and adjacent contractional structures that were also active during the Early Cretaceous. Shaded brown regions indicate the extent of folds and thrusts that accommodated contraction perpendicular to the axis of the Fiordland magmatic arc (Daczko et al. 2002; Blatchford 2016).

the result of strain changes in how pure and simple shear are partitioned within the lower and middle crust. Although the entire section of the crust here appears to have evolved in a transpressional environment, contractional and transcurrent motion are coupled in a transpressional shear zone at Bligh Sound, while to the south strain may be partitioned between several different structures accommodating different amounts of pure and simple shear.

4.2.2 Strain localization

Within the large-scale architecture of the shear zone discussed above, narrow (≤ 1 km) zones of high-strain fabrics represent the localization of deformation within the George Sound shear zone. Just as the geometry of shear fabrics varies along strike, so too do the apparent processes behind strain localization. In this section I discuss two potential factors that likely affected the localization of strain in the GSSZ, and therefore influenced its large-scale form. We infer that both preexisting weak zones and dynamic weakening processes affected strain localization in the GSSZ. I will first address the dynamic process of metamorphism, which may alter the bulk strength of body of rock over time and has been recognized as an influential processes in other shear zones (e.g., Getsinger et al. 2013; Stunitz and Tullis 2001; Condit and Mahan 2018). Finally, I will discuss the influence of preexisting weak zones, both in terms of lithologic heterogeneity and the presence of lithologic boundaries. In both cases, preexisting or newly developed zones of rheologically

weak rocks preferentially accommodated strain in the GSSZ.

Metamorphism

At Bligh Sound, the spatial correlation of structural patterns and metamorphic characteristics suggests a link between deformation and metamorphic processes. Unlike elsewhere in the GSSZ, strain localization in the exposure at Bligh Sound and the formation of the narrower oblate fabric domains may be related to the metamorphic growth of hornblende, biotite, and quartz.

Within the broader domain of prolate fabrics, the northern and southern oblate fabrics define a zone of relatively high strain. The greater amounts of strain accumulated in the oblate fabrics—particularly the southern oblate fabric—compared to the prolate fabrics is evidenced by ubiquitous hornblende and biotite shear bands forming a well-defined foliation. Microstructures indicate that hornblende, biotite, and quartz grew during deformation. These minerals, especially biotite and quartz, are rheologically weak and may easily deform and develop interconnected weak layers that are efficient at accommodating displacements (Gardner et al. 2017; Holyoke and Tullis 2006). This strain localization at the microscale could then be mirrored at the map scale as the bulk rheology of the rocks is weakened by the formation of networks of weak minerals, softening the rocks in what are now the oblate zones and localizing greater strains.

The metamorphic reactions necessary to produce hornblende, biotite, and quartz require the presence of water (Beach 1980; Williams et al. 2000), and thus indicate that the GSSZ served as a conduit for fluids through the crust. Although we are not able to discern whether deformation first facilitated fluid flow and metamorphism or whether preexisting channels for fluid flow facilitated reaction softening, once reaction softening initiated, it likely promoted both further localization of both

strain and fluid flow, creating a positive feedback.

A curiosity of the fabric facies at Bligh Sound is the along-strike difference between the northern and southern oblate fabrics, and the geometric differences between them. It appears that, even within the same pluton, the degree of strain localization may vary along strike in a shear zone. When that strain localizes—at least in a transpressional system like at Bligh Sound—the resulting fabrics may have a different orientation than adjacent lower-strain fabrics, which suggests the existence of discontinuous "steps" in a progressive deformation history (e.g., Fossen et al. 2018).

Preexisting heterogeneities

Beyond Bligh Sound, the George Sound shear zone crosscuts sections of the crust that contain multiple rock types and deformation is heterogeneously distributed, rather than confined to a single, continuous strand of shear fabrics. This is most apparent at George Sound where the GSSZ is separated into branches that bound relatively undeformed sections of rock. In this case, the location of metasedimentary and granitic xenoliths within the eastern McKerr Intrusives correlate with the location of high-strain zones. The GSSZ fabrics to the south of George Sound, however, again define more of a single strand of deformed fabrics, which correlate with the eastern margin of the Misty Pluton juxtaposed against metasedimentary and igneous host rocks to the east.

At George Sound, the metasedimentary and granitic xenoliths would have been natural rocks in which to localize deformation considering their greater proportion of quartz, feldspar, and micas that would makes the rocks relatively weaker than the surrounding dioritic material. Indeed, we observe the heterogeneous distribution of strain on the outcrop scale at Anchorage Cove where amphibolite layers appear less

deformed at the microscale than metasedimentary units (Fig. 3.18). This is then mirrored at the map scale where the most commonly undeformed or weakly deformed rock type is the dioritic eastern McKerr Intrusives. The branching architecture of the GSSZ at George Sound may therefore be the result of preferential strain localization in preexisting, rheologically weak rocks. The heterogeneous distribution of weak rocks in the crust has also been cited as an explanation for the complex, anastomosing nature of other shear zones like the Borborema shear zone system of northeastern Brazil (Vauchez et al. 1995; Tommasi et al. 1995).

The eastern margin of the Misty Pluton on the other hand would have represented a rheological boundary between hot, recently emplaced diorite to the west and potentially cooler host rock to the east. In some places, as at Mary Peaks, weak host rock appears to have localized some deformation, but it is also possible that deformation of the Misty Pluton there has been obscured by subsequent magmatic activity. Thermal gradients are also inferred to be important factors in localizing strike-slip fault systems at depth, so the juxtaposition of the hot Misty Pluton and cooler host rocks may have also been a reason for localizing deformation along its margin (Cao and Neubauer 2016). Contemporaneous magmatism has also been proposed as a focusing mechanism for deformation, helping to weaken parts of the crust and allowing strain to localize (e.g., Dewey et al. 1998; Brown and Solar 1998; Kruckenberg et al. 2013). Because of the emplacement of the Misty Pluton during the same time period as deformation in the GSSZ, it is likely that magmatism played a roll in localizing strain, or was itself influenced by the localization of the GSSZ. However, because tectonic fabrics may overprint previous magmatic textures and vice versa, earlier indicators of magma-deformation interactions would not remain. It is therefore difficult to discern the extent to which magmatism helped localize strain in the GSSZ.

Whereas dynamic weakening of parts of the Worsley Pluton via metamorphic reactions appears to have been involved in the localization of high-strain fabrics at Bligh Sound, preexisting lithologic heterogeneities were likely an important control on the localization of strain at George Sound and farther south. The dominance of these different processes within the same shear zone demonstrates how the evolution of a single shear zone system may vary along strike within the lower crust.

Chapter 5

Conclusions

I present structural, petrologic, and microstructural observations from two new field areas and three previously studies sites in western Fiordland. After analyzing the geometry, kinematics, and relative strain intensity of fabrics at each site, I correlate fabrics between each field area to define the architecture of the George Sound shear zone. The picture that results is of a ~50 km-long, N–S-striking structure recording oblique sinistral shearing (dominantly west side down-to-the-SW) in a transpressional environment at upper amphibolite facies conditions during the Early Cretaceous. Within the GSSZ, the branching segments and thickness variations from <1 km to ~10 km, as well as the suite of fabrics of different strain intensities all likely resulted from differences in strain localization and partitioning in the compositionally heterogeneous lower crust of the Fiordland magmatic arc. Variations in fabric orientations—particularly the shallowing of lineation directions along the strike of the GSSZ—may be explained by variations in strain partitioning in the lower crust of the Fiordland magmatic arc.

The GSSZ appears as a single zone in relatively homogeneous plutons—the Misty and Worsley Plutons—but branches into several strands where strain was

likely localized by map-scale lithologic contacts and the presence of large xenoliths of weak metasedimentary and granitic within the eastern McKerr Intrusives. Within these zones, strain was further localized as the GSSZ evolved. Metamorphic reactions likely also helped strain to localize within sections of the Worsley Pluton, where the products of metamorphic hydration reaction are associated with high-strain fabrics. To the south, however, lithologic or temperatures contrasts localized deformation to the eastern margin of the Misty Pluton.

The shallowing of lineations from 70° S at George Sound to 0–30° N/S along the Misty Pluton margin may be explained by the partitioning of strain among adjacent contractional structures along the Misty Pluton margin. Whereas pure and simple shear appear coupled in the triclinic transpressional system at Bligh Sound, the partitioning of the pure shear component onto nearby structures—like the Caswell Sound fold thrust belt, the South Adams Burn thrust, and the Te Au Saddle thrust—along the Misty Pluton margin would render the southern GSSZ a transcurrent structure primarily accommodating simple shear. Such a kinematic style provides an explanation for the development of gently-plunging lineations.

The variability in geometry and inferred strain localization processes that occur along the strike of the George Sound shear zone system underscore the complexity of deformation in the lower crust. This also emphasizes the number of factors—metamorphic, magmatic, lithologic, structural—that must be considered in order to evaluate the various possible controls on shear zone architecture and evolution in the lower crust. In the future, petrochronologic studies and more detailed thermobarometry on rocks from the GSSZ would help to better understand the relationship between the various fabrics observed at each field area by comparing their relative timing and the P-T conditions in which they formed. Geochemical work to better understand the impacts and compositions of fluids in the GSSZ

would also help to determine the possible metamorphic reactions that occurred, and may better constrain the sources and pathways of fluids in continental magmatic arc settings. The results of this work also suggest the kinematic style of a shear zone may not be consistent along its strike—potentially as a result of variations in strain partitioning among other structures. But, how this transition occurs and what in entails for the translation of deformation to other levels of the crust is unclear, and its effects on the behavior of lithosphere-scale boundaries has not been explored.

Bibliography

Allibone, A. H., R. Jongens, J. M. Scott, A. J. Tulloch, I. M. Turnbull, A. F. Cooper, N. G. Powell, E. B. Ladley, R. P. King, and M. S. Rattenbury (2009a). *Plutonic rocks of the Median Batholith in eastern and central Fiordland , New Zealand : Field relations , geochemistry , correlation , and nomenclature.* Vol. 52. 101-148. DOI: 10.1080/00288300909509882.

Allibone, A. H., R. Jongens, I. M. Turnbull, L. A. Milan N, R. Daczko, M. C. De Paoli, and A. J. Tulloch (2009b). "Plutonic rocks of western Fiordland, New Zealand: Field relations, geochemistry, correlation, and nomenclature". In: *New Zealand Journal of Geology and Geophysics* 52.4, pp. 379–415. DOI: 10.1080/00288306.2009.9518465.

Anderson, Ian, Harold Stowell, Joshua J. Schwartz, K. A. Klepeis, Elizabeth M. Bollen, and Elena A. Miranda (2019). "Pressure, temperature, and timing of magma intrusion and metamorphism, George Sound, New Zealand". In: Geological Society of America Abstracts with Programs. Vol. 51. DOI: doi:10.1130/abs/2019AM-337312.

Beach, A. (June 1974). "Amphibolitization of Scourian granulites". In: *Scottish Journal of Geology* 10.1, pp. 35–43. DOI: 10.1144/sjg10010035.

— (Jan. 1, 1980). "Retrogressive metamorphic processes in shear zones with special reference to the Lewisian complex". In: *Journal of Structural Geology*. Shear zones in rocks 2.1, pp. 257–263. DOI: 10.1016/0191-8141(80)90058-9.

Betka, Paul M. and Keith A. Klepeis (Sept. 2013). "Three-stage evolution of lower crustal gneiss domes at Breaksea Entrance, Fiordland, New Zealand: GNEISS DOME EVOLUTION IN FIORDLAND". In: *Tectonics* 32.5, pp. 1084–1106. DOI: 10.1002/tect.20068.

Blatchford, Hannah (2016). "The structural evolution of a portion of the Median Batholith and its host rock in central Fiordland, New Zealand: Examples of partitioned transpression and structural reactivation". MS. University of Vermont.

Bradshaw, J.Y. (1990). "Geology of crystalline rocks of northern Fiordland: details of the granulite facies Western Fiordland Orthogneiss and associated rock units". In: *New Zealand Journal of Geology and Geophysics* 33, pp. 465–484.

Bradshaw, J.Y. and D. L. Kimbrough (1991). “Mid Paleozoic age of granitoids in enclaves within Early Cretaceous granulites, Fiordland, southwest New Zealand”. In: *New Zealand Journal of Geology and Geophysics* 34, pp. 455–470.

Brandon, Mark T. (Oct. 1, 1995). “Analysis of geologic strain data in strain-magnitude space”. In: *Journal of Structural Geology* 17.10, pp. 1375–1385. DOI: 10.1016/0191-8141(95)00032-9.

Brodie, K. H. and E. H. Rutter (1985). “On the Relationship between Deformation and Metamorphism, with Special Reference to the Behavior of Basic Rocks”. In: *Metamorphic Reactions: Kinetics, Textures, and Deformation*. Ed. by Alan Bruce Thompson and David C. Rubie. Advances in Physical Geochemistry. New York, NY: Springer, pp. 138–179. DOI: 10.1007/978-1-4612-5066-1_6.

Brown, Michael and Gary S. Solar (Feb. 1, 1998). “Shear-zone systems and melts: feedback relations and self-organization in orogenic belts”. In: *Journal of Structural Geology*. Structures and Properties of High Strain Zones in Rocks 20.2, pp. 211–227. DOI: 10.1016/S0191-8141(97)00068-0.

Bürgmann, Roland and Georg Dresen (2008). “Rheology of the Lower Crust and Upper Mantle : Evidence from Rock Mechanics , Geodesy , and Field Observations”. In: *Annual Review of Earth and Planetary Sciences* 36, pp. 531–567. DOI: 10.1146/annurev.earth.36.031207.124326.

Buritica, Luisa F., Joshua J. Schwartz, Keith A. Klepeis, Elena A. Miranda, Andy J. Tulloch, Matthew A. Coble, and Andrew R. C. Kylander-Clark (Oct. 1, 2019). “Temporal and spatial variations in magmatism and transpression in a Cretaceous arc, Median Batholith, Fiordland, New Zealand”. In: *Lithosphere* 11.5. Publisher: GeoScienceWorld, pp. 652–682. DOI: 10.1130/L1073.1.

Cao, Shuyun and Franz Neubauer (Nov. 1, 2016). “Deep crustal expressions of exhumed strike-slip fault systems: Shear zone initiation on rheological boundaries”. In: *Earth-Science Reviews* 162, pp. 155–176. DOI: 10.1016/j.earscirev.2016.09.010.

Carreras, J. (2001). “Zooming on Northern Cap de Creus shear zones”. In: *Journal of Structural Geology* 23.9, pp. 1457–1486. DOI: 10.1016/S0191-8141(01)00011-6.

Clarke, G. L., K. A. Klepeis, and N. R. Daczko (2000). “Cretaceous high-P granulites at Milford Sound, New Zealand: metamorphic history and emplacement in a convergent margin setting”. In: *Journal of Metamorphic Geology* 18.4. _eprint: https://onlinelibrary.wiley.com/doi/pdf/10.1046/j.1525-1314.2000.00259.x, pp. 359–374. DOI: 10.1046/j.1525-1314.2000.00259.x.

Condit, Cailey B. and Kevin H. Mahan (2018). “Fracturing , fluid flow and shear zone development : Relationships between chemical and mechanical processes in Proterozoic mafic dykes from southwestern Montana , USA”. In: *Journal of Metamorphic Geology* 36, pp. 195–223. DOI: 10.1111/jmg.12289.

Daczko, Nathan R., Keith A. Klepeis, and Geoffrey L. Clarke (2002). "Thermomechanical evolution of the crust during convergence and deep crustal pluton emplacement in the western province of Fiordland, New Zealand". In: *Tectonics* 21.4, pp. 1–18. DOI: 10.1029/2001TC001282.

— (Apr. 1, 2001). "Evidence of Early Cretaceous collisional-style orogenesis in northern Fiordland, New Zealand and its effects on the evolution of the lower crust". In: *Journal of Structural Geology* 23.4, pp. 693–713. DOI: 10.1016/S0191-8141(00)00130-9.

Davey, F. J. and E. G. C. Smith (Jan. 1, 1983). "The tectonic setting of the Fiordland region, south-west New Zealand". In: *Geophysical Journal International* 72.1, pp. 23–38. DOI: 10.1111/j.1365-246X.1983.tb02802.x.

Davis, Joshua R (2019). *The geologyGeometry library for R*. Version 2019/08/08.

Davis, Joshua R. and Sarah J. Titus (2017). "Modern methods of analysis for three-dimensional orientational data". In: *Journal of Structural Geology* 96, pp. 65–89. DOI: 10.1016/j.jsg.2017.01.002.

Decker, M., J. J. Schwartz, H. H. Stowell, K. A. Klepeis, A. J. Tulloch, K. Kitajima, J. W. Valley, and A. R. C. Kylander-Clark (2017). "Slab-Triggered Arc Flare-up in the cretaceous median batholith and the growth of lower arc crust, Fiordland, New Zealand". In: *Journal of Petrology* 58.6, pp. 1145–1171. DOI: 10.1093/petrology/egx049.

Deer, W. A., Jack Zussman, R. A. Howie, Howie-R. A, Zussman- J, W.A Deer, R.A Howie, and J Zussman (1962). *Rock-forming minerals*. Type: Book; Book/Illustrated. London : Longmans.

Dell'angelo, L. N. and J. Tullis (1988). "Experimental deformation of partially melted granitic aggregates". In: *Journal of Metamorphic Geology* 6.4. _eprint: https://onlinelibrary.wiley.com/doi/pdf/10.1111/j.1525-1314.1988.tb00436.x, pp. 495–515. DOI: 10.1111/j.1525-1314.1988.tb00436.x.

Dewey, J. F., R. E. Holdsworth, and R. A. Strachan (1998). "Transpression and transtension zones". In: *Geological Society, London, Special Publications* 135.1, pp. 1–14. DOI: 10.1144/GSL.SP.1998.135.01.01.

Ducea, Mihai N., Jason B. Saleeby, and George Bergantz (2015). "The Architecture, Chemistry, and Evolution of Continental Magmatic Arcs". In: *Annual Review of Earth and Planetary Sciences* 43.1, pp. 299–331. DOI: 10.1146/annurev-earth-060614-105049.

Dumond, Gregory, Michael L. Williams, and Sean P. Regan (May 30, 2018). "The Athabasca Granulite Terrane and Evidence for Dynamic Behavior of Lower Continental Crust". In: *Annual Review of Earth and Planetary Sciences* 46.1, pp. 353–386. DOI: 10.1146/annurev-earth-063016-020625.

Fossen, Haakon, Carolina Cavalcante, Roberto Pinheiro, and Carlos Archanjo (May 1, 2018). "Deformation – Progressive or multiphase?" In: *Journal of Structural Geology*. DOI: 10.1016/j.jsg.2018.05.006.

Fossen, Haakon and Geane Carolina G. Cavalcante (Aug. 2017). "Shear zones – A review". In: *Earth-Science Reviews* 171, pp. 434–455. DOI: 10.1016/j.earscirev.2017.05.002.

Gardner, Robyn, Sandra Piazolo, Lynn Evans, and Nathan Daczko (Apr. 1, 2017). "Patterns of strain localization in heterogeneous, polycrystalline rocks – a numerical perspective". In: *Earth and Planetary Science Letters* 463, pp. 253–265. DOI: 10.1016/j.epsl.2017.01.039.

Geology of the Fiordland Area. Institute of Geological & Nuclear Sciences 1: 250,000 Geological Map 17 (n.d.). In collab. with I. M. Turnbull, A. Allibone, and R. Jongens. Lower Hutt, GNS Science.

Gerbi, Christopher, Scott E. Johnson, Deborah Shulman, and Keith Klepeis (2016). "Influence of microscale weak zones on bulk strength". In: *Geochemistry, Geophysics, Geosystems* 17.10. _eprint: https://agupubs.onlinelibrary.wiley.com/doi/pdf/10.1002/2016GC006551, pp. 4064–4077. DOI: 10.1002/2016GC006551.

Getsinger, A. J., G. Hirth, H. Stünitz, and E. T. Goergen (2013). "Influence of water on rheology and strain localization in the lower continental crust". In: *Geochemistry, Geophysics, Geosystems* 14.7, pp. 2247–2264. DOI: 10.1002/ggge.20148.

Gibson, G M, I McDougali, and T R Ireland (1988). "Age constraints on metamorphism and the development of a metamorphic core complex in Fiordland, southern New Zealand". In: p. 4.

Goncalves, P., E. Oliot, D. Marquer, and J. A. D. Connolly (2012). "Role of chemical processes on shear zone formation: An example from the grimsel metagranodiorite (Aar massif, Central Alps)". In: *Journal of Metamorphic Geology* 30.7, pp. 703–722. DOI: 10.1111/j.1525-1314.2012.00991.x.

Handy, Mark R. (June 10, 1989). "Deformation regimes and the rheological evolution of fault zones in the lithosphere: the effects of pressure, temperature, grainsize and time". In: *Tectonophysics* 163.1, pp. 119–152. DOI: 10.1016/0040-1951(89)90122-4.

Hanmer, Simon (Feb. 1, 1997). "Shear zone reactivation at granulite facies: the importance of plutons in the localization of viscous flow". In: *Journal of the Geological Society* 154.1. Publisher: GeoScienceWorld, pp. 111–116. DOI: 10.1144/gsjgs.154.1.0111.

Hippertt, J, A Rocha, C Lana, M Egydio-Silva, and T Takeshita (Jan. 1, 2001). "Quartz plastic segregation and ribbon development in high-grade striped gneisses". In: *Journal of Structural Geology* 23.1, pp. 67–80. DOI: 10.1016/S0191-8141(00)00129-2.

Hollis, J. A., G. L. Clarke, K. A. Klepeis, N. R. Daczko, and T. R. Ireland (2004). "The regional significance of Cretaceous magmatism and metamorphism in Fiordland, New Zealand, from U–Pb zircon geochronology". In: *Journal of Metamorphic Geology* 22.7. _eprint:

https://onlinelibrary.wiley.com/doi/pdf/10.1111/j.1525-1314.2004.00537.x, pp. 607–627. DOI: 10.1111/j.1525-1314.2004.00537.x.

Holyoke, C. W. and J. Tullis (2006a). "The interaction between reaction and deformation: an experimental study using a biotite + plagioclase + quartz gneiss". In: *Journal of Metamorphic Geology* 24.8. _eprint: https://onlinelibrary.wiley.com/doi/pdf/10.1111/j.1525-1314.2006.00666.x, pp. 743–762. DOI: 10.1111/j.1525-1314.2006.00666.x.

Holyoke, Caleb and Jan Tullis (Apr. 1, 2006b). "Mechanisms of weak phase interconnection and the effects of phase strength contrast on fabric development". In: *Journal of Structural Geology - J STRUCT GEOL* 28, pp. 621–640. DOI: 10.1016/j.jsg.2006.01.008.

Ireland, T. R. and G. M. Gibson (1998). "SHRIMP monazite and zircon geochronology of high-grade metamorphism in New Zealand". In: *Journal of Metamorphic Geology* 16.2. _eprint: https://onlinelibrary.wiley.com/doi/pdf/10.1111/j.1525-1314.1998.00112.x, pp. 149–167. DOI: 10.1111/j.1525-1314.1998.00112.x.

Jamtveit, Bjørn, Håkon Austrheim, and Andrew Putnis (2016). "Disequilibrium metamorphism of stressed lithosphere". In: *Earth-Science Reviews* 154, pp. 1–13. DOI: 10.1016/j.earscirev.2015.12.002.

King, Peter R. (Dec. 2000). "Tectonic reconstructions of New Zealand: 40 Ma to the Present". In: *New Zealand Journal of Geology and Geophysics* 43.4, pp. 611–638. DOI: 10.1080/00288306.2000.9514913.

Klepeis, Keith A. and Geoffrey L. Clarke (2004). "The evolution of an exposed mid-lower crustal attachment zone in Fiordland, New Zealand". In: *Geological Society, London, Special Publications* 227.1, pp. 197–229. DOI: 10.1144/GSL.SP.2004.227.01.11.

Klepeis, Keith A., Geoffrey L. Clarke, George Gehrels, and Jeff Vervoort (2004). "Processes controlling vertical coupling and decoupling between the upper and lower crust of orogens: Results from Fiordland, New Zealand". In: *Journal of Structural Geology* 26.4, pp. 765–791. DOI: 10.1016/j.jsg.2003.08.012.

Klepeis, Keith, Laura Webb, Hannah Blatchford, Joshua Schwartz, Richard Jongens, Rose Turnbull, and Harold Stowell (2019). "Deep Slab Collision during Miocene Subduction Causes Uplift along Crustal-Scale Reverse Faults in Fiordland, New Zealand". In: *GSA Today* 29.9, pp. 4–10. DOI: 10.1130/gsatg399a.1.

Kruckenberg, Seth C., Basil Tikoff, Virginia G. Toy, Julie Newman, and Laura I. Young (May 1, 2013). "Strain localization associated with channelized melt migration in upper mantle lithosphere: Insights from the Twin Sisters ultramafic complex, Washington, USA". In: *Journal of Structural Geology.* Deformation localization in rocks 50, pp. 133–147. DOI: 10.1016/j.jsg.2012.10.009.

Kula, Joseph, Andy Tulloch, Terry L. Spell, and Michael L. Wells (May 1, 2007). "Two-stage rifting of Zealandia-Australia-Antarctica: Evidence from 40Ar/39Ar

thermochronometry of the Sisters shear zone, Stewart Island, New Zealand". In: *Geology* 35.5. Publisher: GeoScienceWorld, pp. 411–414. DOI: 10.1130/G23432A.1.

Lafrance, B., Barbara E. John, and James S. Scoates (Jan. 24, 1996). "Syn-emplacement recrystallization and deformation microstructures in the Poe Mountain anorthosite, Wyoming". In: *Contributions to Mineralogy and Petrology* 122.4, pp. 431–440. DOI: 10.1007/s004100050139.

Lin, Shoufa, Dazhi Jiang, and Paul F. Williams (1998). "Transpression (or transtension) zones of triclinic symmetry: natural example and theoretical modelling". In: *Geological Society, London, Special Publications* 135.1, pp. 41–57. DOI: 10.1144/GSL.SP.1998.135.01.04.

Marcotte, Stephen B., Keith A. Klepeis, Geoffrey L. Clarke, George Gehrels, and Julie A. Hollis (2005). "Intra-arc transpression in the lower crust and its relationship to magmatism in a Mesozoic magmatic arc". In: *Tectonophysics* 407.3, pp. 135–163. DOI: 10.1016/j.tecto.2005.07.007.

Mardia, Kanti V. and Peter E. Jupp (Sept. 25, 2009). *Directional Statistics*. John Wiley & Sons. 453 pp.

Mortimer, N. (2004). "New Zealand's geological foundations". In: *Gondwana Research* 7.1, pp. 261–272. DOI: 10.1016/S1342-937X(05)70324-5.

Mortimer, N., A. J. Tulloch, R. N. Spark, N. W. Walker, E. Ladley, A. Allibone, and D. L. Kimbrough (1999). "Overview of the Median Batholith, New Zealand: A new interpretation of the geology of the Median Tectonic Zone and adjacent rocks". In: *Journal of African Earth Sciences* 29.1, pp. 257–268. DOI: 10.1016/S0899-5362(99)00095-0.

Mortimer, Nick (Dec. 2008). "Zealandia". In: *ASEG Extended Abstracts* 2008.1, pp. 1–4. DOI: 10.1071/ASEG2006ab119.

Mortimer, Nick, Hamish J. Campbell, Andy J. Tulloch, Peter R. King, Vaughan M. Stagpoole, Ray A. Wood, Mark S. Rattenbury, Rupert Sutherland, Chris J. Adams, Julien Collot, and Maria Seton (2017). "Zealandia: Earth's hidden Continent". In: *GSA Today* 27.3, pp. 27–35. DOI: 10.1130/GSATG321A.1.

Moyer, Griffin (2019). "Strain accommodation, metamorphic evolution, and 3D kinematics of transpressional flow within the lower crust of a Cretaceous magmatic arc in Fiordland, New Zealand". MS. University of Vermont.

Neves, S.P., A. Vauchez, and C.J. Archanjo (Sept. 1996). "Shear zone-controlled magma emplacement or magma-assisted nucleation of shear zones? Insights from northeast Brazil". In: *Tectonophysics* 262.1, pp. 349–364. DOI: 10.1016/0040-1951(96)00007-8.

NZ 8m Digital Elevation Model (2012) (Mar. 2, 2016).

Poirier, J. P. (Jan. 1, 1980). "Shear localization and shear instability in materials in the ductile field". In: *Journal of Structural Geology*. Shear zones in rocks 2.1, pp. 135–142. DOI: 10.1016/0191-8141(80)90043-7.

Ramezani, J. and A. J. Tulloch (2009). *TiMS u-Pb geochronology of southern and eastern Fiordland*.

Roberts, Nicolas M., Basil Tikoff, Joshua R. Davis, and Tor Stetson-Lee (2018). "The utility of statistical analysis in structural geology". In: *Journal of Structural Geology* (December 2017). DOI: 10.1016/j.jsg.2018.05.030.

Rosenberg, Claudio L. and Holger Stünitz (Mar. 2003). "Deformation and recrystallization of plagioclase along a temperature gradient: an example from the Bergell tonalite". In: *Journal of Structural Geology* 25.3, pp. 389–408. DOI: 10.1016/S0191-8141(02)00036-6.

Schwartz, Joshua J., Keith A. Klepeis, Joseph F. Sadorski, Harold H. Stowell, Andy J. Tulloch, and Matthew A. Coble (2017). "The tempo of continental arc construction in the Mesozoic Median Batholith, Fiordland, New Zealand". In: *Lithosphere* 9.3, pp. 343–365. DOI: 10.1130/L610.1.

Schwartz, Joshua J., Harold H. Stowell, Keith A. Klepeis, Andy J. Tulloch, Andrew R. C. Kylander-Clark, Bradley R. Hacker, and Matthew A. Coble (June 1, 2016). "Thermochronology of extensional orogenic collapse in the deep crust of Zealandia". In: *Geosphere* 12.3. Publisher: GeoScienceWorld, pp. 647–677. DOI: 10.1130/GES01232.1.

Scott, J. M. and A. F. Cooper (2006). "Early Cretaceous extensional exhumation of the lower crust of a magmatic arc: Evidence from the Mount Irene Shear Zone, Fiordland, New Zealand". In: *Tectonics* 25.3. _eprint: https://agupubs.onlinelibrary.wiley.com/doi/pdf/10.1029/2005TC001890. DOI: 10.1029/2005TC001890.

Scott, J. M., A. F. Cooper, J. M. Palin, A. J. Tulloch, J. Kula, R. Jongens, T. L. Spell, and N. J. Pearson (2009). "Tracking the influence of a continental margin on growth of a magmatic arc, Fiordland, New Zealand, using thermobarometry, thermochronology, and zircon U-Pb and Hf isotopes". In: *Tectonics* 28.6. _eprint: https://agupubs.onlinelibrary.wiley.com/doi/pdf/10.1029/2009TC002489. DOI: 10.1029/2009TC002489.

Stipp, Michael, Holger Stünitz, Renée Heilbronner, and Stefan M. Schmid (Dec. 1, 2002). "The eastern Tonale fault zone: a 'natural laboratory' for crystal plastic deformation of quartz over a temperature range from 250 to 700°C". In: *Journal of Structural Geology* 24.12, pp. 1861–1884. DOI: 10.1016/S0191-8141(02)00035-4.

Stowell, H., K. Odom Parker, M. Gatewood, A. Tulloch, and A. Koenig (2014). "Temporal links between pluton emplacement, garnet granulite metamorphism, partial melting and extensional collapse in the lower crust of a Cretaceous magmatic arc, Fiordland, New Zealand". In: *Journal of Metamorphic Geology* 32.2. _eprint: https://onlinelibrary.wiley.com/doi/pdf/10.1111/jmg.12064, pp. 151–175. DOI: 10.1111/jmg.12064.

Stünitz, Holger and Jan Tullis (May 1, 2001). "Weakening and strain localization produced by syn-deformational reaction of plagioclase". In: *International Journal of Earth Sciences* 90.1, pp. 136–148. DOI: 10.1007/s005310000148.

Sutherland, Rupert, Fred Davey, and John Beavan (Apr. 30, 2000). "Plate boundary deformation in South Island, New Zealand, is related to inherited lithospheric structure". In: *Earth and Planetary Science Letters* 177.3, pp. 141–151. DOI: 10.1016/S0012-821X(00)00043-1.

Teyssier, Christian and Basil Tikoff (1998). "Strike-slip partitioned transpression of the San Andreas fault system: a lithospheric-scale approach". In: *Geological Society, London, Special Publications* 135.1. Publisher: Geological Society of London _eprint: https://sp.lyellcollection.org/content/135/1/143.full.pdf, pp. 143–158. DOI: 10.1144/GSL.SP.1998.135.01.10.

Tommasi, Andréa, Alain Vauchez, and Bertrand Daudré (Nov. 10, 1995). "Initiation and propagation of shear zones in a heterogeneous continental lithosphere". In: *Journal of Geophysical Research: Solid Earth* 100 (B11), pp. 22083–22101. DOI: 10.1029/95JB02042.

Tullis, J., R. Yund, and J. Farver (Jan. 1, 1996). "Deformation-enhanced fluid distribution in feldspar aggregates and implications for ductile shear zones". In: *Geology* 24.1. Publisher: GeoScienceWorld, pp. 63–66. DOI: 10.1130/0091-7613(1996)024<0063:DEFDIF>2.3.CO;2.

Tullis, Jan and Richard A Yund (1991). "Diffusion creep in feldspar aggregates: experimental evidence". In: *Journal of Structural Geology* 13.9, pp. 987–1000. DOI: 10.1016/0191-8141(91)90051-J.

Tulloch, A. J., J. Ramezani, D. L. Kimbrough, K. Faure, and A. H. Allibone (Sept. 1, 2009). "U-Pb geochronology of mid-Paleozoic plutonism in western New Zealand: Implications for S-type granite generation and growth of the east Gondwana margin". In: *Geological Society of America Bulletin* 121, pp. 1236–1261. DOI: 10.1130/B26272.1.

Tulloch, Andrew and David Kimbrough (2003). "Paired plutonic belts in convergent margins and the development of high Sr/Y magmatism: Peninsular Ranges Batholith of Baja California and Median Batholith of New Zealand". In: *Special Paper of the Geological Society of America*. Vol. 374, pp. 275–295. DOI: 10.1130/0-8137-2374-4.275.

Vauchez, A., S. Neves, R. Caby, M. Corsini, M. Egydio-Silva, M. Arthaud, and V. Amaro (July 1995). "The Borborema shear zone system, NE Brazil". In: *Journal of South American Earth Sciences* 8.3, pp. 247–266. DOI: 10.1016/0895-9811(95)00012-5.

Vauchez, Alain, Andréa Tommasi, and David Mainprice (Aug. 2012). "Faults (shear zones) in the Earth's mantle". In: *Tectonophysics* 558-559, pp. 1–27. DOI: 10.1016/j.tecto.2012.06.006.

Vollmer, Frederick W. (June 1, 2018). "Automatic contouring of geologic fabric and finite strain data on the unit hyperboloid". In: *Computers & Geosciences* 115, pp. 134–142. DOI: 10.1016/j.cageo.2018.03.006.

Williams, M. L., G. Dumond, K. Mahan, S. Regan, and M. Holland (Nov. 1, 2014). "Garnet-forming reactions in felsic orthogneiss: Implications for densification and strengthening of the lower continental crust". In: *Earth and Planetary Science Letters* 405, pp. 207–219. DOI: 10.1016/j.epsl.2014.08.030.

Williams, Melis, Kopf, and Hanmer (2000). "Microstructural tectonometamorphic processes and the development of gneissic layering: a mechanism for metamorphic segregation". In: *Journal of Metamorphic Geology* 18.1, pp. 41–57. DOI: 10.1046/j.1525-1314.2000.00235.x.

Appendix A

Map of field sites for QMAP data

The figure on the following page is a copy of figure 3.1, but includes dots to represent the location of field sites that were visited in the preparation of the Fiordland QMAP (Turnbull et al. 2010). The structural data from the sites reported by Turnbull et al. (2010) helped to constrain and define the extent of GSSZ fabrics at areas located between those field areas presented in this thesis. The interpretation of these structural data is discussed in chapter four.

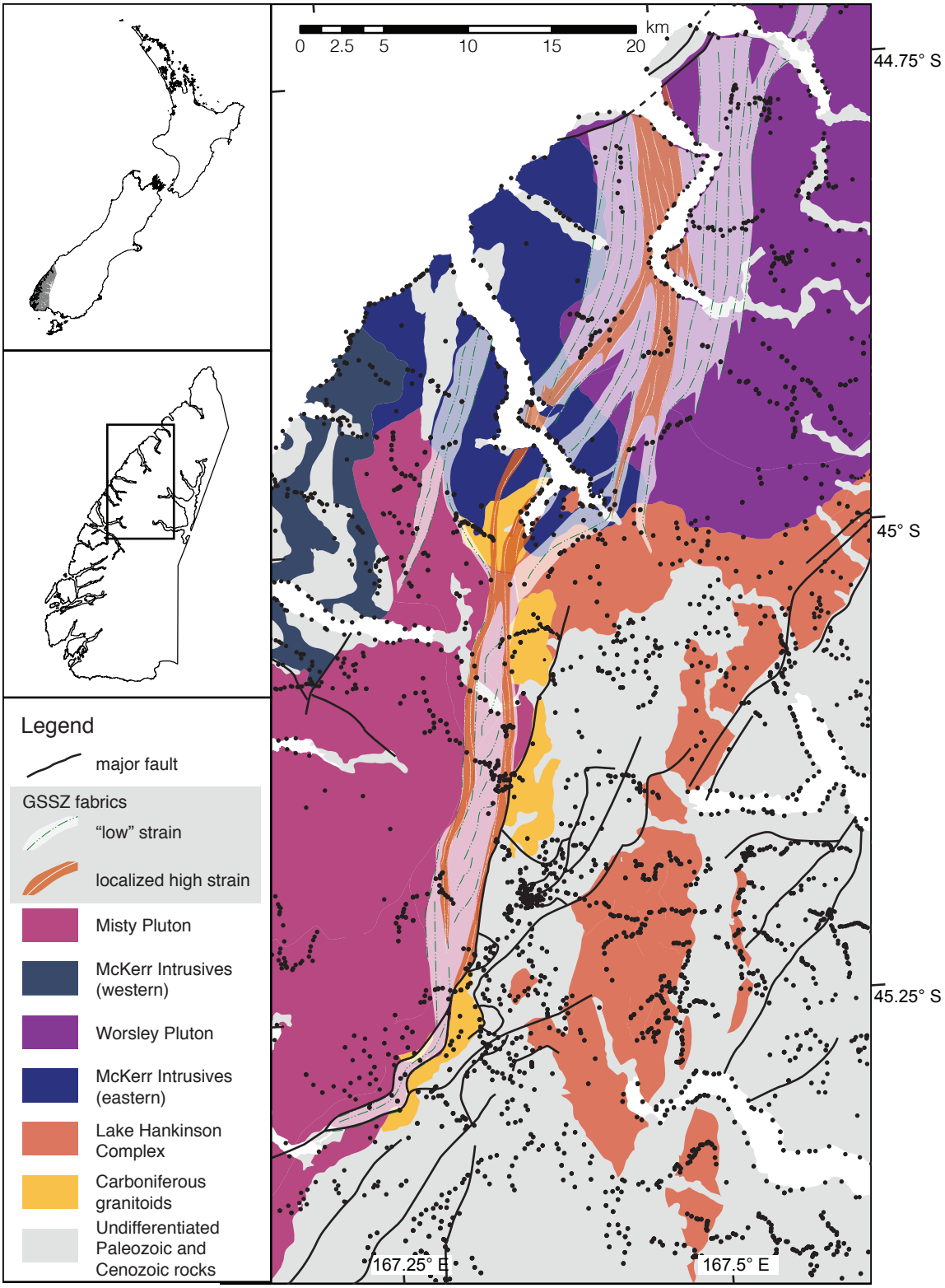
km
0 2.5 5 10 15 20
44.75° S
45° S
45.25° S
167.25° E
167.5° E
Legend
major fault
GSSZ fabrics
"low" strain
localized high strain
Misty Pluton
McKerr Intrusives (western)
Worsley Pluton
McKerr Intrusives (eastern)
Lake Hankinson Complex
Carboniferous granitoids
Undifferentiated Paleozoic and Cenozoic rocks

Appendix B

Bligh Sound mineral composition

The following pages contains raw mineral composition data output from Oxford AZtec EDS quantification software for mineral analyses on Bligh Sound samples. All compositions are reported in oxide wt. %.

Feldspar Compositions

Sample	18BS42A	18BS42A	18BS42A	18BS42A	18BS42A	18BS42A	18BS35A	18BS35A	18BS35A
Spectrum ID	Spectrum 589	Spectrum 590	Spectrum 604	Spectrum 606	Spectrum 612	Spectrum 613	Spectrum 622	Spectrum 623	Spectrum 625
Na_2O	8.4	8.91	8.16	8.6	8.34	8.73	8.33	7.74	8.58
MgO	0	0	0	0	0	0	0	0	0
Al_2O_3	24.83	26.17	23.3	24.36	24.82	25.58	26.11	24.54	26.84
SiO_2	62.8	66.17	59.52	62.57	62.43	65	64.08	59.94	66.15
P_2O_5	0.26	0.27	0	0.36	0	0.27	0.35	0	0.34
K_2O	0.34	0.28	0.34	0.15	0.19	0.28	0.34	0.37	0.35
CaO	5.12	5.42	4.83	4.97	5.33	5.19	6.06	5.8	6.24
TiO_2	0	0	0	0	0	0	0	0	0
MnO	0	0	0	0	0	0	0	0	0
FeO	0	0	0	0	0	0	0	0	0
Total	101.75	107.22	96.15	101	101.1	105.05	105.27	98.38	108.51

Feldspar Compositions

Sample	18BS35A	18BS35A	18BS35A	18BS64A	18BS64A	18BS64A	18BS64A	18BS64A	18BS64A
Spectrum ID	Spectrum 633	Spectrum 641	Spectrum 647	Spectrum 659	Spectrum 661	Spectrum 668	Spectrum 680	Spectrum 681	Spectrum 686
Na_2O	8.46	7.85	8.2	7.56	8.07	7.7	8.14	8.81	8.66
MgO	0	0	0	0	0	0	0	0	0
Al_2O_3	26.35	25.09	25.77	22.91	23.55	22.72	24.64	25.52	25.3
SiO_2	64.09	61.15	62.97	56.35	59.61	57.31	60.85	63.34	63.66
P_2O_5	0.28	0.26	0	0	0.26	0	0.26	0.34	0.26
K_2O	0.29	0.27	0.17	0.2	0.15	0	0	0	0.16
CaO	6.18	5.9	6.02	5.08	4.99	4.85	5.49	5.42	5.4
TiO_2	0	0	0	0	0	0	0	0	0
MnO	0	0	0	0	0	0	0	0	0
FeO	0	0	0	0	0	0	0	0	0
Total	105.65	100.52	103.12	92.1	96.63	92.58	99.38	103.42	103.45

Feldspar Compositions

Sample	18BS64A	18BS42A	18BS42A	18BS42A	18BS42A	18BS35A	18BS35A	18BS35A	18BS35A
Spectrum ID	Spectrum 687	Spectrum 592	Spectrum 595	Spectrum 605	Spectrum 610	Spectrum 620	Spectrum 624	Spectrum 631	Spectrum 640
Na_2O	8.4	0.72	0.85	0.43	0.96	0.64	0.4	0.91	0.51
MgO	0	0	0	0	0	0	0	0	0
Al_2O_3	24.64	18.75	18.81	17.92	20.61	19.28	20.12	20.29	19.61
SiO_2	61.42	62.19	62.13	59.72	67.55	64.45	68	67.85	65.71
P_2O_5	0.28	0.28	0	0	0	0	0	0	0.29
K_2O	0	14.53	13.99	14.15	15.39	15.26	16.28	15.48	15.65
CaO	5.35	0	0	0	0	0	0	0	0
TiO_2	0	0.28	0.22	0.21	0.27	0.31	0.32	0.25	0.26
MnO	0	0	0	0	0	0	0	0	0
FeO	0	0	0	0	0	0	0	0	0
Total	100.09	96.75	95.99	92.42	104.78	99.94	105.12	104.77	102.03

Feldspar Compositions

Sample	18BS35A	18BS35A	18BS64A	18BS64A	18BS64A	18BS64A	18BS64A	18BS64A	18BS64A
Spectrum ID	Spectrum 646	Spectrum 648	Spectrum 660	Spectrum 665	Spectrum 673	Spectrum 688	Spectrum 692	Spectrum 703	Spectrum 707
Na_2O	0.95	1.77	0.61	0.98	1.41	1.2	0.55	1.28	0.69
MgO	0	0	0	0	0	0	0	0	0
Al_2O_3	20.42	20.28	16.91	18.44	19.4	18.49	19.17	18.61	19.56
SiO_2	68.78	66.14	56.97	61.35	64.71	62.41	64.57	62.4	65.93
P_2O_5	0	0	0	0.27	0.28	0	0	0	0
K_2O	15.66	13.17	13.54	14.08	14.29	13.84	15.19	13.73	15.58
CaO	0	0.78	0	0	0	0	0	0	0
TiO_2	0.28	0	0.25	0.25	0.32	0.22	0.25	0.33	0.26
MnO	0	0	0	0	0	0	0	0	0
FeO	0	0	0	0	0	0	0	0	0
Total	106.09	102.14	88.28	95.37	100.41	96.15	99.73	96.36	102.02

Orthopyroxene Compositions

Sample	18BS42A	18BS42A	18BS42A	18BS42A	18BS42A	18BS42A	18BS35A	18BS35A
Spectrum Label	Spectrum 585	Spectrum 596	Spectrum 599	Spectrum 601	Spectrum 607	Spectrum 609	Spectrum 615	Spectrum 628
Na_2O	0	0	0	0.24	0.47	0	0.24	0.26
MgO	22.67	23.08	20.9	22.98	22.36	22.7	19.97	19.43
Al_2O_3	4.32	3.41	3.22	3.83	3.58	3.63	3.86	3.52
SiO_2	54.1	54.19	49.1	54	53.03	54.24	54.19	52.87
P_2O_5	0	0	0	0	0	0	0	0
K_2O	0	0	0	0	0	0	0	0
CaO	0.29	0.34	0.41	0.42	0.55	0.42	0.48	0.9
TiO_2	0	0	0	0	0	0	0	0
MnO	0.67	0.62	0.53	0.64	0.56	0.67	0.64	0.56
FeO	22.65	22.28	19.79	22.54	21.08	22.68	27.04	26.05
Total	104.69	103.91	93.96	104.65	101.62	104.34	106.43	103.59

Orthopyroxene Compositions

Data from Aztec	18BS35A	18BS35A	18BS64A	18BS64A	18BS64A	18BS64A	18BS64A	18BS64A
Spectrum Label	Spectrum 635	Spectrum 642	Spectrum 652	Spectrum 653	Spectrum 669	Spectrum 675	Spectrum 679	Spectrum 694
Na_2O	0.24	0	0.22	0	0	0	0	0
MgO	19.4	15.62	18.63	17.81	25.15	18.26	18.21	15.22
Al_2O_3	3.89	3.01	2.44	2.79	1.49	2.84	2.54	2.15
SiO_2	53.28	42.51	50.88	48.97	63.68	52.15	50.29	43.5
P_2O_5	0	0	0	0	0	0	0	0
K_2O	0	0	0	0	0	0	0	0
CaO	0.48	0.32	0.5	0.4	0	0.43	0.43	0.34
TiO_2	0	0	0	0	0.2	0	0	0
MnO	0.64	0.61	0.7	0.77	0	0.85	0.68	0.52
FeO	27.13	21.28	25.86	24.31	9.57	28.13	25.46	22.88
Total	105.06	83.36	99.23	95.04	100.09	102.66	97.62	84.61

Clinopyroxene compositions

Sample	18BS42A	18BS42A	18BS42A	18BS42A	18BS42A	18BS42A	18BS35A	18BS35A	18BS35A
Spectrum ID	Spectrum 586	Spectrum 587	Spectrum 598	Spectrum 600	Spectrum 608	Spectrum 611	Spectrum 619	Spectrum 621	Spectrum 629
Na_2O	2.19	1.96	2.09	1.89	1.64	1.98	1.86	1.86	2.07
MgO	12.11	12.33	11.85	12.24	13.85	11.15	11.41	10.06	11.19
Al_2O_3	6.34	5.81	6.21	6.06	4.63	5.76	6.61	5.91	6.49
SiO_2	54.42	53.7	53.24	53.16	51.66	50.37	52.72	48.01	54.67
P_2O_5	0	0	0	0	0	0	0	0	0
K_2O	0	0	0	0	0	0	0	0	0
CaO	20.47	19.24	20.2	20.38	12.62	18.88	20.02	18.41	20.98
TiO_2	0.4	0.48	0.55	0.48	0.41	0.47	0.55	0.47	0.42
MnO	0.23	0.26	0	0.23	0.32	0.21	0.27	0.2	0.31
FeO	9.06	10.05	9.17	9.58	13.87	8.43	10.53	9.63	10.77
Total	105.22	103.84	103.31	104.01	99	97.26	103.98	94.55	106.9

Clinopyroxene compositions						Hornblende compositions			
Sample	18BS35A	18BS35A	18BS64A	18BS64A	18BS64A	Sample	18BS35A	18BS35A	18BS35A
Spectrum ID	Spectrum 637	Spectrum 643	Spectrum 656	Spectrum 662	Spectrum 666	Spectrum ID	Spectrum 617	Spectrum 627	Spectrum 639
Na_2O	1.96	1.62	1.51	1.7	1.47	Na_2O	1.96	1.67	1.71
MgO	11.53	10.31	10.68	11.33	9.66	MgO	9.69	9.63	9.37
Al_2O_3	6.37	5.59	4.21	4.34	4.26	Al_2O_3	16.41	16.51	15.39
SiO_2	54.36	49.54	49.55	52.72	44.88	SiO_2	42.88	42.83	41.75
P_2O_5	0	0	0	0	0	P_2O_5	0	0	0
K_2O	0	0	0	0	0	K_2O	2.5	2.84	2.53
CaO	20.84	18.37	19.11	20.16	17.5	CaO	11.35	11.68	11.12
TiO_2	0.65	0.57	0.37	0.36	0.38	TiO_2	2.6	2.33	2.39
MnO	0.23	0.26	0.26	0.34	0	MnO	0.22	0	0
FeO	10.61	10.44	10.15	10.43	8.72	FeO	16.41	16.17	16.01
Total	106.55	96.69	95.83	101.36	86.87	Total	104.03	103.65	100.26

Hornblende compositions

Sample	18BS64A	18BS64A	18BS64A	18BS64A	18BS64A	18BS64A	18BS64A	18BS64A
Spectrum ID	Spectrum 655	Spectrum 664	Spectrum 674	Spectrum 684	Spectrum 693	Spectrum 696	Spectrum 700	Spectrum 702
Na_2O	1.26	1.73	2.1	2.1	1.64	2.05	1.83	2.02
MgO	7.56	7.7	9.22	8.59	7.16	8.51	8.31	8.93
Al_2O_3	11.37	13.22	14.52	14.77	11.35	14.63	13.78	13.44
SiO_2	34.19	37.38	42.29	40.66	33.83	41.36	40.44	39.72
P_2O_5	0	0	0	0	0	0	0	0
K_2O	1.65	1.95	2.15	2.13	1.75	2.18	2.01	1.95
CaO	9.04	9.73	10.9	10.64	8.78	10.45	10.39	10.17
TiO_2	1.31	2.11	2.29	2.47	2.12	2.06	1.54	2.3
MnO	0	0	0	0	0	0.2	0.26	0
FeO	14.01	15.91	17.37	16.53	14	17.48	17.14	15.3
Total	80.39	89.73	100.84	97.88	80.64	98.93	95.69	93.82

Biotite compositions

Sample	18BS64A	18BS64A	18BS64A	18BS64A	18BS64A	18BS64A	18BS64A	18BS64A
Spectrum ID	Spectrum 670	Spectrum 671	Spectrum 672	Spectrum 676	Spectrum 685	Spectrum 695	Spectrum 698	Spectrum 705
Na_2O	0	0	0	0	0	0	0	0.21
MgO	10.61	11.62	11.37	11.84	10.11	11.76	10.42	10.55
Al_2O_3	14.15	14.86	15.21	15.49	14.98	14.96	13.91	14.08
SiO_2	35.83	37.48	37.46	37.46	36.48	37.41	38.42	35.25
P_2O_5	0	0	0	0	0	0	0	0
K_2O	8.65	9.68	9.58	9.71	9.47	9.44	8.96	8.55
CaO	0	0	0	0	0	0	0	0
TiO_2	4.14	4.67	4.39	4.47	6.08	4.32	4.12	4.18
MnO	0	0	0	0	0	0	0	0
FeO	17.69	18.31	18.91	18.21	17.58	18.31	17.85	18.68
Total	91.07	96.62	96.93	97.19	94.7	96.21	93.68	91.5